Automated Reaction Discovery Tools and their Application to Understanding Organometallic Reactions

by

Amanda L. Dewyer

A dissertation submitted in partial fulfillment
of the requirements for the degree of
Doctor of Philosophy
(Chemistry)
in the University of Michigan
2019

Doctoral Committee:

Associate Professor Paul M. Zimmerman, Chair
Professor Ronald G. Larson
Professor Anne J. McNeil
Professor Melanie S. Sanford

Amanda L. Dewyer

adewyer@umich.edu

ORCID iD: 0000-0002-2660-6188

DEDICATION

This thesis is dedicated to my Parents, Terri and Joe Dewyer, for their unwavering faith in my ability to succeed in life, and their constant support in all of the endeavors I pursue.

ACKNOWLEDGMENTS

This thesis was made possible with the support and guidance of Professor Paul Zimmerman, as well as by funding from The University of Michigan's Rackham Graduate School, The University of Michigan Language, Science and Arts School, University of Michigan's Department of Chemistry, and by Dow Chemical Company.

TABLE OF CONTENTS

LIST OF TABLES

LIST OF FIGURES

LIST OF APPENDICIES

ABSTRACT

Using computational simulations to model reaction mechanisms has been a common way to garner kinetic and thermodynamic information of a chemical system that can help to understand reaction rates and selectivities. The most widely used tools available for reaction path modeling, however, lend themselves to working best when chemical intuition or experimental data for a chemical reaction is available to help build the simulation. In order to model reaction mechanisms of chemical systems that have not been well studied, or even tested experimentally yet, new tools for simulation are needed that do not rely on chemical intuition or experimental data. Herein, new methods developed for reaction discovery are laid out and applied to understanding transition metal catalyzed reactions on a deeper level. The first tool, ZStruct, allows for the systematic exploration of chemical space for unimolecular and bimolecular reactions for both organic and organometallic reactions. This method requires minimal user guidance, with the only prior knowledge required being that of which atoms on each reactant may be participating in bond forming/breaking processes. This method has been applied to explore the following reaction: (1) methane activation by cisplatin, where 10 previously unexplored reaction pathways were identified. (2) Ni(II)-catalyzed beta-hydride elimination, where off cycle Ni-THF or Ni-pyridine intermediates were found to be thermodynamically favorable. (3) Palladium-catalyzed piperidine arylation, where the full catalytic cycle, including the rate limiting C-H activation step, as well as roles of important Ar-I and Cs-salt additives, were elucidated through ZStruct's ability to explore chemical space. The second tool, CGen, allows for sampling conformational changes that reactants of interest can undergo, and use them to generate metal-reactant complexes. Using the conformers that are generated, reaction discovery using ZStruct can be done to understand how conformational changes impact the mechanism by which a reaction occurs. Additionally, CGen can also be used to create catalyst-reagent complexes (reagents could be counterions, solvent molecules, or any other molecular additives

used experimentally) by aligning a catalyst and reagent of interest in different orientations, thus allowing for better sampling of molecular interactions during a reaction. CGen was used to explore the chemical space of ethylene polymerization with a Ti-constrained geometry catalyst (Ti-CGC). With this system the impact of the polymer chain conformation on the mechanism to ethylene insertion was investigated. The favorable pathways to insertion that were found involve polymer chain conformations that maximize the distance between Ti and the polymer chain. The barriers to insertion found with the naked cation system were lower than experimental results, implying that inclusion of the experimentally required borane counterion is important for generating a model that reflects experimental observations. Therefore, the same reaction was remodeled once with Me-$B(C_6F_5)_3^-$ and again with $B(C_6F_5)_4^-$, and in both cases CGen was used to generate Counterion-catalyst complexes. The sampling of various counterion alignments and polymer chain conformations demonstrated that alignment/conformer combinations can actually impede monomer insertion from occurring. Additionally, the models showed that the difference in nucleophilic strength between the two counterions impact how energetically challenging monomer uptake prior to insertion is, as well as how each counterion positions itself with respect to the catalyst during monomer insertion. The insights gained using reaction discovery methods in this work gave way to a deeper understanding of how chemical interactions in-situ may be hindering or helping a chemical reaction to occur.

CHAPTER I

Introduction

This work partly appears in Reference 60

Deep mechanistic insight into chemical reactions can be gained from atomistic studies of elementary steps, where one intermediate is connected to another by a path containing a single transition state (TS). The three-dimensional structural information provided by reaction paths not only provides a basic framework for conceptualizing the reaction, but also can estimate the rates, thermodynamics, and selectivity of a reaction.

Since the advent of quantum chemistry it has been known that reaction mechanisms, in principle, could be studied using computational modeling.[1] With the significant advances in quantum chemical methods and computer processor speed over the past few decades, it has now become commonplace to use computation to investigate reaction mechanisms.[2,3] Popular electronic structure methods, such as density functional[4] or wave function theories,[5] are available to accurately evaluate the structures and energetics of a sequence of intermediates and TSs in an envisioned reaction mechanism.

Density Functional Theory

The use of Density Functional Theory (DFT) has become a common practice for modeling chemical reactions to understand the geometry of intermediates and transition state structures, as well as their relative energies to explain experimentally observed rates and selectivities. By utilizing the electron probability density, $\boldsymbol{\rho}$, of the chemical system in place of the wavefunction describing the electrons themselves, DFT enables the modeling of larger systems, without facing the same scaling issues as other higher accuracy methods such as coupled-cluster theory (CCSD(T))[6,7], which is considered the "gold standard" of quantum chemistry. (scaled = N^3 for DFT versus N^7 for CCSD(T), N=number of atoms.)[8,9] This lowered computational cost of DFT balances

out with the lower accuracy compared to CCSD(T), making it a viable choice for modeling a variety of chemical systems, including organometallic reactions.[10-15]

In order to describe the electron density of a molecule, DFT utilizes functionals to describe the electron density. However, the true density functional of a system is not known. Instead, approximations of the functional have been developed by numerous groups by using experimental data and databases of chemical information to parameterize each specific functional in an effort create generalized methods that work with a variety of chemical systems.[7-9] These approximations lead to some functionals being better suited to treat certain chemical systems compared to other (i.e. organic versus inorganic complexes). There are however, some functionals which have been shown to do a decent job of modeling a broad array of reactions, such as B3LYP.[16-20] However, even this broadly applicable method is known to perform poorly in some cases such as modeling excited states in charge transfer reactions.[21-23]

Another factor that impacts the accuracy of DFT calculations, is the choice of basis set used to define the orbitals that electrons can occupy, which the functional uses to calculate the electron probability density. For example, with main group elements using basis sets with functions describing at least both s and p orbitals is required for accurate modeling. If a transition metal is being modeled, then a larger basis set that includes functions to describe d and potentially f orbitals becomes necessary to calculate the electron density. Therefore, the accuracy of a calculation is dependent on both the functional and basis set of choice for any given calculations.

In addition to accuracy being dependent on method choice, another caveat of DFT is its poor ability to model weak dispersion interactions (Vander Waal's forces), which can be important in chemical systems such as organometallic reactions.[19,24,25] The inability to model these interactions arises from an inability of exchange-correlation functionals to describe long range electron dispersion forces.[26] To combat this issue, a variety of methods for modeling these long range interactions have been developed. For example, the addition of empirical dispersion corrections can be added to a functional, as was done to develop dispersion corrected DFT methods such as ωB97X-D[27]. These methods improve the ability of DFT to capture these weak interactions and has led to the ability to more accurately model organometallic reactions where

long-range dispersion interactions are important. Despite the approximations used in DFT, when appropriate basis sets and functionals are combined, they have been shown to generate optimized structures that closely resemble experimentally determined geometries.[28-30] Additionally, the calculation of reaction energetics (thermodynamics and kinetic barriers) within reasonable accuracy has allowed for DFT to be used in a wide variety of systems to explain experimental outcomes.[16-19,31-33] As with all methods though, DFT still has error associated with it.[34] When the best method (i.e. an appropriate functional and basis set) is used, statistical errors bars of 2 kcal/mol are possible.[31-40]

Modeling Reactions with Quantum Chemistry

With powerful tools such as DFT, researchers in the field of quantum chemistry have been able to examine a wide scope of reactions,[31-33,41,42] However, when doing so, these methods are best at evaluating previously hypothesized, chemically intuited mechanisms. In other words, computational methods do not usually discover reaction pathways, but instead evaluate reactions based on existing chemical knowledge. For mechanisms where no hypotheses are available—and the researchers "just don't know"—computation has not really offered practical solutions to discover these unknown mechanisms.

This "just don't know" problem becomes compounded in situations where chemical reactivity is complex. For example, in transition metal-catalyzed reactions, numerous elementary steps can be required to convert initial reactants into end products. These multi-step processes can involve a multitude of intermediate structures that can be impossible to isolate experimentally. This can make it hard or impossible to probe the mechanism from an experimental standpoint, limiting the amount of intuition available to guide computational studies. In addition, to the catalytic reaction pathways of interest, there can also be a variety of competing off-cycle pathways occurring that lead to inactive catalysis species or side products. Finally, when additives, ligands, and solvent are considered the number of potential transition metal species (with varying oxidation states, conformations, and coordination modes) that could exist in-situ can drastically increase. In order to explore chemical reactivity, gain mechanistic insight and make predictions with computation all of these factors need to be taken into

consideration to get a full picture of what is going on in situ. The variety of factors, and the complexity of modeling how numerous reagents interact makes it increasingly difficult to probe whether the catalyst species and intermediates being studied computationally are the active species inside of the flask, **Figure I.1**.

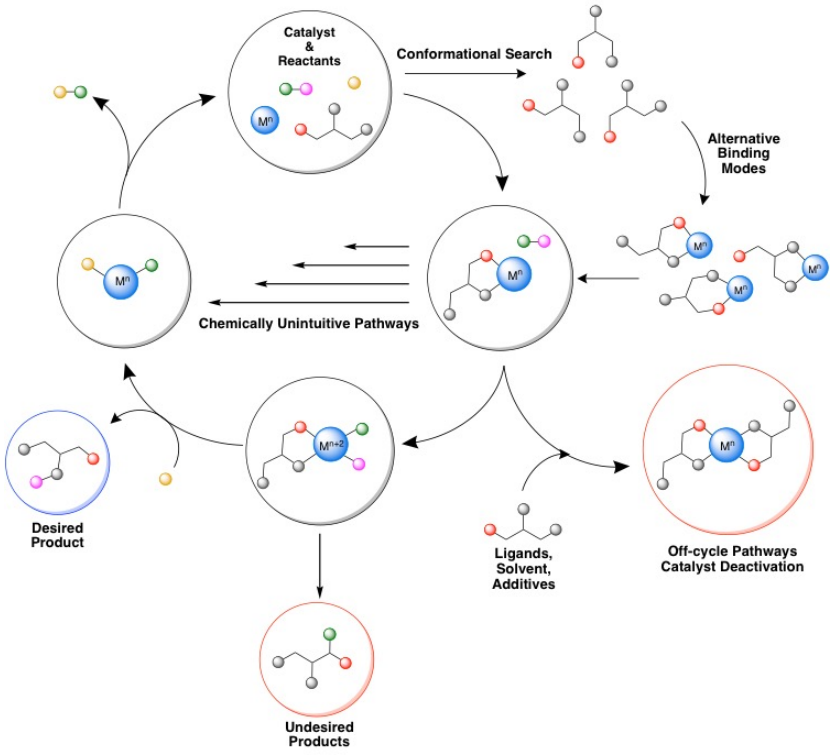

Figure I.1: Complexities associated with computational modeling of reactions

With all of the complexities of capturing experimental conditions and the expansive reaction network that can be taking place in situ, computational models that lack experimental guidance may be insufficient for explaining reactivity. This is especially true in situations where the "just don't know" problem persists.

In an effort to combat this "just don't know" problem, a highly successful model of a reaction is needed in which all key elementary steps composing the mechanism are known and accounted for. Building such a model is by no means trivial, even for relatively well-studied reactions where many of the elementary steps are already known. For emerging reactions with

little mechanistic precedent, the task requires large amounts of effort—both computational and human time—and no current strategy provides any guarantee of success.

Automating Reaction Discovery

Despite there being no guarantee of success, a number of interesting ways to go about reaction discovery have been developed though, including: optimization methods,[43,44] computer aided synthesis,[45] QM/MM,[46-50] MD simulations that do not look for TSs,[51-54] potential energy surface generation,[55,56] machine learning tools[57-59], PES exploration tools for molecular systems, and related atomistic methods that approximate the information that would have come from *ab initio* simulation.[60]

Of these methods, the PES exploration tools allow for combining chemical intuition with a priori knowledge of chemical reactivity to discover elementary reaction networks in a systematic, and reliable way. This ability gives these methods an advantage towards being useable tools for automating reaction discovery.

These PES exploration tools use first principles, or *ab initio*, simulations of reactant molecules and catalysts to generate potential energy surfaces (PES)—and from this free energy surfaces— which are approximations to the true reactive landscapes of an experiment. From the PES important intermediates, TSs, and elementary step reaction pathways are obtained, and thus a deeper, more detailed, understanding of chemical reactions can be achieved. Specifically, the identification of TS structures for elementary steps of a reaction provide kinetic information from which rates and selectivity can be determined.

Generally these methods can be categorized as follows: (1) Forced reaction discovery biased along a specific reaction coordinate (e.g. a change in distance between two or more atoms)[54,61-63] (2) "By-hand" reaction discovery, where chemical intuition is used to make guesses at intermediate and TS structures for a reaction of interest.[44,64] (3) Systematic reaction discovery where changes in connectivity or other chemical descriptors are used to describe a reaction path.[65-67] A comparison of these powerful methods can be found in **Figure I.2**.

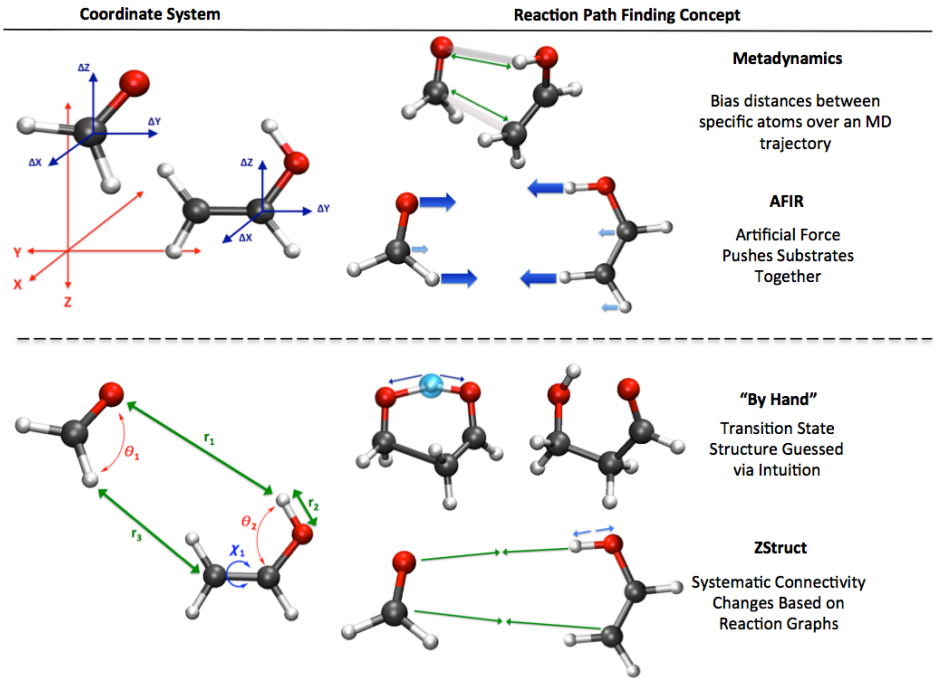

Figure I.2. Comparison of selected, computational reaction finding methods.

In principle, all potential elementary steps may be located by exploring these PES landscapes. However, the high dimensionality (approximately 3N, where N is the number of atoms in the system) of the surfaces means that exhaustive exploration is usually impossible. Therefore, if computational predictions about reactivity are to be made, then some form of systematic PES search strategy must be developed. One possible route to this can be achieved through low-dimensional re-envisioning of reaction paths to locate intermediates and the TSs that connect them.

This desire to guide experiment through computational predictions leads directly to the two key challenges of automated reaction discovery: **1. Locating reaction paths for single elementary steps and quantifying the reaction rate,** and **2. Identifying hypothetical reaction pathways quickly, automatically, and with good coverage of the physically relevant elementary steps with minimal need for chemical intuition.**

The standard toolkit for computational reaction searches avoids the problem of dimensionality by providing, as input, specific reaction coordinates from which reaction pathways can be generated. There are three general methods by which this can be achieved: (I)

TS finding, followed by an intrinsic reaction coordinate calculation (IRC)[68], which connects the TS to its neighboring intermediates (**Figure I.3**, a), (II) single-ended searching by moving along a reaction coordinate through a TS to a new intermediate (**Figure I.3,** b) or (III) double-ended path optimization starting from two endpoints of the considered reaction path (**Figure I.3, c**). All of these methods use a local TS finder to optimize saddle points[69-72] along the identified reaction pathway based on a guess structure. In the case of Method I, the TS guess is generated and optimized prior to the IRC calculation. Methods II and III on the other hand, generate a guess structure during reaction path generation. The success in finding a TS structure is highly dependent on the quality of the guess structure generated with these methods.

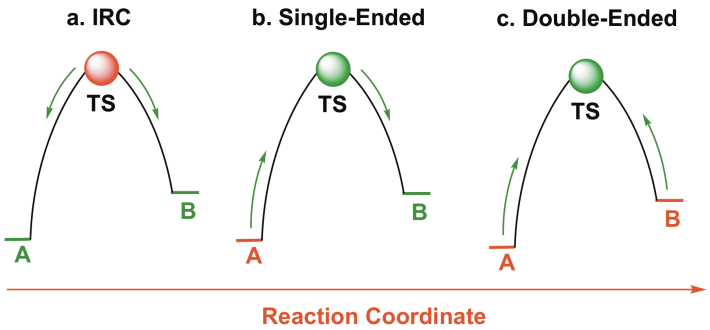

Figure I.3. Types of reaction pathway searches that can be used to identify single elementary steps connecting two intermediates.

Largely, these methods have relied on chemical intuition to designate the reaction paths and TSs that are of interest to search for.[73,74] Therefore these methods accomplish **Goal 1**, but at the same time they do not solve **Goal 2**. New tools that accomplish **Goals 1** and **2** together are needed, to achieve high-fidelity, low-cost PES exploration without high reliance on prior chemical knowledge. In general, a strong strategy for PES exploration must synergistically combine a reaction hypothesis generator and reaction path finder to achieve maximal success.

Achieving this synergy between a given reaction path finder and reaction hypothesis generator is not trivial though. Multiple methods for reaction hypothesis generation have been developed, that work with the reaction path finders described above, and can be broken down into four different categories described below.

Four Concepts for Discovering Elementary Reaction Networks

The four categories shown in **Figure I.4** all have methods that begin with a designation of the initial reactants and catalysts, but otherwise are supposed to operate with as little input from a researcher as possible. The categories are: (1) encoded elementary step types where databases of experimental information or chemical heuristics are used to describe reaction pathways.[75-82] (2) Automated generation of approximate TSs, sometimes through the use of artificial forces to push two molecules together, followed by local TS optimization and IRC computations.[83-91] (3) Potential elementary step intermediates are generated from input reactants using a graphical tool, and double-ended methods are used to refine a reaction path and TS. [65-67,92-96] (4) Hypothetical reaction coordinates are generated based on a graph, and used with single-ended methods for reaction path searches.[97,98] All of these methods generate approximate reaction paths, estimate energetic barriers for reaction, and can be used to sequentially create huge networks of elementary steps. Despite the apparent promise of user-interaction-free exploration, every method still requires at least some input of chemical intuition.

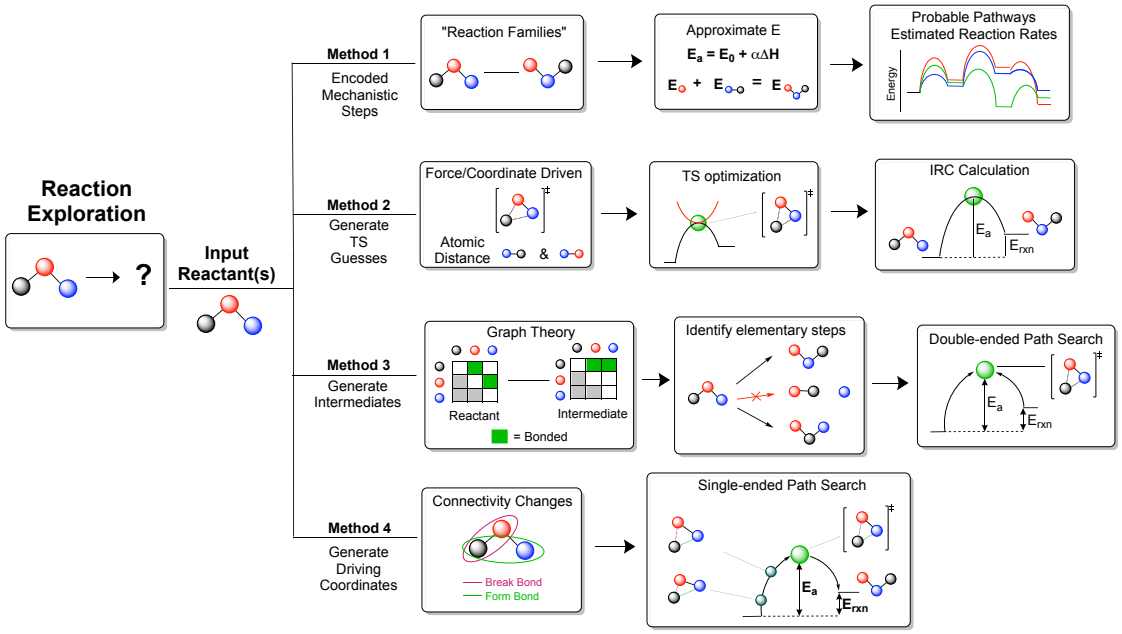

Figure I.4. Four main groups for automated reaction hypothesis generation and reaction exploration.

Specifically, approaches within categories 1 and 2 tend to require more a priori chemical information (databases of experimental information) or chemical intuition about intermediate structures. **Group 3** and **4** methods, on the other-hand shows promise for a systematic, less guided, approach to reaction discovery by implementing the use of connectivity changes to generate potential elementary steps of a reaction.

This use of connectivity changes in the **Group 3** method, specifically that of ZStruct generated in the Zimmerman Group[65,66,67,97], proved to be a powerful tool for exploring unknown pathways.[99-108] For example, work by Montgomery and co-workers utilized ZStruct to assess the PES for a Ni-catalyzed C-H activation reaction, where it was found that the catalyst ligand, cyclo-octadiene (COD), was reactive leading to an off-cycle π-allyl complex that inhibited C-H activation.[106] Once this off-cycle intermediate was identified COD was replaced with 1,5-hexadiene experimentally. This change in ligand, prompted by ZStruct, shut down the pathway to the formation of the π-allyl complex and led to productive C-H activation, as predicted by computation.

Despite the impressive predictive capabilities of ZStruct, this approach still requires generation and optimization of potential intermediates prior to reaction path exploration, which can be tedious and computationally costly. Additionally, for bimolecular or transition-metal catalyzed reactions user input of aligned starting structures is needed, which require chemical intuition to generate.

For this reason, a **Group 4** approach in which no specific intermediate structure needs to be defined prior to reaction exploration was developed on the shoulders of ZStruct. The availability of using the single-ended Growing String Method (SE-GSM), developed within the Zimmerman Group[109], to generate elementary step reaction paths made it apparent that ZStruct's connectivity changes could be used as driving coordinates for SE-GSM. This led to the development of an updated version of ZStruct, which allows for more systematic modeling of bimolecular and transition metal-catalyzed reactions. Through the use of connectivity changes, aligned reactant structures and hypothesized driving coordinates leading to elementary steps can be generated, and used with SE-GSM for reaction exploration.[97]

With ZStruct greater flexibility in exploring both intuitive and unintuitive reaction pathways for unimolecular, bimolecular, and transition metal-catalyzed reactions leading to both desired and undesired products is achievable. This ability is a critical feature needed for reaction discovery tools, especially if computation hopes to guide experimental design through predicting chemical reactivity. Even with tools like ZStruct, the task of guiding experiment is still non-trivial. Part of the challenge that remains lies in the fact that the number of potential pathways to explore increases as the complexity of the chemical system increases (i.e. numerous conformational changes of reactants being possible) and as the number of reagents interacting with one another in situ increases.

Challenges in Modeling Complex Reaction Networks

In an ideal world, one would be able to create a simple model that only requires accounting for reactants that are undergoing connectivity changes to map the PES, and understand what chemistry is going on inside of a flask. However, additives that are believed to be innocent, counterions that are thought to participate in one step of a reaction, but not others, and even the conformational flexibility of a catalyst or reactant can significantly complicate the ability to create a reliable, accurate chemical model for predicting chemistry.

Despite ZStruct's ability to expand the scope of chemical space that can be explored, computational models are only as good as their ability to capture what is going on experimentally. As noted above, see **Figure I.1**, catalysis is further complicated by interactions that occur between reactants, additives, solvent, and catalysts *in situ*. The realization that modeling these interactions can be key to understanding and explaining the experimental outcomes of a reaction has become more evident with time.[104,105,107]

The task of modeling these interactions expands the scope of intermediates, TSs, and reaction pathways that need to be considered, and when done manually greater user-guidance and chemical intuition is required and can still lead to skipping over key intermediates and pathways that are unintuitive. The need to consider these interactions led to the development of a method for systematically generating metal-L (L = ligand, substrate, additive, solvent) complexes to aid in creating more accurate models. In addition to the complexity added by using

multiple reagents, it has become obvious that rotatable bonds complicate matters even more.[110]

One could imagine that flexible catalysts ligands, or substrates can result in numerous conformers existing in situ that could participate in the reaction.[111-116] Capturing these conformers and understanding how they impact the energetics obtained through computation can make or break the accuracy of a model. For example, if a conformer is chosen at random without sampling, then there is no guarantee that it will lead to the minimum energy pathway, as shown in **Figure I.5**. If conformational sampling is done, then the best conformer(s) can be used in computational models, from which better estimates of reaction energies can be obtained.

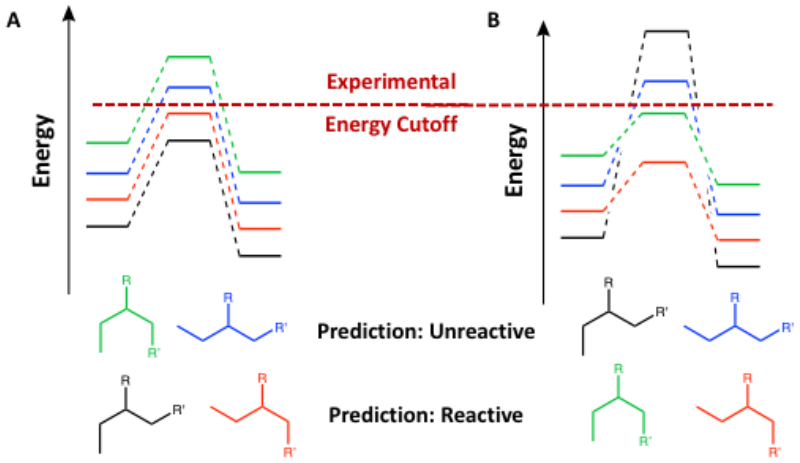

Figure I.5: Hypothetical reaction path energy diagrams comparing conformers of a generic alkyl molecule. (A) Situation where the activation barrier is dependent upon relative energies of reactant conformers, leading to predictions of the conformers in black and red being reactive, and the green and blue conformers being unreactive. (B) Situation where the activation barrier is independent of the relative energy of reactant conformers, leading to predictions of the conformers in green and red being reactive, and the black and blue conformers being unreactive.

Additionally, conformational sampling can allow for greater insight to be gained into what structural features impact the activation barrier of a reaction. By looking at how small differences in substrate structures change the relative energies amongst conformers, models could be generated that provide insight as to what structural features lead to more stable intermediates, or reaction pathways. This insight could be used to enhance the ability to design catalysts or substrates for a reaction of interest.

Dealing with the complexities of modeling reactions including solvent and additive interactions, as well as the generation of conformers through bond rotations is a trivial task. They all can require extensive chemical intuition and user-effort to arrive at a reasonable starting structure for reaction discovery. The need for a systematic way to tackle these issues led to the development of a second automated reaction exploration tool, namely CGen. This tool allows conformers of a reactant or ligand to be systematically generated using OpenBabel's Confab software[117], **Figure I.6.** In the case of transition metal catalyzed reactions, where ligands, additives or solvent coordinate to the metal center, this tool can also generate M-L complexes (L = solvent, additive, ligand, or substrate of interest) with each conformer generated.

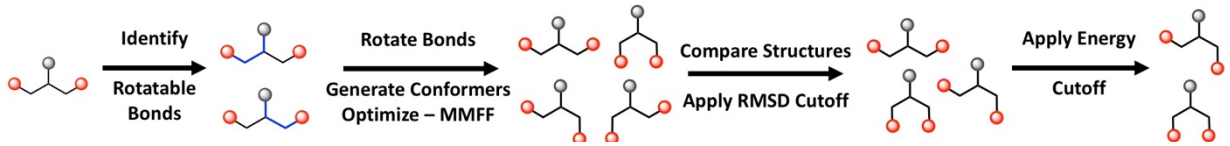

Figure I.6: Flow chart for conformer generation using OpenBabel's Confab Function.

By first using CGen to generate initial conformers and/or M-L complexes for reaction discovery, the systematic identification of low energy structures from which to model a reaction pathway can be done with minimal user interaction or chemical intuition. The output of this tool can then be used as input for ZStruct in order to search for reaction pathways of interest.

Herein this work the development of new methods for automated reaction discovery and their application to exploring transition metal-catalyzed reactions are described. In **Chapter II**, details of the **Group 4** automated reaction discovery method (ZStruct) are laid out, along with its application to exploring previously reported and unreported pathways to methane activation by cisplatin. **Chapter III** extends the application of ZStruct to understanding the more complex reaction of Palladium-catalyzed C-H activation of piperidine, where the roles of the additives, Ar-I and Cs-salt, were identified. In **Chapter IV** the CGen method is described and applied to understanding how polymer chain conformations impact ethylene polymerization with a Ti-constrained geometry catalyst (Ti-CGC), and finally in **Chapter V** the application of CGen to exploring how the presence of a counterion impacts the energetics of monomer uptake and insertion during ethylene polymerization with the Ti-CGC catalyst studied in **Chapter IV**.

CHAPTER II

Automated Reaction Discovery Based on Connectivity Changes

This work partly appears in Reference 97

Abstract

Accurate mapping of chemical reaction mechanisms is of crucial importance towards understanding reaction rate, efficiency, and selectivity. Quantum chemistry is highly effective for producing detailed elementary step mechanisms from first principles. This process, however, requires extensive human effort and chemical intuition to elucidate these mechanisms. In many cases this leads to investigations focusing on only the most promising chemical pathways and neglecting the exploration of new, unknown pathways of chemical importance. To enhance computations ability to search for reaction mechanisms that are not already preconceived by chemists new methods for reaction discovery are needed. Herein the new reaction discovery tool, ZStruct, is described. This method makes use of connectivity rules to define generic chemical reactions which are generally applicable to main group elements. Until recently, these methods were not available for transition metals due to the complex variety of coordination geometries that are possible. By developing a systematic set of rules pertaining to transition metals, reaction discovery can now be used to systematically identify many chemical reactions that are vital to catalysis. These recent developments also extended the methodology to bimolecular reactions, where initial alignment of reactant species is important. These methods utilize the single-ended growing string method for reaction path and transition state searches, giving rise to an automated procedure for mapping chemical reaction pathways in transition metal catalyzed reactions. ZStruct has been applied to methane C-H activation by cisplatin, where previously reported as well as unexplored reaction pathways were found. Additionally, Ni(II)-catalyzed β-hydride elimination was explored and off-cycle Ni(II)-THF and Ni(II)-pyridine complexes were identified as potential thermodynamic sinks.

Introduction

Reaction mechanisms reveal the atomistic details of chemical transformations, provide guidance to increase rates and selectivity, and explain *why* a transformation occurs. Mechanisms therefore have substantial fundamental scientific importance and provide practical value for engineering and optimizing chemical reactions.

Since the advent of quantum chemistry it has been known that computational methods can be used to accurately evaluate the structures and energetics of a sequence of intermediates and transition states in an envisioned reaction mechanism.[1-3] With these powerful tools, researchers in the field of quantum chemistry have been able to best evaluate previously hypothesized, chemically intuited mechanisms in a variety of reactions.[33,41,118] The ability on the other hand to predict chemical reactivity and discover reaction mechanisms to guide experimental design with computation has remained a challenge, especially in newly developing areas of chemistry.

Recent developments are transforming the ability of quantum chemistry to discover reaction mechanisms even without prior chemical intuition. These techniques allow specification of the reactant molecules and catalyst and proceed to determine feasible sequences of elementary reaction steps.[65-67] Unexpected reaction mechanisms[104,106,107,119] can therefore be found at reasonable computational cost, enabling a new paradigm of research in quantum chemistry.

The standard toolkit for computational reaction searches generally utilizes specific reaction coordinates as input to bias reaction exploration towards pathways that are based on hypothetical elementary steps connecting a presupposed reactant-product pair. Additionally, reaction mechanism generation does not systematically search over a comprehensive set of these hypothesized reaction coordinates, and instead focus on a user selected set of reaction coordinates that are determined to be most probable to occur. This reliance on chemical intuition to explore reaction mechanisms limits the ability to discovery new mechanisms and inhibits the predictive capabilities of computational methods.

To overcome the limitations of the standard toolkit for reaction exploration a reaction discovery tool was developed that allows for systematically searching the PES for reaction

pathways based on potential changes in connectivity that can occur between reactants. [65-67,97] The method, called ZStruct, uses a graph-based approach to sample a combinatorial set of hypothetical reaction pathways. ZStruct, named after the Z-matrix type of internal coordinates[120,121], systematically drives reactions to occur in inter- and intramolecular systems using the basic chemical structures of the substrates (and catalyst) as input. The success and efficiency of this procedure is enabled by the growing string method (GSM)[122] which is a low-cost computational tool that reliably constructs a reaction path connecting two intermediates. Recent developments in GSM, namely single-ended Growing String Method (SE-GSM)[109], allows for the location of intermediates, transition states, and minimum energy reaction pathways starting only from the reactant state and a set of reaction coordinates.

Automated Reaction Discovery with ZStruct

The ZStruct procedure for discovering bimolecular reactions involving a transition metal complex and a substrate is outlined in **Figure II.1**. The two species and a selection of their reactive atoms are provided as input, and ZStruct automatically performs the remainder of the reaction discovery. ZStruct thus identifies the basic structure of the metal complex, creates a combinatorial set of reaction driving coordinates (one set shown in **Figure II.1**, bottom right), aligns structures for reaction, and then performs a reaction path search (via SE-GSM) to find the transition state and subsequent intermediate. These intermediates can then be used as input to the next ZStruct run to construct an entire reaction network,[97] including thermodynamic quantities and activation barriers for each elementary step, all without input of reaction coordinates or hypotheses from intuition. Recent work with ZStruct has allowed for the study of systems with ~170 atoms,[100] where up to ~15 of those atoms were selected as reactive. The partitioning of the system into reactive (e.g. catalytic active site atoms) and unreactive atoms (e.g. ligand backbone) is vital to approaching such large systems because the graphical method would otherwise identify more reaction coordinates than could be feasibly computed.

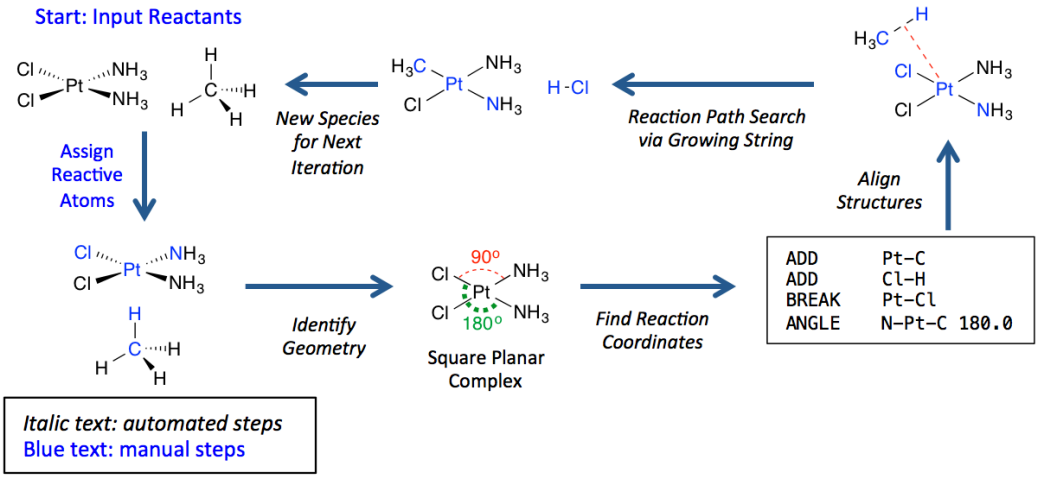

Figure II.1. ZStruct process for reaction pathway discovery.

The generation of driving coordinates can be done by taking advantage of the fact that elements have a set maximum and minimum number of connections (i.e. bonds). By defining the number of connections an atom has initially the number of connections that could potentially change at each atom can be determined. Based on the changes that can occur, bond forming and breaking rules between the user defined reactive atoms can be generated.

When a transition metal center is labeled as reactive by the user, the geometry at the transition-metal center is defined by ZStruct. In order to do this, the number of connections to the metal center is determined and then the angles and distances between each connection on the metal center are calculated. Then based on the number of connections, and the angles between them, the geometry is defined. For example, if a metal center is found to have 4 connections with angles of roughly 90 degrees between the ligands, then the TM center would be labeled as having a square planar geometry. With the gained knowledge of the TM geometry, pre-defined bond forming (add) and bond breaking (break) rules based on the TM geometry are used in addition to the maximum and minimum number of connections for each element to determine what potential bond forming or breaking connectivity changes can occur. An example of these rules with a square planar transition metal center is shown in **Figure II.2**.

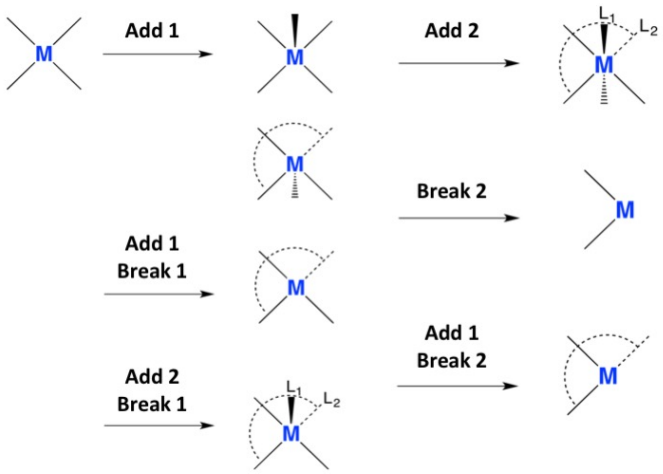

Figure II.2: Potential bond forming and breaking connectivity changes starting from a square planar transition metal center geometry.

Once the bond forming and breaking rules are generated, the reactants can be aligned based on the driving coordinates generated, as shown in **Figure II.3**. The determination of the metal center geometry allows for creating multiple alignments for each set of driving coordinates, where the substrate can be aligned with different faces of the metal center. This allows for the potential to generate different isomers (cis versus trans) of metal complexes to be upon reaction exploration. For example, if an Add 1 connectivity change is modeled at a square planar geometry then two initial structures will be generated. One will have the incoming reactant aligned above the plane of the metal center, and one below the metal center, **Figure II.3 step 3**.

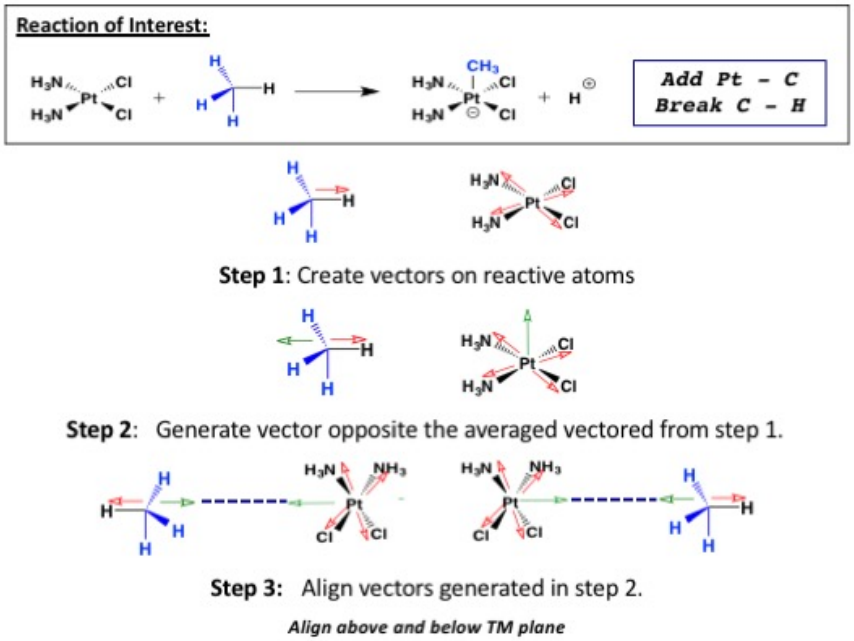

Figure II.3: Generation of alignments with ZStruct

During the alignment process vectors originating from the reactive atom on each molecule are generated. If a connection is breaking at a reactive atom, then a vector is generated in the direction of that break in connectivity. If no connections are breaking, then vectors in the direction of each connection to the reactive atom are generated instead. In step two the vectors from step one are averaged and a new vector in the opposite direction to the average is generated. If the average of the vectors cancel one another out, then a vector orthogonal to connections on the reactive atom is generated. Finally, the vectors from step 2 are lined up with one another to create the aligned structures. Finally, as noted, multiple alignments with different faces of the metal center are generated (e.g. above and below the plane of a square planar geometry.) to allow for pathways to different isomers (cis versus trans ligand orientations) of the metal complexes to be generated upon reaction exploration.

Application of ZStruct to Exploring Methane Activation by Cisplatin

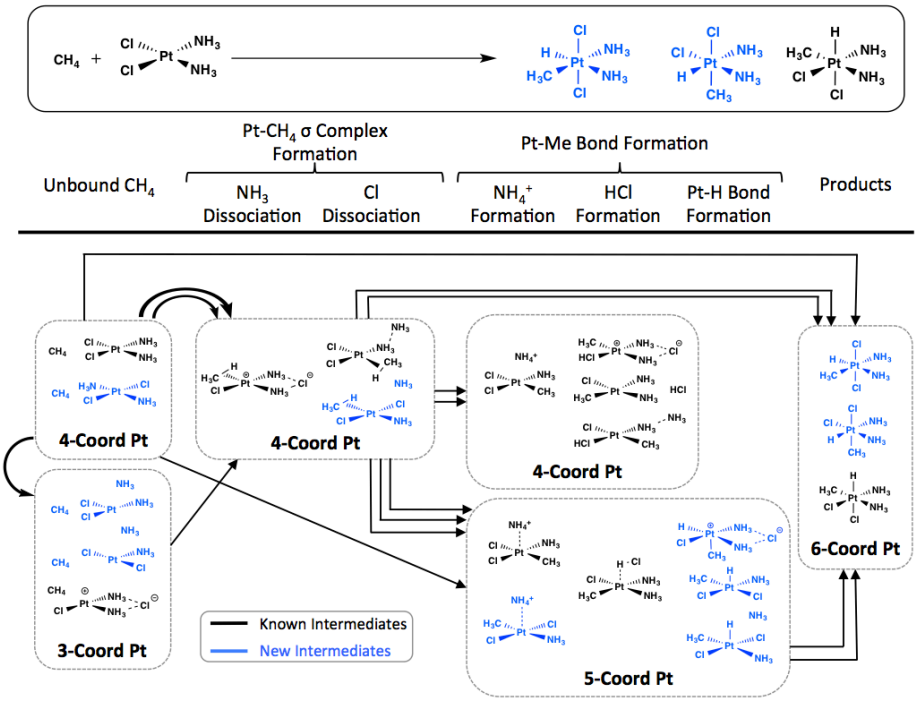

Figure II.4. Reaction networks from ZStruct for methane activation by cisplatin.

To demonstrate the power of ZStruct, it was applied to the reaction of methane with cisplatin ($PtCl_2(NH_3)_2$). This system's activity for C-H functionalization has been examined by experimental[123-126] and computational studies,[127-134] where chemical intuition was used to hypothesize intermediates and reaction pathways. Despite the apparently simple structure of the reaction precursors, this reaction contains significant complexity due to the formation of 3-, 4-, 5-, and 6-coordinate structures enabled by the redox activity of Pt(II/IV). ZStruct was applied to the first two elementary steps of this reaction leading to the oxidative addition product of C-H activation (**Figure II.4**). After screening for low barrier and thermodynamically reasonable reactions, ZStruct's thorough search found 21 intermediates without help from chemical intuition, 10 of which were not previously reported in the literature. This result is especially surprising given that this reaction is particularly well known and well studied. In this case, all of these reaction paths could have been identified using chemical intuition, but the large number

of plausible paths prohibited them from being studied in full using standard simulation techniques. For reactions with less studied mechanisms, unidentified reactive events are even more likely to be found. [104,106,107,119]

Despite the exploration of methane activation showcasing ZStruct's ability to expand the scope of chemical space that can be explored, the models generated are only as good as their ability to capture experimental conditions. Particularly, catalysis reactions are complicated by interactions that occur between additives, solvent, catalysts, and reactants *in situ*, modeling of which can be crucial to understanding and explaining experimental results. As successful as ZStruct is at exploring chemical space, some chemical intuition is still necessary to help and guide ZStruct towards the most optimal section of chemical space to explore. By using chemical intuition and experimental results to provide the relevant reactants, additives, solvent, and catalyst structures as well as their reactive atoms as starting points for ZStruct it allows for an expansive search of chemical space that should be most relevant to the reaction under investigation.

For example in a recent study towards trying to understand why a Ni-catalyzed thiophene-polyolefin co-polymerization reaction was failing to produce co-polymer, experimental knowledge and chemical intuition was needed in addition to ZStruct to determine that solvent (THF) and additive (pyridine) molecules were explicitly needed within the model to better explain experimental results.

Application to Ni(II)-Catalyzed Co-polymerization

Recent work by McNeil and co-workers focusing on a one-pot approach to generate poly(1-pentene)-*block*-poly(3-hexylthiophene) copolymers was found to produce polyolefin monomers and polythiophene monomers instead of the desired copolymer. In order to understand what might be inhibiting the coupling of olefin and thiophene DFT along with ZStruct was used to assess potential pathways blocking coupling from occurring.[108]

For the initial exploration into why co-polymerization was failing, chemical intuition suggested that a β-Hydride elimination pathway from the alkyl bound Ni(II)-diimine cation should be searched for using ZStruct. However, in addition to this, investigating the effect of adding in

THF, pyridine and a new IPr ligand to the system was deemed important as well, as all of these reactants are known to coordinate to Ni. Using chemical intuition to identify important reactants, and ZStruct for reaction exploration a pathway to β-Hydride elimination from the alkyl bound Ni(II)-diimine cation was found, and coordination complexes between the alkyl bound Ni(II) cation and all of the potential reagents (diimine ligand, IPr ligand, THF, and pyridine) were identified. From the insight gained with ZStruct it was determined that β-Hydride elimination could be occurring with the alkyl bound Ni(II)-diimine cation, however the addition of IPr, THF and pyridine to the reaction likely outcompetes β-Hydride elimination, leading to intermediates that can act as unreactive thermodynamic sinks from a catalytic standpoint, **Figure II.5**.

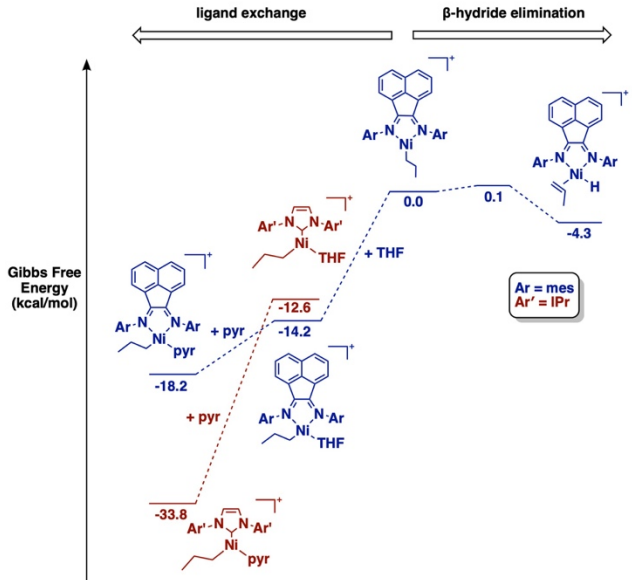

Figure II.5: Gibbs free energy diagram for β-Hydride elimination from the Ni(II)-diimine-alkyl cation species, versus THF/pyridine coordination pre- or post-ligand swap.

The identification of THF or pyridine coordinated intermediates, which are calculated to be downhill in energy by a minimum of 12.6 kcal/mol from the initial alkyl bound Ni(II)-diimine cation, has not been noted experimentally. However, finding these intermediates and generating the hypothesis that these off-cycle Ni(II) complexes could be inhibiting co-polymerization would not have been achieved without the combination of chemical intuition and ZStruct. Chemical intuition was needed to realize that explicit consideration of THF and pyridine was necessary,

while ZStruct was able to find a reaction pathway to β-Hydride elimination and identify the off-cycle intermediates that could potentially be inhibiting co-polymerization.

Conclusions

Chemical reaction mechanisms are powerful conceptual tools, and methods like ZStruct that quickly reveal new mechanisms are therefore extremely useful. This is especially true for exploring chemical reactions where limited experimental data is available to guide computational studies.

As was demonstrated through testing ZStruct on exploring cisplatin catalyzed methane activation, not all pathways will be identified through chemical intuition alone. Within the model generated by ZStruct pathways to elementary steps matching those previously reported and similar to those previously reported, but resulting in different isomers, were found. These pathways may be intuitive to a chemist, but due to computational resources they were not identified in previous studies. The identification of the 21 pathways found for methane activation, without any user guidance, other than the determination of reactive atoms, demonstrates ZStruct's ability to explore a greater scope of chemical space with minimal user involvement.

In contrast though, the investigation into off cycle pathways of Ni(II)-catalyzed copolymerization demonstrated that some chemical intuition is still needed to help guide ZStruct towards experimentally relevant chemical space. By giving ZStruct a starting point with chemical intuition about relevant reactants and experimental conditions the opportunity to do a more expansive search of chemical space for experimentally relevant information becomes a more straightforward task. Additionally, by using ZStruct unprecedented reaction pathways and intermediates can be identified in cases where chemical intuition alone isn't enough to tease out the details of a reaction mechanism to explain experimental results.

In order to see how ZStruct can handle a more complex chemical system that has not been studied previously, it was applied to modeling Pd-catalyzed C-H functionalization of piperidine. The results of the catalytic cycle and the roles that additives play in the reaction, as found with ZStruct, are described in the next chapter.

CHAPTER III

Simulated Mechanism for Palladium-Catalyzed, Directed γ-Arylation of Piperidine

This work largely appears in Reference 107

Abstract

Quantum chemical reaction path finding methods, ZStruct[97] and SE-GSM[109], are herein used to investigate the mechanism of Pd-catalyzed distal functionalization of piperidine, as reported by Sanford.[167] These methods allowed navigation of a complex reaction landscape with multiple reactants interacting at all key steps of the proposed catalytic cycle. A multi-step cycle is shown to conceptually begin with substrate ligation and Pd(II) catalyzed C-H activation, which occurs through concerted metalation deprotonation. In subsequent steps, the kinetic and thermodynamic profiles for oxidative addition, reductive elimination, and catalyst regeneration show why excess Cs salts and ArI were required in the experiment. Specifically, excess ArI is necessary to thermodynamically overcome the high energy of the C-H activated intermediate and allow oxidative addition to be favorable, and excess Cs salt is needed to sequester reaction byproducts during oxidative addition and catalyst regeneration. The overall catalytic profile is consistent with rate-limiting C-H activation, explains the probable functions of all major experimental conditions, and gives atomistic detail to guide experiment to improve this challenging transformation even further.

Introduction

Advances in transition metal-catalyzed C-H bond activation have allowed functionalization of ubiquitous and unreactive carbon centers.[135-140] To achieve selectivity in these transformations, directing groups (DG) are often used to align the C-H bond of interest to the transition metal. [141-151] For instance with alicyclic amines ortho-functionalization is possible through five-membered metallacycles that form between the DG, metal center, and ortho-carbon.[152-154] To expand the scope of bidentate DG functionality[155-158], templates capable of forming macrocyclic transition states[159-166] have allowed for a more diverse range of site selective C-H functionalization. The Sanford Group recently expanded this area further by demonstrating that a bidentate DG could be employed with a flexible substrate, piperidine, to achieve remote arylation at the γ-carbon [167] (**Scheme III.S1**), which is the least likely C-H position to undergo functionalize on this ring**.** This motif successfully avoided arylation of the α- and β-carbons[168-180] despite their higher intrinsic reactivity induced by the N heteroatom and the unfavourability of the chair-boat flip required for γ-carbon activation (**Scheme III.S1**). [181-186] This functionalization was accomplished by using the bidentate DG to align the γ-C-H for preferential activation over the remaining ring sites.

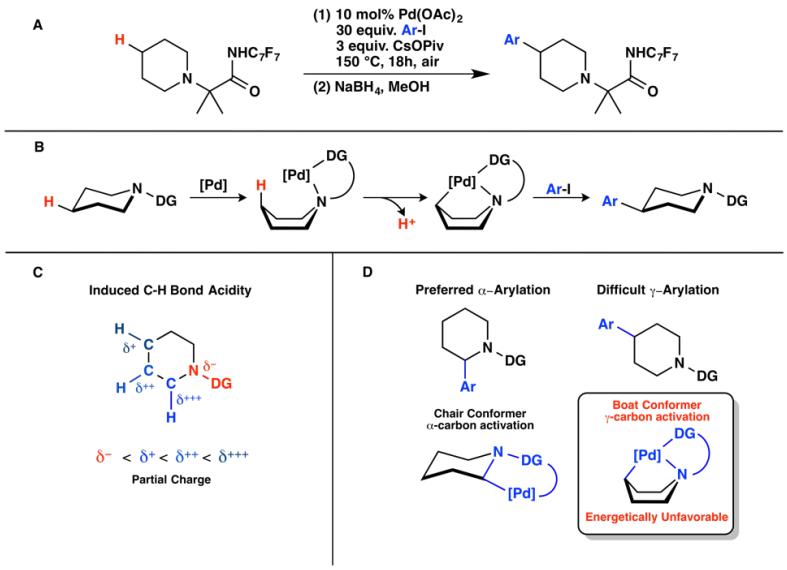

Scheme III.S1: (A) Reaction as reported by Sanford and Co-workers[6], C_7F_7 = 4-CF_3-C_6F_4. (B) Proposed role of piperidine ring flexibility, and bidentate DG in achieving γ-arylation. (C) N atom induced C-H bond acidity. (D) Preferred α-arylation versus γ-arylation and the piperidine conformer required for activation to occur.

Since this directed distal functionalization of piperidine is novel, many aspects of the reaction remain to be better developed. For example, the reaction has a limited substrate scope, including some substrates requiring preactivation of the piperidine via a locked boat conformation. Additionally, temperatures above 130 °C, excess Cesium pivalate (CsOPiv), and excess coupling substrate, aryl iodide (ArI), are required to drive the reaction to provide yields up to 66%.[6] A detailed mechanistic understanding of this reaction should provide insight toward improving yields and designing milder reaction conditions.

In order to give insight into how γ-C-H arylation of piperidine proceeds, density functional theory (DFT) can be used to elucidate elementary reaction steps. This reaction, however, involves multiple reactants and additives as well as a multi-step catalytic cycle that makes mechanistic investigations using DFT challenging. To combat this challenge and explore a variety of potential elementary steps in an expansive manner, the reaction mechanism discovery method discussed in **Chapter II**[97] was used to explore a variety of elementary reaction types to reveal the operative, fundamental reaction steps of the catalytic mechanism. This allowed for a relatively unbiased search of chemical space using driving coordinates for reaction exploration, in contrast to relying primarily on chemical intuition for hypotheses at what transition states or intermediate structures may look like.

Prior quantum chemical studies on transition metal-catalyzed reactions[15,187-198,]involving C-H activation[199-224] have used DFT to explain observed site selectivity[200-205], understand the C-H activation mechanism[206-210], and determine the role of the directing group,[211-215] catalyst[199-210,216,217], additive[218-221] or oxidants[222-224] in the catalytic cycle. Notably, studies by several research groups[200,203,207-209,214,219,225,226] have shown Pd-carboxylate catalysts, such as Pd-acetate ($Pd(OAc)_2$), facilitate C-H activation using the carboxylate base as the proton acceptor. This type of C-H activation was designated by Fagnou and co-workers as "Concerted Metalation Deprotonation" (CMD).[225-227] Based on the insight gained from these previous works and the experimental requirement of a carboxylate base[167], a CMD mechanism is postulated to be operative in piperidine C_γ-H activation.

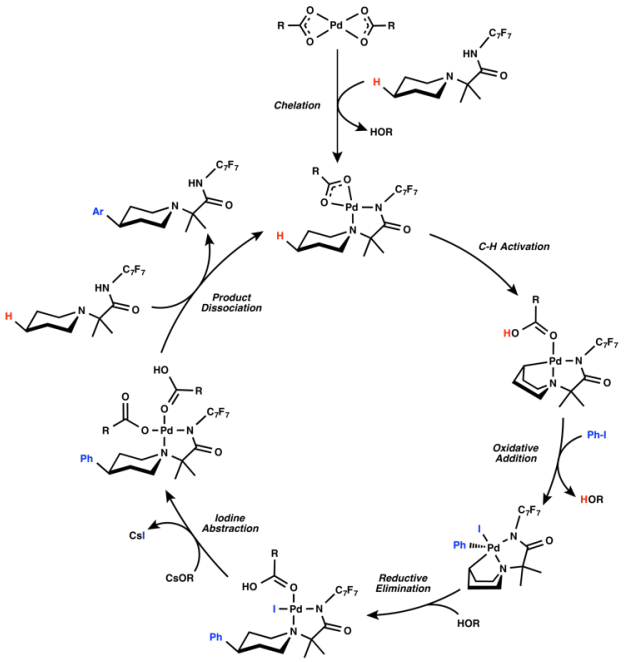

Scheme III.S2: Proposed Pd(II)/Pd(IV) catalytic cycle for C_γ-arylation.

The computational studies in this work have examined the catalytic cycle shown in **Scheme III.S2**, which involves 6 main steps. These steps are (1) generation of the active catalyst through bidentate chelation of the substrate to Pd, which also orients the Pd center near the γ-carbon, (2) C-H activation of the γ-carbon after piperidine undergoes a chair-to-boat conformational switch, (3) oxidative addition of ArI across the Pd(II) center, generating a high valent Pd(IV) species, (4) reductive elimination of the arylated product, (5) iodine abstraction from Pd by CsOAc and (6) product dissociation and chelation of a new substrate at the Pd center to regenerate the active catalyst.

In this chapter, the elementary steps for γ–arylation of piperidine via **Scheme III.S2** are elucidated and described in detail. The challenges associated with this reaction include the unknown chelation mode of the substrate to Pd, the role of additives during oxidative addition and iodine abstraction, and the rate-limiting step(s) of the catalytic cycle. Additionally, the primary roles of CsOAc in effecting kinetically feasible steps for oxidative addition and iodine abstraction are noted. The insight gained from this study should expand the understanding of how γ-arylation occurs while also identifying steps of the catalytic cycle that are important from

a mechanistic standpoint. In addition, this study will lead to a better understanding of how to increase yields and expand the activation of remote C(sp^3)-H bonds to novel chemical systems.

Model System

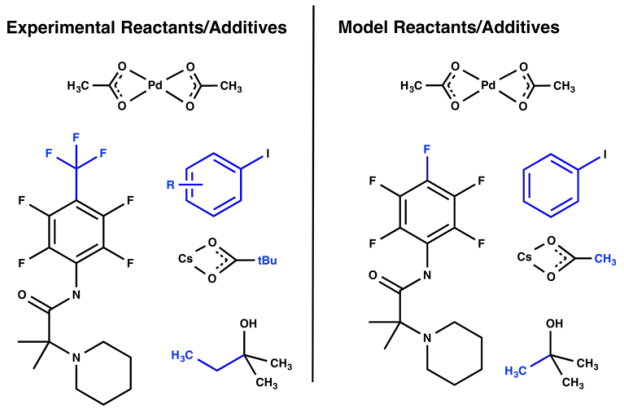

Scheme III.S3: Experimental reactants: Pip-CONHC$_7$F$_7$ substrate (C$_7$F$_7$ = 4-CF$_3$-C$_6$F$_4$), ArI, CsOPiv, Pd(OAc)$_2$, t-AmylOH[6] (left). Model reactants: Pip-CONHC$_6$F$_5$ substrate, PhI, CsOAc, Pd(OAc)$_2$, t-BuOH (right).

Sanford and co-workers optimized their reaction conditions to include Pd(OAc)$_2$, CsOPiv, and either t-AmylOH or ArI (neat reaction) as the solvent (**Scheme III.S3**).[167] In order to keep computations as close to experiment as possible Pd(OAc)$_2$ was modeled without any changes, and the ArI was chosen to be modeled using PhI, which was used experimentally. The substrate, Pip-CONHAr (Ar = 4-CF$_3$-C$_6$F$_4$) was modeled as Pip-CONHAr (Ar =C$_6$F$_5$) due to its similar electronic and steric nature. CsOPiv was truncated to Cesium acetate (CsOAc), due to acetate's similar chemical reactivity. Finally, t-AmylOH was truncated to t-BuOH for the SMD solvent model due to their similar dielectric constants. Due to the excess of pivalate present, C-H activation was also modeled with the experimentally used Pd-pivalate and CONHC$_7$F$_7$ substrate, which is discussed in the C-H activation section of the results.

Results

Thermodynamic Preliminaries

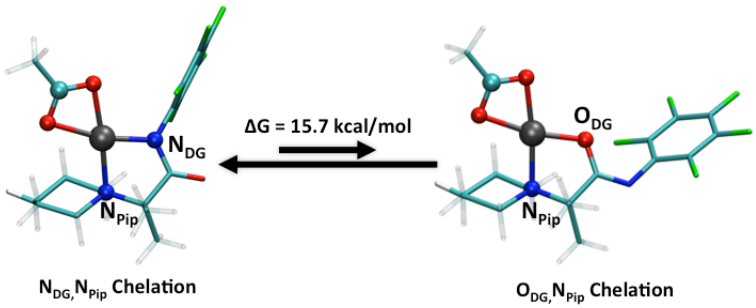

Figure III.1: N_{DG},N_{Pip} (left) versus O_{DG},N_{Pip} (right) chelation modes.

There are two possible modes for bidentate chelation to Pd acetate, one involving the amide nitrogen plus the piperidine nitrogen (N_{DG},N_{Pip}), and the other involving the carbonyl oxygen plus the piperidine nitrogen (O_{DG},N_{Pip}), as shown in **Figure III.1**. These two possible coordination modes of the CONHAr DG were explored to assess their relative stability. Experiments in related systems have shown that either coordination mode is feasible,[228-230] but computations for this system suggest the N_{DG},N_{Pip} coordination is favored by 15.7 kcal/mol. Natural bond orbital analysis showed that the difference in energy is most likely due to the difference in p- and d-orbital interactions between N_{DG}-Pd and O_{DG}-Pd coordination. The N_{DG},N_{Pip} coordination mode gives rise to a N_{DG} p-orbital to Pd d-orbital overlap that is greater than the O_{DG} p-orbital to Pd d-orbital overlap present in the O_{DG},N_{Pip} coordination mode, more details of which can be found in the *Appendix B.* Due to this thermodynamic favorability, only pathways involving N_{DG},N_{Pip} chelation will be discussed in this article.

The challenge of γ-arylation is manifest in the relative reactivity of the three distinct carbon atoms of the piperidine ring in the model substrate, Pip-$CONHC_6F_5$. First, natural charges of the α-, β-, and γ-carbon atoms of piperidine, with the substrate bound to Pd through bidentate N_{DG},N_{Pip} chelation, are -0.109, -0.275, and -0.246, respectively. These charges suggest that the γ-C-H bond is less acidic than the α-carbon, making it a less preferred location for C-H activation (**Figure III.2**). In addition, the energy difference between the chair and boat conformations of piperidine was found to be 7.7 kcal/mol, matching the expected thermodynamic cost of

isomerization.[231] This hinders γ-C-H activation because the less favorable boat conformation is required for a metallacycle to form between Pd and the γ-carbon (**Figure III.3,** structure **A)**. Together, these challenges are evident based on the experimentally observed formation of an aminal product through a competitive reaction at the α-carbon.[167] On the other hand, the bidentate chelating nature of the substrate restricts activation of the α- and β-C-H bonds compared to the γ-C-H bond, by destabilizing the metallacyclizations (**Figure III.3**) that yield three- and four-membered metallacycles for α- and β- activation respectively. The greater ring strain in the three- and four-membered metallacycles favors the formation of the less strained five-membered metallacycle at the γ-carbon (**Figure III.3,** structure **A**). This preference is noted by the fact that the γ-metallacycle is lowest in energy while the α- and β- metallacycles **(Figure III.3,** structures **B** and **C)** have higher relative energies of 2.0 kcal/mol and 3.6 kcal/mol respectively. This small but significant preference to form the five-membered metallacycle, even when the chair-to-boat isomerization is included, is proposed to allow for C-H activation at the γ-carbon to occur. Although the thermodynamics alone suggest that C-H activation at the α- and β-carbon centers is unfavorable the barriers to C-H activation at these three sites were found to be 49.7, 35.3 and 33.9 kcal/mol for α-, β-, and γ-activation respectively (further details can be found in the *Appendix B*.)

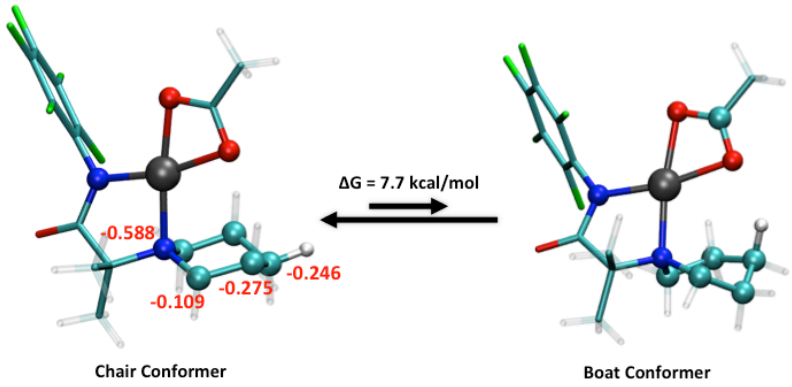

Figure III.2: Conformation change from chair to boat in the model piperidine substrate. Natural charges on the N_{DG}, α-, β-, and γ-carbon atoms of piperidine shown on the left from NBO calculations.

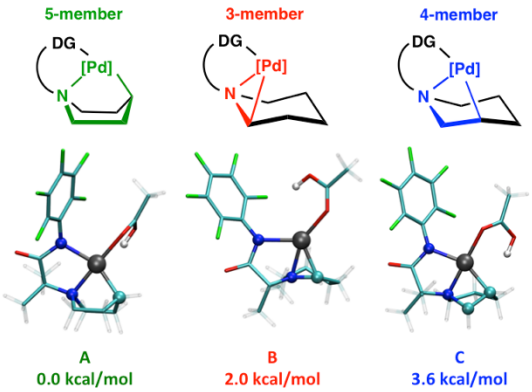

Figure III.3: Optimized structures for the metallacycles (A, B, C) that result from γ-, α-, and β-C-H activation. Energies are Gibbs free energies (413 K) relative to the lowest energy structure.

Catalytic Cycle

N_{DG},N_{Pip} Chelation of $Pd(OAc)_2$

Distal C-H functionalization of piperidine begins with chelation of the substrate, Pip-$CONHC_6F_5$, to $Pd(OAc)_2$ in a multi-elementary step sequence (**Figure III.4**). This chelation process leads to two intermediates with N_{DG},N_{Pip} binding that are thermodynamically stable precursors for C-H activation. In the first intermediate, **4**, κ^1-acetate and κ^1-acetic acid ligands are coordinated to Pd, and in the second intermediate, **5**, acetic acid dissociates leaving only a κ^2-acetate ligand bound to Pd (**Figure III.5**).

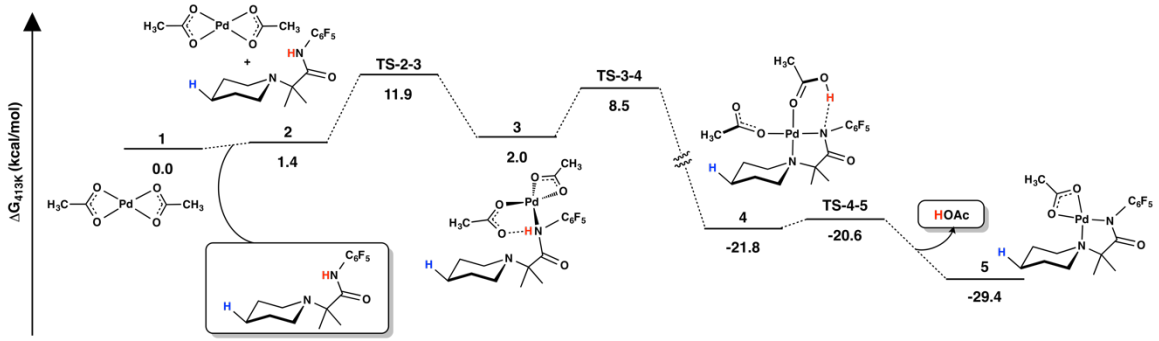

Figure III.4: Pathway for chelation of $Pd(OAc)_2$ to the substrate Pip-$CONHC_6F_5$. All energies are referenced to separate reactants at **1** ($Pd(OAc)_2$, PhI, CsOAc, and Pip-$CONHC_6F_5$).

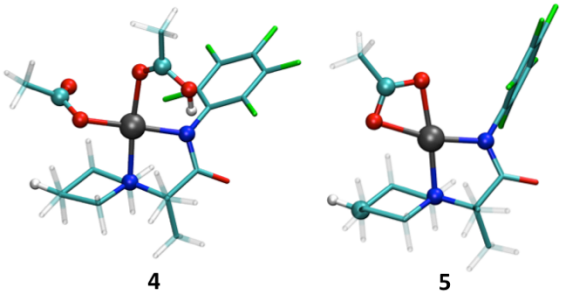

Figure III.5: Chelated intermediates that can undergo C-H activation (left) **4** and (right) **5**.

In order to form **4** and **5**, Pd-acetate and Pip-CONHC$_6$F$_5$ first come together into a reaction precomplex, **2**, in which Pd is oriented such that the empty axial coordination site on Pd faces the amide nitrogen, N_{DG}, (**Figure III.4**). Intermediate **4** is then formed through a facile two-step process from **2**. In the first step, an oxygen of a κ^2-acetate ligand on Pd is replaced by N_{DG} with a barrier of 11.9 kcal/mol through **TS-2-3**. The acetate's displaced O forms a hydrogen bond with the amide proton leading to **3**, which lies 2.0 kcal/mol uphill from **1**. The chelation of Pd to N_{DG} leaves an open axial site oriented directly above N_{Pip}, poising it for coordination. In the second step, **TS-3-4**, the H-bonding interaction leads to deprotonation of N_{DG} by acetate's unligated O. During this proton transfer the Pd coordinates to N_{Pip} causing an oxygen of the κ^2-acetate ligand to be displaced. This step has a barrier of only 8.5 kcal/mol and leads to **4**, which is downhill 23.8 kcal/mol from **3**. The stability of **4** can be attributed to the five-membered metallacycle that forms when Pd coordinates to N_{DG} and N_{pip}. In addition, the free O of acetate and the OH of acetic acid are aligned towards opposite faces of the square-planar Pd center, allowing the OH of acetic acid to form an intramolecular H-bond with $N_{DG.}$ From **4** the displaced O of the κ^1-acetate ligand can rebind, displacing the acetic acid ligand with a barrier of 1.2 kcal/mol (**TS-4-5**), forming **5**, which is more stable than **4** by 7.6 kcal/mol. Each of the steps identified for chelation are facile and the step interconverting between **4** and **5** is reversible, meaning that intermediates **4** and **5** (**Figure III.5**) are in equilibrium, and each has the potential to undergo C-H activation.

C-H Activation

From either intermediate **4** or **5** γ-C-H activation can occur through either an outer sphere or inner sphere mechanism, which have been noted in previous DFT studies of C-H activation.[232-

[238] Both mechanisms result in the formation of a five-membered metallacycle involving N_{Pip}, Pd, and C_γ (**Figure III.3**, structure **A**). While pathways for C-H activation from **4** and **5** were each found to involve a CMD mechanism, the pathway from **4** occurs through an outer-sphere deprotonation involving acetic acid and acetate, whereas the pathway from **5** occurs through an inner-sphere deprotonation involving only the κ^2-acetate ligand (**Figure III.6**).

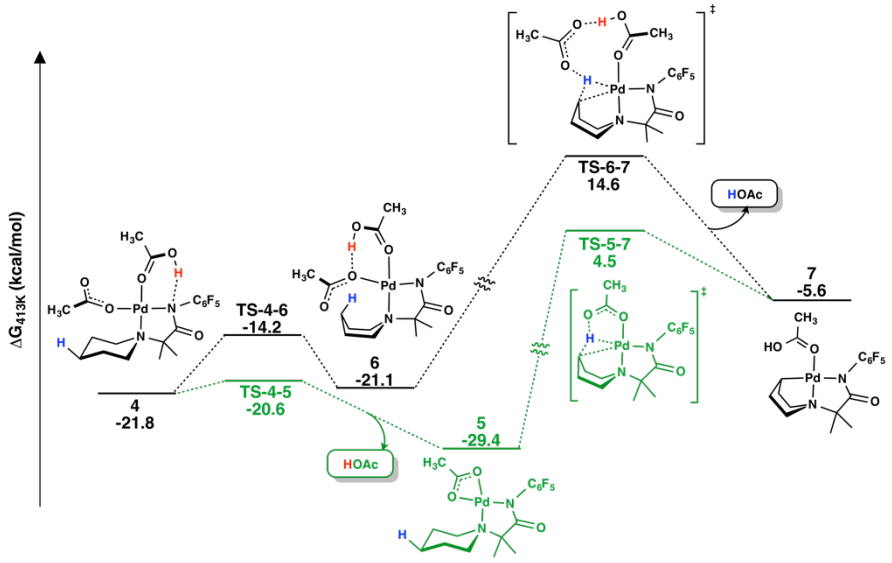

Figure III.6: C-H activation from intermediates **4** (black) and **5** (green). Energies are referenced to separate reactants (i.e. **1** from **Figure III.4**).

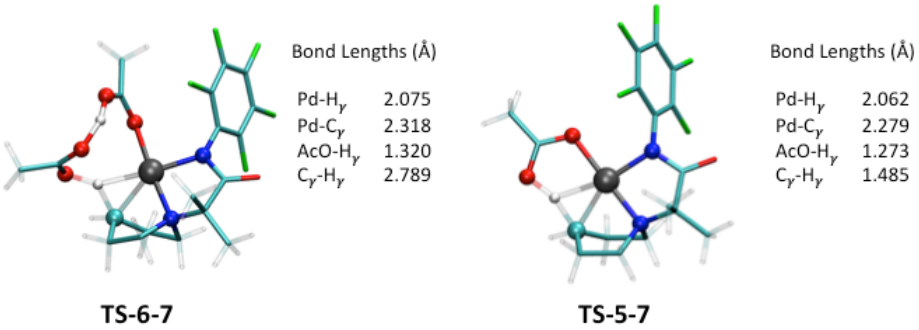

Figure III.7: Transition state structures and key bond distances for C-H activation from (left) **4** and (right) **5.**

Starting from **4**, γ-carbon activation occurs through a two-step process shown in **Figure III.6**, with a rate-limiting transition state (**TS-6-7**) shown in **Figure III.7**. In the first step, **TS-4-6**, the H-bond between the κ^1-acetic acid ligand and N_{DG} breaks and allows the OH to rotate towards

the κ^1-acetate ligand and form a new H-bond with the ligated O of acetate. In concert with this step the piperidine ring isomerizes to a boat conformer, orienting the γ-C-H towards the free O of acetate. This isomerization decreases the distance between the free O of the κ^1-acetate ligand and the γ–carbon hydrogen from 3.99 Å to 2.18 Å as well as the distance between Pd and the γ–carbon from 4.20 Å to 3.51 Å, which are necessary for C-H activation to occur. This concerted rotation and isomerization is facile and reversible with a barrier of 7.6 kcal/mol (**TS-4-6**) and leads to **6**, which is 0.7 kcal/mol higher in energy than **4**. The similar energetics of these two structures, despite piperidine isomerization, is due to stabilization from H-bonding between the acetic acid and the acetate ligand. In the second step, **TS-6-7** (**Figure III.7**), the κ^1-acetate ligand dissociates from Pd to generate an empty coordination site on Pd for binding the γ–carbon. (An alternate path involving dissociation of the acetic acid ligand would be unfavorable due to the open coordination site on Pd being further from the γ-carbon that needs to coordinate to Pd.) During C-H activation the H-bonding interactions present between the κ^1-acetate and κ^1-acetic acid ligands keeps the free acetate in close proximity to the Pd and γ–carbon, allowing the free acetate to act as a proton acceptor during C-H activation. Therefore, C-H activation occurs via Pd-assisted proton transfer from the γ–carbon to acetate as the Pd-γ–carbon bond forms (**TS-6-7**), leading to **7**, which is uphill 16.2 kcal/mol from **4**. The high energy of the C-H activated intermediate also entails a high barrier to C-H activation of 36.4 kcal/mol. The new intermediate, **7**, has a square planar Pd center bound to N_{DG}, N_{Pip}, C_γ and a κ^1-acetic acid ligand. The instability of **7** can be attributed to increased ring strain presented by the second five-membered metallacycle that forms between Pd, N_{DG}, N_{Pip}, and $C_{\boldsymbol{\gamma}}$ as well as the destabilization of the Pd-N_{DG} interactions caused by the $C_{\boldsymbol{\gamma}}$–Pd bond that forms. This destabilization is evident based on the elongation of the Pd-N_{DG} bond from 2.00 Å to 2.14 Å as well as the change in natural bond charge on Pd and N_{DG} from 0.795 a.u. and -0.637 a.u. to 0.621 a.u. and -0.729 a.u. respectively, indicating decreased electron donation to Pd from N_{DG}.

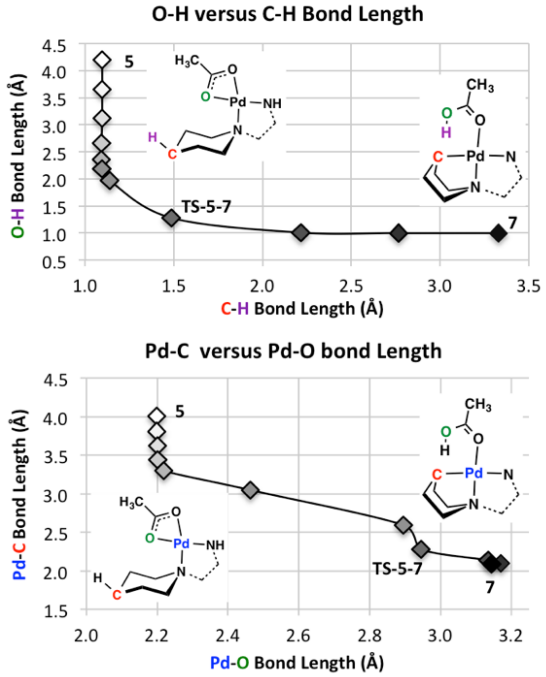

Figure III.8: Key bond lengths along the path for C-H activation, converting **5** to **7** through **TS-5-7.**

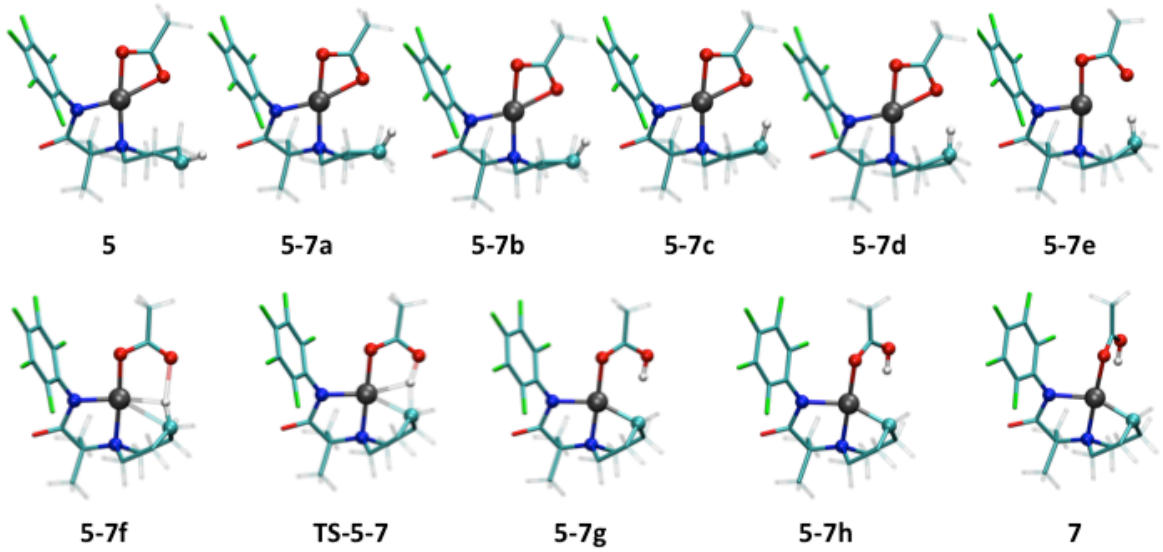

Figure III.9: Snapshots along the pathway for C-H activation from **5** to **7**.

In contrast to the C-H activation pathway from **4**, the pathway from **5**, shown in **Figure III.6**, occurs through a single elementary step. This step involves piperidine isomerization from a chair to boat conformation as the κ^2-acetate O that is in closer proximity to the γ-carbon dissociates from Pd (**TS-5-7, Figure III.7**). (A two-step mechanism in which piperidine

isomerization occurs followed by subsequent C-H activation was also investigated and led to the same C-H activation transition state, the details of which can be found in the *Appendix B*). In this concerted asynchronous process, the piperidine ring isomerizes to its boat conformation prior to the acetate O dissociating from Pd. As the isomerization occurs the Pd-O bond begins to lengthen from 2.198 Å in **5-7c** to 2.463 Å in **5-7e**, both shown in **Figure III.9** with bond distances shown in **Figure III.8**. The isomerization changes the orientation of the γ–C-H from facing away from Pd, **5**, to facing towards Pd and the acetate ligand (**5-7e**), thus allowing C-H activation to occur by decreasing the Pd-C_{γ} distance from 4.01 Å to 3.05 Å and the Pd-H distance from 4.63 Å to 2.58 Å in structure **5** and structure **5-7e** respectively. Upon isomerization the Pd-O bond breaks, allowing Pd to coordinate to the γ–carbon and γ–hydrogen (**5-7e** and **5-7f**). This coordination enables Pd to facilitate the proton transfer to the newly un-ligated O of acetate through **5-7f** and **TS-5-7** and bind to the γ–carbon, **5-7h**. Finally, the newly formed κ^1-acetic acid ligand rotates out of the square plane of the Pd to avoid steric interactions between the OH and the Pd-γ-carbon bond (**5-7g, 5-7h,** and **7**). The rate-limiting barrier to this step is 33.9 kcal/mol (**TS-5-7**) and results in **7**, which is uphill 23.8 kcal/mol from **5.**

TS-6-7 and **TS-5-7** (**Figure III.7**) show that C-H activation occurs through a sequential chair-boat isomerization and CMD mechanism. The barrier to C-H activation through **TS-5-7**, where no acetic acid is present, is 2.5 kcal/mol lower in energy than C-H activation through **TS-6-7** making the two steps competitive paths to the resulting intermediate, **7**. Once the C-H activation intermediate, **7**, is formed the catalytic cycle continues on to PhI coordination and subsequent oxidative addition, followed by C_{γ}-C_{Ph} coupling through reductive elimination, as described in the next two sections.

Having explored the key C-H activation event using a model substrate and CMD acceptor, the same reaction was explored using Pd-pivalate and the experimental substrate, which contains a 4-CF_3-C_6F_4 Ar group (**Scheme III.S3**). These substitutions bring the model closer to the experimental setup, where the excess CsOPiv allows pivalate to replace acetate at the Pd center during catalysis. The rate-limiting C-H activation reaction with κ^2-carboxylate assisted CMD using pivalate and the 4-CF_3-C_6F_4 arene ring is shown in **Figure III.10**.

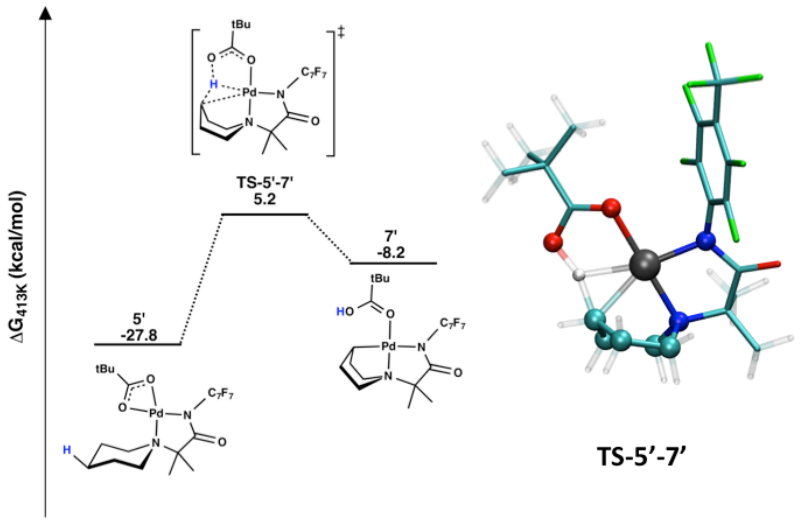

Figure III.10: Energy profile for Pd-pivalate catalyzed C-H activation with a 4-CF_3-C_6F_4 arene ring on the DG (Left). Transition state structure for C-H activation. Energies referenced to the reactants, Pd-pivalate and Pip-$CONHC_7F_7$.

Starting from **5',** the same CMD mechanism from the model system was found to be operative, showing a single elementary step from chair conformation of the ligated DG to form the Pd-C bond through **TS-5'-7'**. The barrier to C-H activation is 33.0 kcal/mol and leads uphill 19.6 kcal/mol. This barrier is lower than with the acetate model, and leads to a more stable C-H activation intermediate, suggesting that the reaction with pivalate should proceed more readily than with acetate, which agrees with the experimental observation of the same effect.[6] Regardless, the rate-limiting C-H activation mechanism is qualitatively similar for the experimental system as to the model, supporting the further use of the model system for investigation into the remaining steps of the catalytic cycle.

Oxidative Addition of PhI across Pd(II)

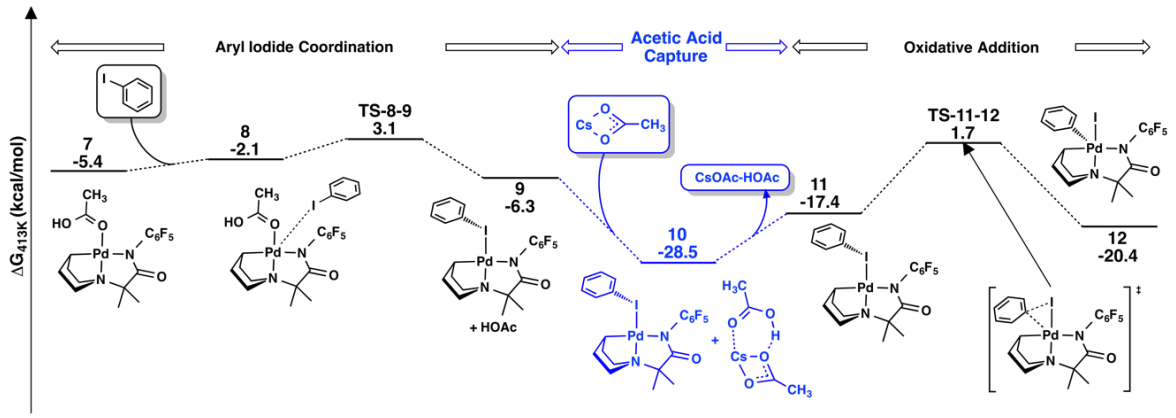

Figure III.11: Coordination of PhI and oxidative addition to generate Pd(IV). Energies are referenced to separate reactants (i.e. **1** from **Figure III.4**).

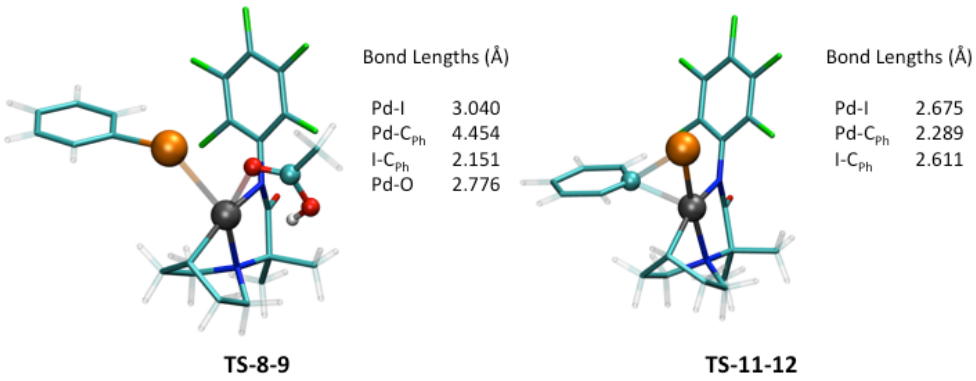

Figure III.12: Transition states for PhI coordination (left) and oxidative addition of PhI (right).

The next step of the catalytic cycle generates high valent Pd(IV) via coordination and oxidative addition of PhI. This process begins with the complexation of PhI to **7** to give **8**, which is 3.3 kcal/mol uphill (**Figure III.11**). From **8** a three-step process leading to oxidative addition was found. In the first step a facile ligand swap reaction, where PhI displaces the κ^1-acetic acid ligand, occurs with a barrier of 5.2 kcal/mol above **8** (**TS-8-9** of **Figure III.12**). During this step iodine coordinates to Pd to produce **9**, a square planar Pd complex with N_{DG}, N_{Pip}, iodine, and C_γ ligands, which is downhill 4.2 kcal/mol from **8**. (A pathway to form a Pd-π complex between PhI and Pd was found to be higher energy, the details can be found in the *Appendix B*.) Although this step is facile when referenced to **8**, it has a barrier of 32.5 kcal/mol when referenced to the lowest

energy intermediate prior to this step, **5**. This high barrier makes PhI coordination a kinetically slow step that could be made more favorable by the presence of excess PhI.

From **9**, immediate oxidative addition has a barrier of 40.4 kcal/mol when referenced to the lowest energy intermediate, **5**, making it energetically infeasible (see *Appendix B* for details). In order to bypass this high barrier, the role of CsOAc on oxidative addition was explored. Addition of CsOAc to **9** leads downhill 22.2 kcal/mol to **10** through CsOAc sequestering acetic acid (displaced during PhI coordination). Coordination of CsOAc to acetic acid also inhibits the reverse ligand swap reaction in which acetic acid replaces iodine transforming intermediate **9** back into **8**. Removal of the CsOAc-HOAc cluster from the simulation leads uphill 11.1 kcal/mol to **11**, which has Pd coordinated to iodine, C_{γ}, N_{DG}, and N_{Pip}.

From **11** the oxidative addition pathway, **TS-11-12**, shown in **Figure III.12**, was found where the Ph group adds into the axial position on Pd *cis* to C_{γ} while iodine remains in its equatorial position, leading to **12.** The barrier for this pathway is 19.1 kcal/mol above **11**, but 31.1 kcal/mol above **5**, the lowest energy intermediate prior to this step. This oxidative addition step is the same as is operative without the inclusion of CsOAc. The stabilization of **10** caused by CsOAc sequestering acetic acid makes this oxidative addition step to form the high valent Pd(IV) intermediate energetically feasible but kinetically slow. This step is likely sped up by the presence of excess ArI, to make Pd-I coordination more favorable, and Cs-salt, to make acetic acid sequestration more favorable. Intermediate **12** is 3.0 kcal/mol downhill from **11** and has square pyramidal Pd(IV) bound to C_{γ}, C_{Ph}, iodine, N_{DG} and N_{Pip}. This structure is expected to undergo facile reductive elimination in order to generate a more stable Pd(II) intermediate.

The high barriers for PhI coordination and oxidative addition (**TS-8-9**, 32.5 kcal/mol, and **TS-11-12**, 31.1 kcal/mol, each compared to **5**) makes these steps kinetically slow, however, the pathway from **8** to **12** (**Figure III.11**) suggests that higher concentrations of PhI and CsOAc should increase the reaction rate and bias the thermodynamics towards the formation of **12**. This conclusion agrees with experiment, which requires the presence of excess PhI and CsOPiv[167], suggesting the difficulty of these steps. Thus, it is proposed that the presence of excess additives should act as a driving force for these two steps, inherently lowering the barriers making each step energetically feasible and non rate-limiting.

Reductive Elimination

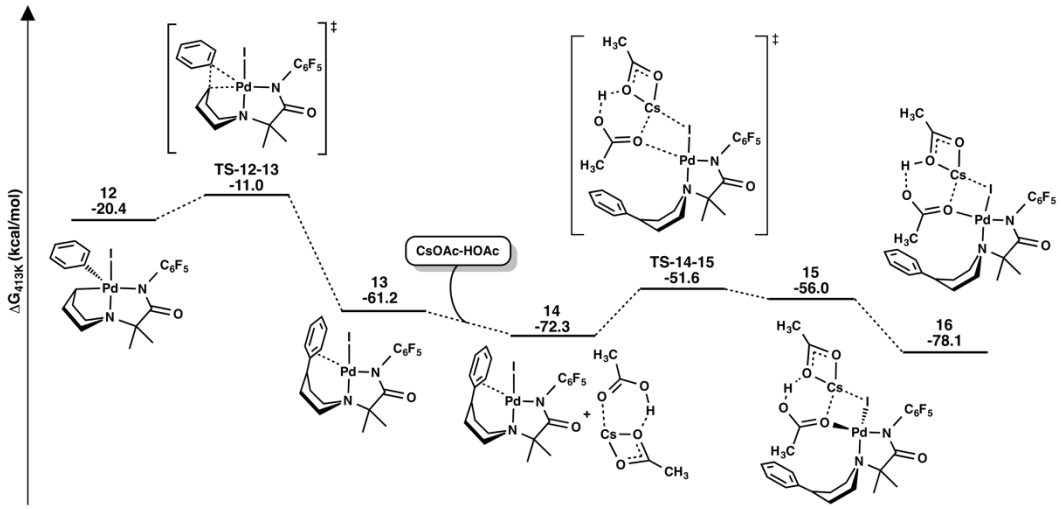

Figure III.13: Reductive elimination pathway leading to the bound arylated product. Energies are referenced to separate reactants (i.e. **1** from **Figure III.4**).

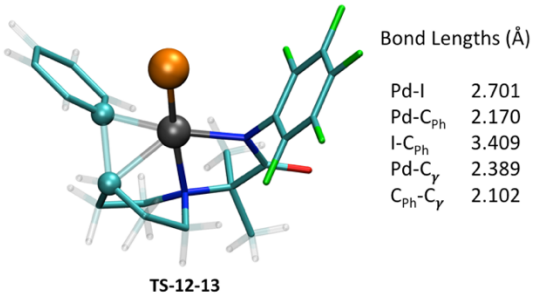

Figure III.14: Transition state for reductive elimination, **TS-12-13**, and key bond lengths.

Reductive elimination from **12** (**Figure III.13**) occurs through **TS-12-13** (**Figure III.14**) with a barrier of 9.4 kcal/mol to give **13**, which is downhill 41.3 kcal/mol from **12.** This step to form the arylated product is favorable due to the formation of the C_{γ}-C_{Ph} bond and reduction of Pd(IV) back to a more stable Pd(II) complex. After C_{γ}-C_{Ph} bond formation the Pd-Ph π-interaction that persists in **13** can be broken up by coordination of acetate (from the CsOAc-HOAc cluster or another CsOAc) to the Pd center. Addition of CsOAc-HOAc to **13** results in **14** which is 11.1 kcal/mol downhill. Acetic acid then associates to Pd through **TS-14-15** with a barrier of 20.7 kcal/mol, which leads 16.3 kcal/mol uphill to the tetrahedral Pd(II) complex, **15** (**Figure III.15**). **15**

is metastable and isomerizes to a square planar Pd(II) complex, **16** (**Figure III.15**), which is downhill 22.1 kcal/mol from **15**. While the product of C-H functionalization has been formed at intermediate **13**, iodine abstraction from Pd and subsequent dissociation of the arylated product from Pd need to occur to regenerate the active catalyst.

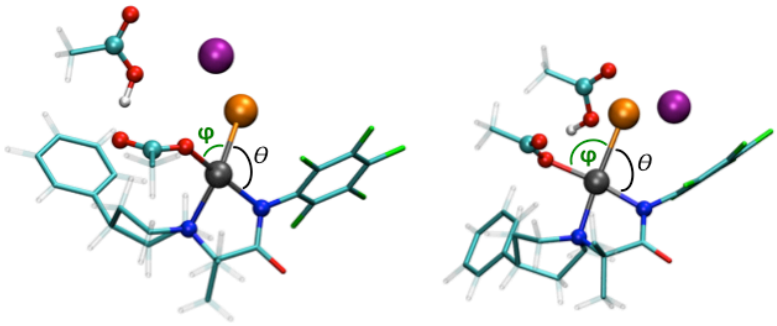

Figure III.15: Post reductive elimination complexes: (left) tetrahedral, **15,** versus (right) square planar, **16**, geometries. The angles, ϕ (I, Pd, O angle) and θ (I, Pd, N_{DG} angle) distinguish between the two metal center geometries.

Product Dissociation and Active Catalyst Regeneration

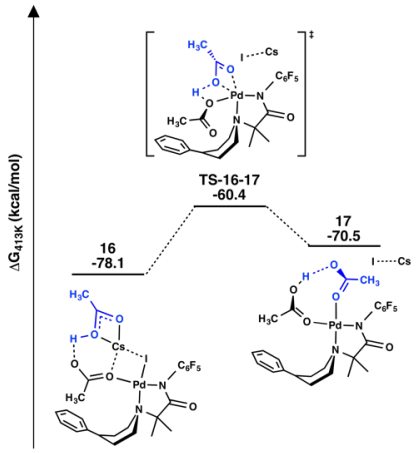

Figure III.16: Iodine abstraction from Pd by CsOAc. Energies are referenced to separate reactants (i.e. **1** from **Figure III.4**).

Regeneration of the active catalyst can be accomplished by iodine abstraction from Pd followed by substitution of the arylated product with an unactivated substrate. The iodine

abstraction occurs in a single ligand swap step where the acetic acid coordinated to Cs displaces the iodine ligand through **TS-16-17** (**Figure III.16**). The barrier to this step is 17.7 kcal/mol and leads uphill 7.4 kcal/mol to **17.** During this ligand swap step the H atom of acetic acid is transferred to the acetate ligand already coordinated to Pd, and results in a H-bonding interaction between the two ligands (**TS-16-17, Figure III.17**). To facilitate this dissociation the Cs cation coordinates to the free iodine anion that is displaced from Pd. Iodide dissociation without the assistance of Cs acetate is unfavorable with a barrier of at least 28.6 kcal/mol (see *Appendix B* for pathways without Cs acetate), suggesting that the presence of Cs (or another cation) is needed for this step to proceed in an energetically feasible process. The formation of an insoluble Cs-iodide salt likely provides a thermodynamic driving force to move the catalytic cycle forward.[167]

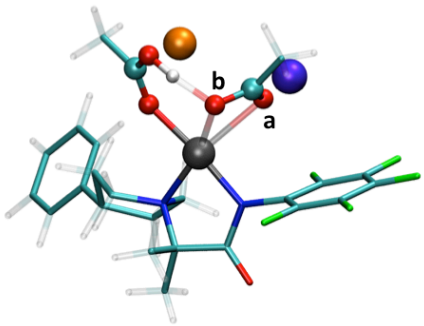

Bond Lengths (Å)	
$Pd\text{-}O_{AcO(a)}$	2.519
$Pd\text{-}O_{AcO(b)}$	2.539
$H\text{-}O_{AcOH}$	1.031
$H\text{-}O_{AcO}$	1.545
Pd-I	5.258
I-Cs	3.732

TS-16-17

Figure III.17: Transition state for iodine abstraction and CsI formation **TS-16-17**.

Experimental observation of the free arylated product suggests that from **17** product dissociation is feasible.[167] To understand this process and close the catalytic cycle, the thermodynamics of the substrate and product binding to Pd as well as the possibility of Pd-acetate regeneration and product dissociation were studied. Having Pd bound to the product (**18**, **Figure III.18**) is 0.2 kcal/mol less stable than Pd being bound the substrate (**19**, **Figure III.18**) both with N_{DG},N_{Pip} bidentate chelation. This thermoneutrality suggests that swapping the product for a new substrate is plausible but does not occur with a strong driving force. In contrast having Pd-bound to the product, **18**, is 23.9 kcal/mol more stable than product dissociation and Pd-acetate

reformation (**20**, **Figure III.18**). This difference in thermodynamics suggests that the ligand swap reaction is the preferred mechanism to regenerate the active catalyst. This ligand swap generates an intermediate similar to **4**, the only difference being with respect to the orientation of the κ^1-acetic acid and κ^1-acetate ligands. In **18** and the subsequent substrate chelated intermediate, **19**, the κ^1-acetic acid ligand is H-bonded to the ligated O of the κ^1-acetate ligand, whereas in **4** the κ^1-acetic acid ligand is H bonded to N_{DG} instead. Therefore, **19** is just an isomer of **4**, and should be able to restart the catalytic cycle for C-H functionalization.

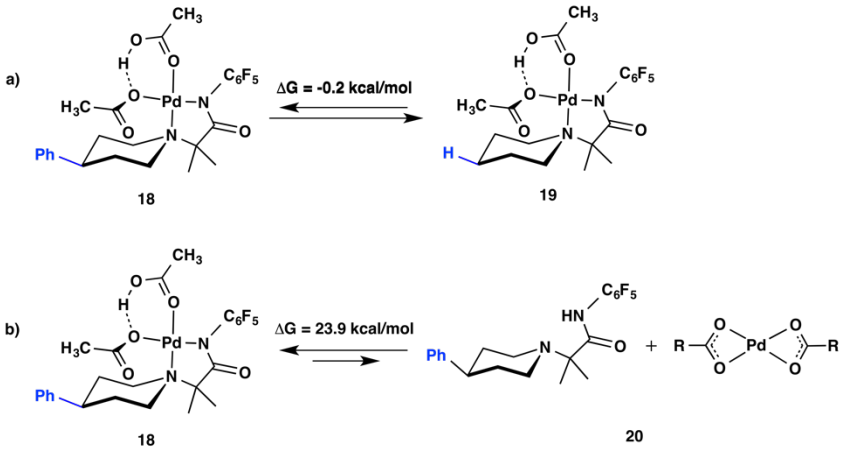

Figure III.18: (a) Equilibrium between Pd(OAc)(HOAc) chelated to the product (left) versus the substrate (right). (b) Equilibrium between Pd(OAc)(HOAc) chelated to the product (left) versus product dissociation and Pd-acetate reformation (right).

Discussion

Selective, remote functionalization of C(sp^3)-H bonds of alicyclic amines is challenging due to the multitude of difficult chemical steps that must be enacted in sequence. Atomistic details of γ–functionalization of piperidine show how combining a bidentate directing group with a flexible substrate can align the remote C(sp^3)-H bond near the metal center and allows for activation of bonds that would otherwise be considered unreactive. This is not the only challenging reactive step. Overall, the quantum chemical studies discussed in this work have shown the following unknown or unexpected details of the mechanism outlined in **Scheme III.S2**:

I. A multistep substrate chelation to attach the DG through N_{DG} and N_{pip} moieties.

II. Asynchronous, yet concerted piperidine isomerization to the boat conformer and C-H activation of the γ-carbon through a CMD mechanism.
III. A high energy C-H activated intermediate must be trapped by oxidative addition of ArI.
IV. One role of the Cs salt is that it aids in allowing interchanges to occur that are required for completion of key steps, such as oxidative addition and iodine abstraction to regenerate the active catalyst.
V. The regeneration of Pd acetate is not expected to occur, due to its relatively high thermodynamic energy, but the product should be displaced by a new substrate's DG to restart the catalytic cycle.

Having uncovered this detailed picture of the mechanism for piperidine γ–functionalization through Pd(II) enabled C-H functionalization, oxidative addition, and reductive elimination (**Scheme III.S2**), the key mechanistic steps that plausibly limit the overall cycle are now available. In addition to this some of the potential roles of the Cs salt and excess aryl-iodide have been identified, such as their roles in driving forward aryl-iodide coordination and oxidative addition steps of the reaction. Despite this, the solvation of Cs in solution is not well understood, and fully modeling the first solvation shell remains a challenge[239] due to Cesium's ability to coordinate to the substrate, carboxylate bases and aryl-iodide in solution. Regardless, it was found that in the first third of the cycle, C-H activation is clearly rate-limiting, and accelerated by the use of CsOPiv compared to CsOAc. Post C-H activation, the high energy of the C-H activated intermediate makes the subsequent steps appear to have unexpectedly high barriers. Without excess PhI or CsOAc to drive the reaction forward, these could be slow steps, but they are not likely rate-limiting under the high loadings that were used in experiment.[167] This mechanistic investigation into the full catalytic cycle and potential roles of additives in C-H functionalization showcases the complexities of the interplay between multiple reactants taking part in a variety of elementary steps leading to the production of arylated products.

Conclusions

In summary, this work describes a detailed mechanism for the Pd-catalyzed directed γ-carbon C-H activation and subsequent arylation of piperidine identified using DFT and ARF methods. The goal of this work was to provide explanations for three main questions: What is the rate-limiting step(s) of the reaction? What mechanism does C-H activation occur through? and, Why are excess additives needed to drive the reactivity? Answers to these three questions were uncovered for the overall reaction mechanism shown in **Scheme III.S2,** although the possibility that catalysis could occur through a qualitatively distinct cycle is left open.

The identification of three catalytic steps with relatively high activation barriers shows the importance of looking at the entire mechanism for C-H functionalization reactions, rather than just focusing on single steps, like C-H activation. Through the investigation of the full cycle, probable roles of the Pd-carboxylate catalysts, aryl iodide oxidants, and salt additives were identified, giving rise to explanations for why such reagents are required for productive catalysis. Although exploring the full complexity of this chemical transformation still remains computationally challenging, the approach used in this work gives rise to substantial insight into how the substrate, catalyst, and additives interact to drive product formation. The hope is this insight will be used to guide future studies to examine and explain such complexities, in order to provide more complete mechanistic understanding of emerging catalytic transformations.

CHAPTER IV

The Role of a Flexible Polymer in Olefin Chain Growth via Constrained Geometry Catalysts

Abstract

Conformational flexibility is a universal feature of all molecules with rotatable bonds. Particularly polyethylene chains can be very flexible due to the large number of sigma bonds that can rotate. Despite the known flexibility of these polymer chains, the impact of their conformational changes on monomer insertion has not been studied in detail. Here a new method is described for systematically generating reactant conformers and binding them to a transition metal-catalyst of interest from which monomer insertion can be modeled using the single-ended Growing String Method (SE-GSM). Herein, this method was applied to studying how the lengthening of polyethylene during olefin chain growth with a Ti-constrained geometry catalyst ($Cp^*SiMe_2NC(CH_3)_3Ti\text{-}R^+$) impacts the reaction pathway to monomer insertion for systems with R = CH_3, C_3H_7 and C_5H_{11}. The conformer generation method leads to the generation of 1, 4, and 46 conformers of $Cp^*SiMe_2NC(CH_3)_3Ti\text{-}R^+$ complexes for each respective step of monomer insertion. From the conformational search, it is found that the energetic barrier to monomer insertion is higher for the first insertion step compared to the second and third steps. Further analysis of the transition state (TS) structures sampled at each step show that the mechanism to monomer insertion is qualitatively the same regardless of the increase in chain length or change in polymer chain conformation. Additionally, when the most favorable pathways are looked at for insertion with R = C_5H_{11}, the most stable initial and TS structures tend to maximize the distance between the Ti center and polymer chain carbon atoms not coordinated to Ti.

Introduction

As discussed, reaction exploration using quantum chemistry has become a powerful tool for examining and explaining reaction rates and selectivity.[1-3,33,41,118] As described in **Chapter I**, automated reaction discovery tools, namely ZStruct[97] and the single-ended Growing String Method (SE-GSM[109]) are particularly useful in mapping potential reaction mechanisms and evaluating their feasibility without relying heavily on prior chemical knowledge. While these methods explore the changes in covalent bonding that represent the rate-limiting steps of chemical transformations, less attention has been paid to the conformational degrees of freedom that also are important to describing reactions. In particular, reaction discovery tools that start from a single initial conformer can only find reaction pathways from that conformer, limiting the scope of information and knowledge that might be gained through the search.

Conformational flexibility is a structural feature present in all molecules that have rotatable bonds. Accounting for this flexibility by investigating the scope of conformers that could exist is a non-trivial task, especially in systems where numerous rotatable-bonds are present.[110-115] Generally, this means that quantum chemical studies of molecules with a high degree of flexibility tend to utilize truncated models,[101,108,240-242] assume the use of a single conformer of the molecule, based on experimental X-ray or crystal structure data when available, [243-251] or use a set of chemically intuitive conformers generated by hand. [252-265] Since all energetics and predictions of chemical reactivity are based on this limited conformer sampling, they are inevitably biased towards whatever reactions and energetics are pertain to the chosen model.

In cases where experimental data may not be available, chemical intuition is limited and truncated portions of a molecule may have unexpected effects on the system, or the choice of conformation may not be representative of the molecule in situ, the potential exists to create an unphysical model that does not reflect experiment when these approximations or assumptions are relied upon.

For example, in computational studies of transition metal catalyzed polyolefin polymerization reactions, truncation of the polymer chain to a CH_3 or C_3H_7 group has been a common approach used to model monomer insertion.[266] This assumption however may lead computational chemists to overlook the impact that polymer chain conformation can have on

the polymerization process. Through the use of MD simulations of polyolefin chains, as well as other polymer structures, and subsequent comparison of results to physical observations, such as surface and interfacial tension, it has been shown that some coiling of polymer chains in solution occurs.[267-270] If coiling can occur during polymerization then it could potentially lead to the chain conformation impacting how easily monomer insertion can occur, especially in the case of living chain polymerizations, where polyolefin remains coordinated to the catalyst throughout the reaction.

Despite this possibility, the use of truncated polymer chain models,[266,271-277] where minimal conformers exist for consideration, has led to computational studies either (1) ignoring conformational sampling entirely or (2) only modeling a few chemically intuitive conformers. For instance, when modeling ethylene insertion using a Ti-constrained geometry catalyst, **Figure IV.1a**, four conformers of the propyl chain have been used to model insertion.[278] Based on the conformations at the second insertion step, it can be anticipated that a larger number of conformers could exist for each subsequent insertion step. As the number of potential conformers grows, it could be envisioned complexes may exist where the conformer could impact the ease with which C_2H_4 insertion occurs, an example of potential conformers is shown in **Figure IV.1b**. Therefore, in order to create models that more accurately capture experimental conditions, conformational sampling in systems like polymerization reactions becomes important, otherwise, computational chemists could miss important Ti-alkyl intermediates from which insertion may occur or be impeded.

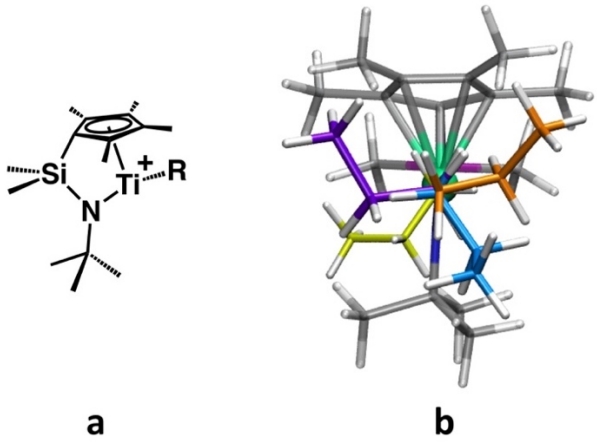

Figure IV.1: (a) Ti-constrained geometry catalyst for olefin polymerization. (b) Potential propyl chain ($Cp^*SiMe_2NC(CH_3)_3$)Ti-$C_3H_7^+$) conformers that could exist coordinated to Ti.

In general, systematic sampling of conformers is required to create models that are unbiased towards an arbitrary conformer choice and avoid inaccuracies that result from such models. Herein a new conformational sampling method that can be coupled with ZStruct[97] and SE-GSM[109] for automated reaction discovery from energetically stable intermediates is described, along with its application to understanding polymer chain conformation impact on Ti-catalyzed polyethylene generation.

From this work it becomes apparent that numerous local minima are likely to exist for systems containing flexible reactants. If reaction mechanisms are explored from the most stable local minima, it does not guarantee that the minimum energy pathway for a reaction will be found. More specifically for this polymerization reaction, conformational changes of the polymer chain do not change the general TS structure associated with the C_2H_4 insertion step, but they do impact the activation barrier through steric and electronic interactions with the catalyst. Finally, as the polymer chain length increases it becomes apparent that multiple points of interaction between the catalyst and polymer chain act together to impact the energetics to insertion. For example, differences in how close each respective polymer chain atom is to the Ti-center could have varying degrees of impact on initial structure stability or the barrier to insertion through steric interactions with the ligand backbone. The increased complexity of the system limits the ability to correlate a specific set of structural features the stability of initial and TS structures. However, with the Ti-$C_5H_{11}^+$ system, differences in Ti-$C_{polymer}$ distances are noted between

probable and unprobable initial and transition state (TS) structures that give some insight as to how polymer chain conformation impacts the energetics associated with polymerization.

Conformational Search Method

To address conformer generation with flexible catalysts or substrates, the CGen method outlined in **Figure IV.2** was developed using a combination of C++ and Python code. CGen generates metal-ligand or metal-substrate complexes with the ligand or substrate conformers generated by OpenBabel[117], providing insight into a variety of geometric structures that could exist within the transition metal complex. Ultimately, the generation and optimization of these conformers gives a means to sampling a variety of distinct reaction pathways using ZStruct[97] and SE-GSM.[109]

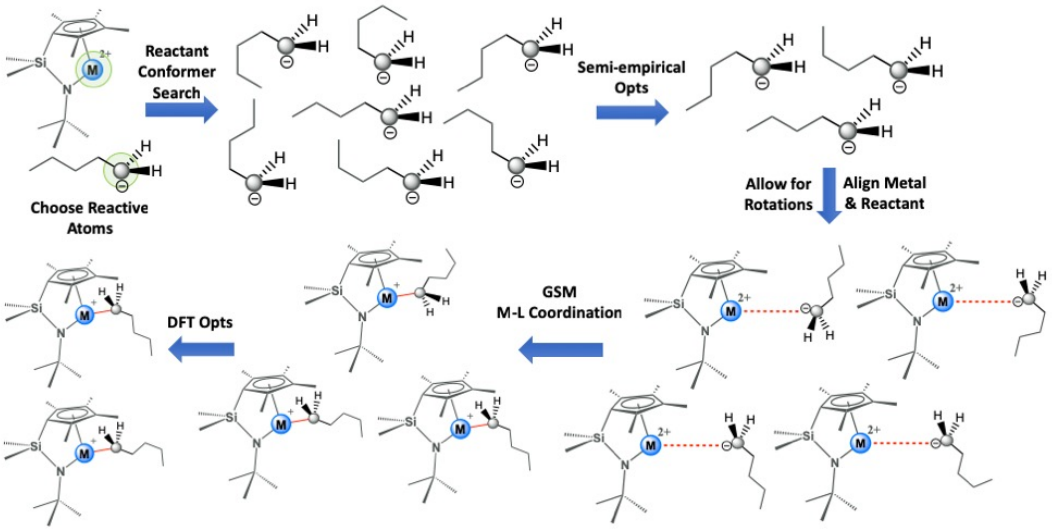

Figure IV.2: Flow chart for the generation, optimization and screening of conformer complexes using CGen, as applied to generating reactant complexes.

CGen (**Figure IV.2**) begins with two species, a fragment of the transition metal complex and the ligand/substrate that will be bound to the metal center. The ligation points/atoms on each structure (i.e. the metal of the metal center and the chelating atom of the ligand/substrate) are labeled for each of the input species. OpenBabel's confab method[117] is then applied to generate conformers of the ligand/substrate by rotating all of the flexible sigma bonds within the

molecule. From this exhaustive set of conformers, a Molecular Mechanics optimization is performed to refine the structures, followed by application of an energetic cutoff and root-mean square deviation (RMSD) metric to identify the unique, lowest energy structures. These conformers are then aligned with the target metal center, and SE-GSM is used to push the metal center and ligand/substrate towards one another until a low energy complex is generated. The complexes are then optimized using semi-empirical methods,[279-282] and another energy cutoff is applied to the resulting M-L structures to provide the initial set of low-energy conformers.

The lowest energy structures are then optimized using density functional theory (DFT) to garner accurate energetics. Similarly, a method for generating inorganic M-L complexes has been developed by Kulik and co-workers,[283] however their method does not take into account conformational searches of reactants. Therefore, with the use of this method, the impact of a reactants conformation on the number of potential low energy M-L complexes can be investigated, and subsequent reaction path exploration can be undertaken from relevant low energy structures.

This method was tested via application to polyolefin generation by Ti-Constrained Geometry Catalysts, **Figure IV.1**.[284-288] This catalyst has limited flexibility of backbone ligand, so the focus of this study will be to assess how the conformational flexibility of the polymer chain itself impact the intermediates and reaction pathways associated with ethylene monomer (C_2H_4) insertion and chain growth.

Computational Details

Investigation of Ti-catalyzed monomer insertion for ethylene polymerization was done using the CGen method, described above along with ZStruct[97] and SE-GSM[109]. The CGen method utilizes OpenBabel[117] to generate conformers of the initial molecular fragment. After conformer generation is completed, all initial geometries for intermediates and transition states were obtained using density functional theory (DFT) in the Q-Chem 4.3 quantum chemistry package.[289] Restricted B97-D[290-292] with a singlet spin and 6-31G* basis set[293,294] was used for optimization and frequency calculations. Energies for initial geometries, intermediates and transition states were refined by applying the 6-31+G* basis set,[295,296] and the SMD implicit solvent model, with

n-decane as the chosen solvent, [297-299] using the ORCA quantum chemistry package.[300] All energies listed are Gibbs free energies with enthalpy and entropy corrections in the solvent phase, and all geometries were confirmed to have the appropriate number of imaginary frequencies.

Thermodynamic corrections to the enthalpy, H, and gas phase entropy, $S_{(g)}$, at catalytic conditions (298 K, 1 atm) were computed for all structures. To avoid inaccuracies inherent in the harmonic oscillator approximation, corrections for enthalpies and entropies were calculated by replacing low frequencies (< 50 cm^{-1}) with 50 cm^{-1}. Solvent-phase enthalpies $H_{(s)}$ were derived by adding thermal corrections for the enthalpies to the corresponding solution-phase total energies ($E_{(l)}$). Considering the significant quenching of rotational and translational degrees of freedom in the solvent phase[301-304] entropies ($S_{(l)}$) were derived by scaling the gas-phase values $S_{(g)}$ by a factor of 0.5 to reduce the overestimation of entropies in the gas phase approximation. Energies reported for Ti-catalyzed monomer insertion are therefore solvent-phase Gibbs free energies ($G_{0.5T\Delta S(l)}$) at 1 atm and 298 K.

Constrained Geometry Catalysts in Polymerization Chemistry

Constrained geometry catalyst (CGC) systems were some of the first single-site catalysts to be commercialized for generating polyethylene.[284-288] Specifically, they have been used to manufacture polyethylene chains that contain long linear branches along the backbone. For this reason, these types of catalysts have been studied experimentally[284-288,305-315] and computationally [274-278,316-336] over the past few decades. The Cossee mechanism[337,338] (**Scheme IV.S1)** has been accepted as the mechanism for polymerization by homogeneous metallocene catalysts, such as the $Cp^*SiMe_2NC(CH_3)_3)Ti\text{-}R^+$ CGC catalyst (R = CH_3, C_3H_7, C_5H_{11}) studied herein.

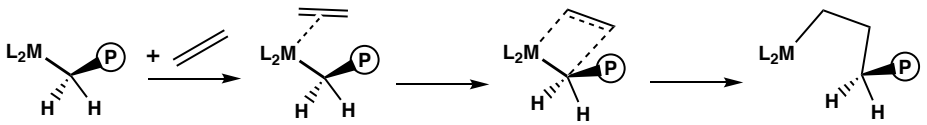

Scheme IV.S1: Cossee mechanism for ethylene polymerization.

Computational studies on similar catalyst systems (i.e. CGC catalysts with varying metal centers, or catalysts with bis-Cp ligands) have generally focused on modeling the first ethylene insertion step into a methyl group when investigating polymerization with the naked cation system (i.e. no counterion in the model). [276-278,330] While most of these studies therefore could safely exclude conformer searches, Ziegler and co-workers examined the energetics of rotation for the propyl chain product of the first insertion step using the Ti-CGC catalyst.[335] This study showed differences in energy between conformer rotations to be approximately 3 kcal/mol, suggesting that as chain elongation continues conformational changes are likely to occur, leading to numerous conformations existing in equilibrium with one another. More recent reports into this type of chemistry have used QM/MM methods to look at the first and second insertion steps for monomer insertion with CGC catalysts with the inclusion of a counterion (typically Me-$B(C_6F_5)_3^-$) in their model.[328,332] Selection of such conformers has previously been done manually, using chemical intuition.

In all studies of Ti-CGC catalyzed polymerization, polymer models up to 3 carbons—a propyl group—have been studied, without a systematic search for conformers. For this reason, conformational sampling at the second and third insertion steps using is done using CGen to help build an understanding of how chain flexibility impacts monomer insertion. Of specific interest are how the polymer chain conformation impacts the catalytic intermediates and transition state structures as well as the barriers to chain growth.

Results and Discussion

Starting from the CGC system, $Cp^*SiMe_2NC(CH_3)_3Ti\text{-}R^+$ catalyst shown in **Figure IV.1**, the procedure outlined in **Figure IV.3** was used to generate various conformations of the polymer chain and the Ti-polymer complexes from which chain growth was modeled. Each ethylene (C_2H_4) insertion step was modeled starting from the cationic CGC species (polymer = CH_3, C_3H_7, C_5H_{11} at each respective step). To assess the energetics of the C_2H_4 insertion step, reaction pathway searches were performed starting from the C_2H_4 monomer aligned with the open coordination site on the Ti-catalyst. Upon reaction path generation and TS optimization, qualitatively similar monomer insertion steps were found, all proceeding through the Cossee mechanism. [337,338] These

TS structures correspond to the C_2H_4 monomer being roughly inline with atom C_1 of the polymer chain (i.e. the carbon atom that is forming a bond with the incoming monomer), shown in **Figure IV.4**.

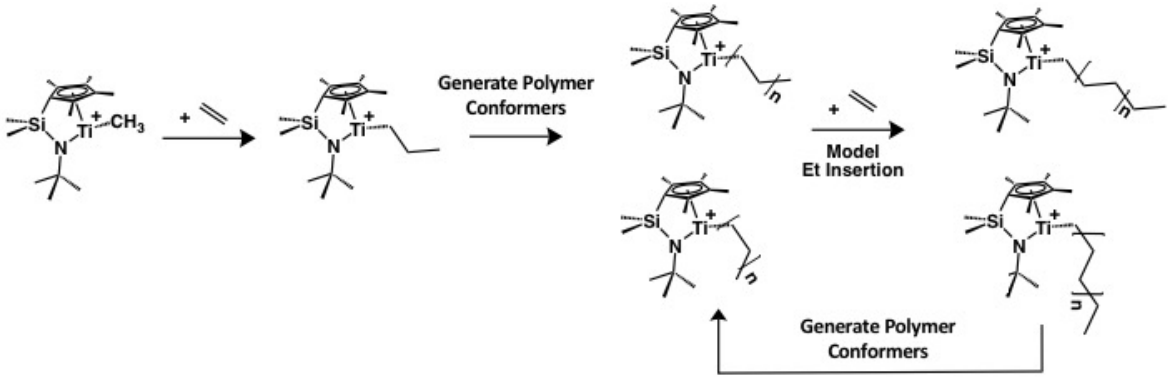

Figure IV.3: Flow chart for modeling ethylene insertion with multiple conformers as the polymer chain grows.

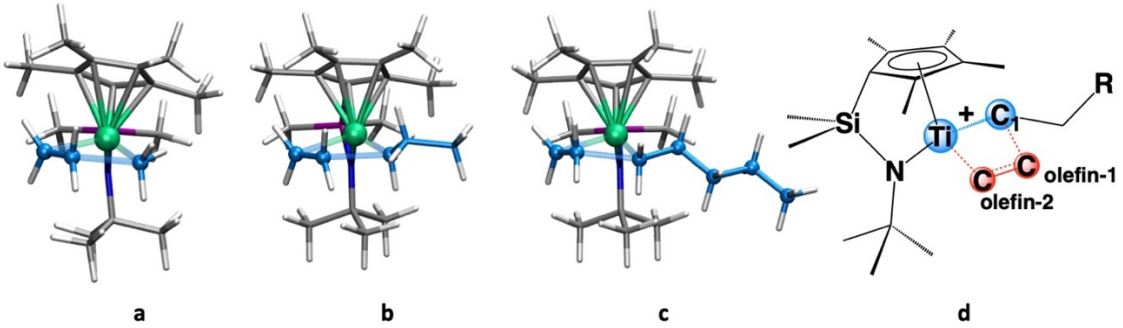

Figure IV.4: 3D rendering of example TS structures for the (a) first, (b) second and (c) third C_2H_4 insertion steps. (d) Chemdraw of C_2H_4 insertion TS with Ti, C_1, $C_{olefin\text{-}1}$, and $C_{olefin\text{-}2}$ labeled.

First Ethylene Insertion Step

The sole conformer of the $Cp^*SiMe_2NC(CH_3)_3Ti\text{-}CH_3^+$ species ($Ti\text{-}CH_3^+$) was modeled for the first insertion step, and the barrier for insertion through the Cossee 4-membered TS was 6.6 kcal/mol (relevant bond distances can be found in **Table 1**). After the transition state the propyl chain intermediate is formed and is downhill in energy by 12 kcal/mol. This calculated activation barrier reflects that of other theoretical studies into this cationic system, which report initial insertion barriers of roughly 6 kcal/mol.[278] These reports as well as the calculated barriers in this work do not match the experimentally determined insertion barrier of 13.3 kcal/mol.[308] The discrepancy in the barrier suggests that the truncated system alone does not accurately reflect

the true experimental conditions. The first insertion into the methyl group should encounter less resistance than when a longer polymer chain is present, so the second insertion step clearly requires examination to understand this discrepancy.

Table IV.1: Average values for relevant bond distances for monomer insertion TSs with Ti-CH_3^+, Ti-$C_3H_7^+$, and Ti-$C_5H_{11}^+$. All bonds are reported in Å, and angles reported in degrees

Conformer	Ti-C_{olefin} dist.	$C_{olefin1}$-$C_{olefin2}$ dist.	C_{olefin}-C_1 dist.	Ti-C_1 dist.
Ti-CH_3^+ ref 334	2.38	1.34	3.00	1.99
Ti-CH_3^+	2.22	1.42	2.16	2.15
Ti-$C_3H_7^+$ (Confs 1,2,3)	2.25	1.40	2.28	2.14
Ti-$C_3H_7^+$ (Conf 4)	2.19	1.43	2.10	2.30
Ti-$C_5H_{11}^+$	2.21	1.42	2.16	2.23

Second Ethylene Insertion Step

The second ethylene insertion step was modeled beginning with the cationic Ti-$C_3H_7^+$ catalyst species, where multiple conformers of the C_3H_7 polymer chain are present. The CGen method generated four different Ti-$C_3H_7^+$ species (**Figure IV.5**), similar to those studied in previously by Ziegler and co-workers[328,332] that could then be used to model the C_2H_4 insertion step**.**

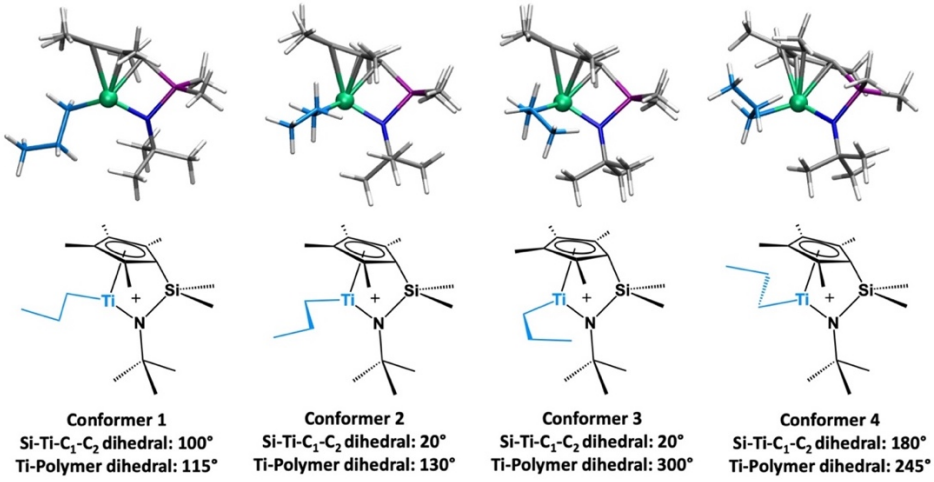

Figure IV.5: 3D rendering of the four Ti-$C_3H_7^+$ complexes generated using CGen. (Top) 3-D structures. (Bottom) 2-D renderings.

Each of the conformers were aligned with a C_2H_4 monomer in two different orientations, inline with the polymer chain and perpendicular to the polymer chain, resulting in eight

structures from which insertion could be modeled from. The different structures led to differences in energy ($\Delta G_{initial}$) ranging from 0.0 to 7.6 kcal/mol (**Figure IV.6**).

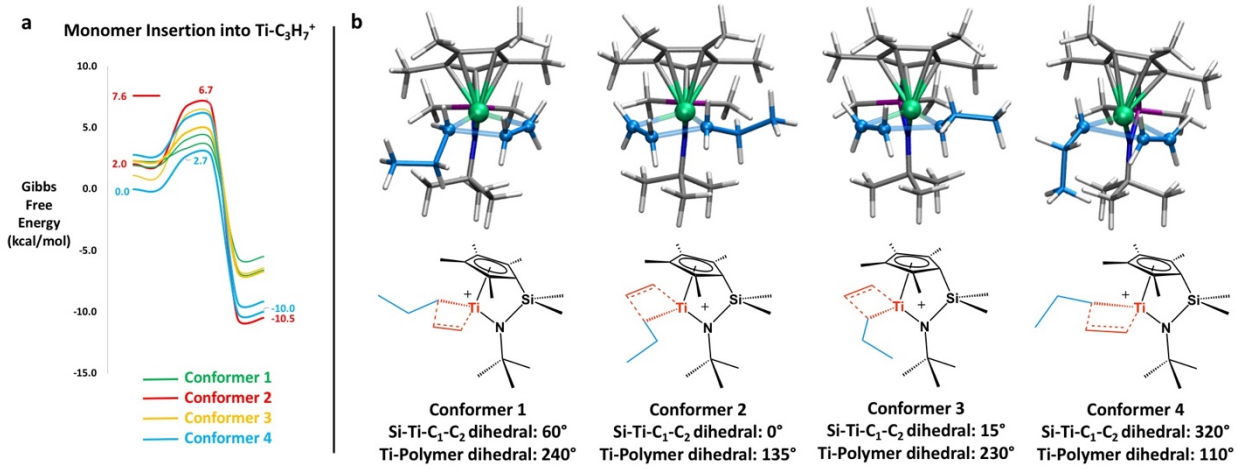

Figure IV.6: (a) Potential energy diagram for C_2H_4 insertion into Ti-$C_3H_7^+$. (b) 3-D renderings of TS structures (top) and 2D representations of TS structures (bottom) for each conformer of Ti-$C_3H_7^+$.

The initial structures appear to be stabilized by a decreased distance between the polymer chain and the Ti-center. Decreased distance likely allowed for more favorable η^2 coordination modes to exist, which are known to be energetically favorable based on previous theoretical studies.[334,339] However, during monomer insertion the polymer chain coordination mode changes from η^2 to η^1 in order for a C-C bond to form between the C_1 carbon and C_2H_4. To investigate the stability of an η^2 coordination with Ti-$C_3H_7^+$, and see how easily the coordination mode can change to allow for insertion to occur, the energetics of converting from an η^2 to η^1 coordination mode with the propyl chain was assessed, **Figure IV.7**, and found to be uphill by 1.8 kcal/mol. In the initial η^2 structure, **A**, the Ti-C_{olefin} distance is 2.67 Å and the Ti-C_1 and Ti-C_2 distances are 2.12 Å and 2.56 Å respectively, while the Ti-C_1-C_2 angle is 87.8 degrees. In contrast, the η^1 structure, **B**, has a Ti-C_{olefin} distance of 2.55 Å and Ti-C_1 and Ti-C_2 distances of 2.08 Å and 2.91 Å, with and increased Ti-C_1-C_2 angle of 106.4 degrees, indicating that closer coordination of the incoming monomer can disrupt the η^2 coordination mode leading the less favorable η^1 coordination mode in prior to insertion.

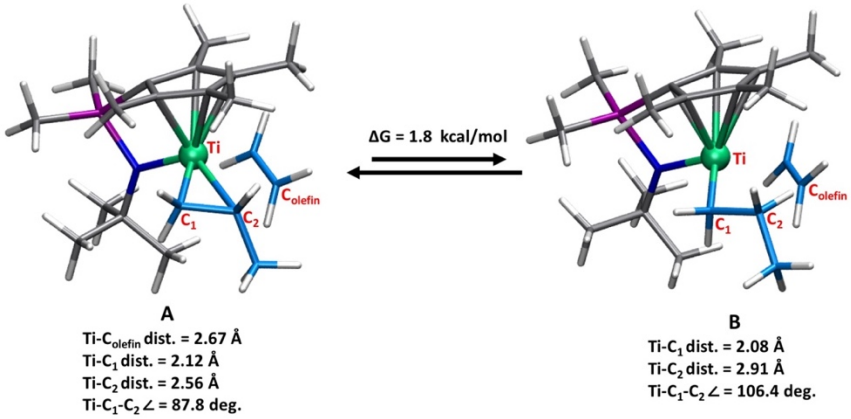

Figure IV.7 η^2 (A) versus η^1 (B) coordination modes of the Ti-$C_3H_7^+$ catalyst.

In contrast to the observed stabilizing effect of η^2 coordination, destabilization can occur when the distance between the Cp* ligand and the polymer chain decreases, likely due to steric clashing between the polymer chain and catalyst backbone. (More details of these interactions can be found in the *Appendix C.*)

From the initial Ti-$C_3H_7^+$ structures the reaction pathways for C_2H_4 insertion were modeled and each conformer led to a reaction path with a TS containing a 4-membered ring between the Ti, C_1 carbon, and both carbons of the C_2H_4 monomer. In a similar fashion to the first insertion step, the monomer addition occurred through an inline orientation of the incoming monomer and C_1 of the polymer chain (**Figure IV.6b**). The TSs are qualitatively similar to those noted in the first insertion step, relevant structural features can be found in **Table IV.1**. The relative energy for insertion amongst the TS structures found (ΔG_{TS}, referenced from the lowest energy initial structure) ranged from 2.7 to 6.7 kcal/mol(**Figure IV.6a**). The highest energy starting structure ($\Delta G_{Initial}$ = 7.6 kcal/mol) did not result in a successful reaction pathway due to a nonproductive orientation of the monomer, being perpendicular to the polymer chain. The same propyl conformation with the lower energy C_2H_4 monomer orientation (inline with the polymer chain) led to the highest energy reaction pathway with ΔG_{TS} = 6.7 kcal/mol. The high energy to insertion with this conformer is likely due to the presence of an η^2 coordination mode between the Ti-center and C_1 and C_2 of the propyl chain in the initial structure, and the H atoms of the C_1 carbon of the propyl chain being oriented towards the incoming monomer prior to insertion. The breaking of the η^2 coordination mode along with the required rotation of the C_1 atom for proper

alignment with the $C_{olefin\text{-}1}$ atom to allow for monomer insertion, likely causes the higher insertion barrier, see **Figure IV.6**, conformer 2.

The lowest barrier pathway found for the second monomer insertion was lower than that of the first insertion with a barrier of 2.7 kcal/mol compared to 6.6 kcal/mol, which is similar to what has been observed in previous computational studies. [328,332] Among the various conformers, the lowest barrier pathway (ΔG_{TS} = 2.7 kcal/mol) originated from the lowest energy initial structure, while the highest energy transition state (ΔG_{TS} = 6.7 kcal/mol) originated from a conformer with a moderate energy ($\Delta G_{Initial}$ = 2.0 kcal/mol). This indicates that the starting structure alone does not dictate the TS energy, and the activation barriers cannot be described only in terms of a ground state effect.

Third Ethylene Insertion Step

The third ethylene insertion step, which has not previously been computationally studied, led to the generation of 46 Ti-$C_5H_{11}^+$ conformers from which insertion may occur (**Figure IV.8**). These structures were aligned with a C_2H_4 monomer to generate initial structures with relative energies ($\Delta G_{Initial}$) ranging from 0.0 to 11.0 kcal/mol (**Figure IV.9**)**.** The energy difference between the initial structures could not be correlated to specific set of structural features, but there was some evidence that these energies depend on the Ti-C_4 and/or Ti-C_5 distances, details of which can be found in the *Appendix C.*

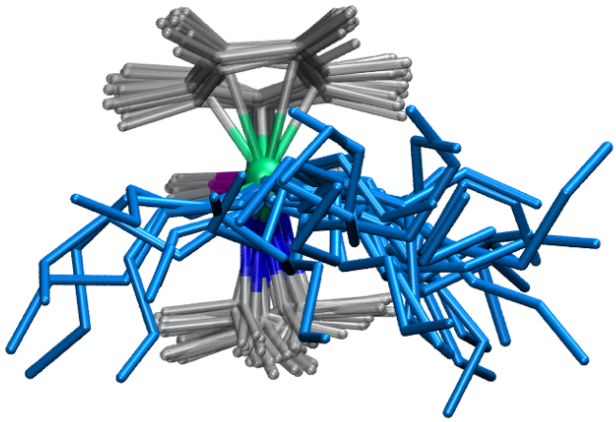

Figure IV.8: 3-D overlay of Ti-$C_5H_{11}^+$ structures produced by the CGen method and used for reaction exploration. Pentyl chains are shown in blue, and H atoms are omitted for clarity.

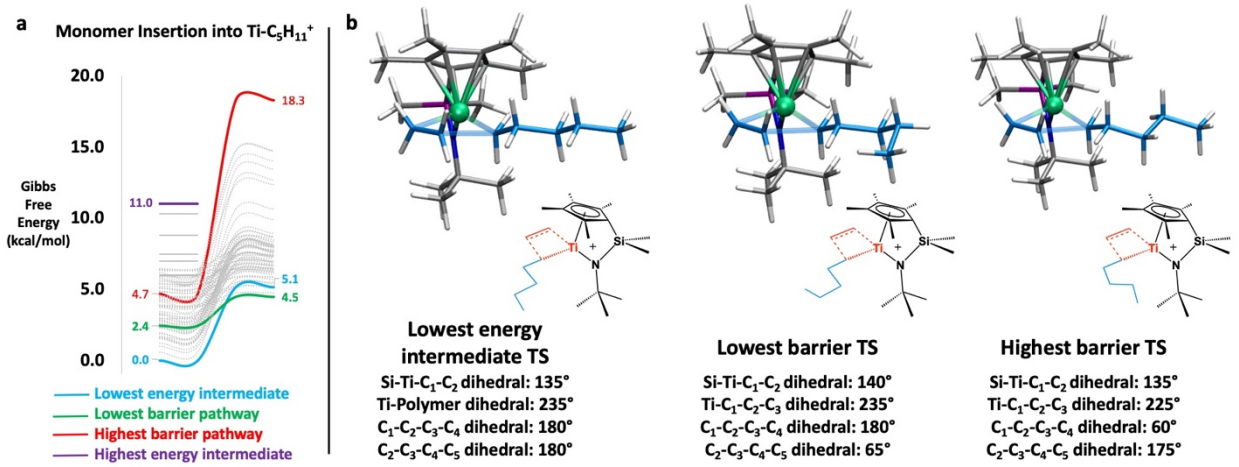

Figure IV.9: (a) Potential energy diagram showing the relative differences in energy between the initial and transition state structures for C_2H_4 insertion into Ti-$C_5H_{11}^+$. (b) 3-D renderings of TS structures and 2D representations of TS structures for the lowest and highest energy pathways.

From each of the initial Ti complexes, reaction paths for monomer insertion were modeled, and the structural features impacting the relative energies to insertion (ΔG_{TS}) were assessed. As was expected, each TS follows the Cossee mechanism and contains a 4-member TS structure that forms a C-C bond between the C_1 atom of the polymer chain and the carbon atom of C_{olefin} atom closest to it, as shown in **Figure IV.4**. Like previous insertion steps modeled, the TSs generally have an inline orientation where the incoming monomer is in the same plane as the C_1 atom of the polymer chain. The average Ti-C_1, C_1-$C_{olefin-1}$, $C_{olefin-1}$-$C_{olefin-2}$, and Ti-$C_{olefin-2}$ distances of 2.23 Å, 2.16 Å, 1.42 Å, and 2.21 Å at the TS are similar to the distances observed in the first and second insertion steps, a comparison of which can be found in **Table IV.1**. Although the transition states found are qualitatively similar, variations in their structures gave rise to ΔG_{TS} values ranging from 4.5 to 18.3 kcal/mol, with respect to the lowest energy starting structure (**Figure IV.9**).

As was the case with the Ti-$C_3H_7^+$ model the relative energy of the initial structures does not correlate directly to the relative energy of their respective TS structure. This is evident by the fact that the highest and lowest energy TSs do not result from the highest and lowest energy initial structures. In fact, the lowest energy starting structure leads to a reaction pathway with ΔG_{TS} of 5.1 kcal/mol. In contrast, the highest energy structure that leads to successful monomer

insertion ($\Delta G_{Initial}$ = 8.2 kcal/mol) leads to a reaction pathway with ΔG_{TS} of 8.5 kcal/mol. Additionally, the lowest barrier pathway (ΔG_{TS} = 4.5 kcal/mol) originates from an intermediate with a relative energy of 2.4 kcal/mol.

Structural analysis of both the Ti-$C_3H_7^+$ and Ti-$C_5H_{11}^+$ systems show that the Ti-Cp* interactions have some level of impact on the stability of the TS, and details of this interaction for the second and third step can be found in *Appendix C.* With the presence of a longer polymer chain, a wider range of ΔG_{TS} values were found across all of the reaction pathways for the third insertion step compared to the second insertion step. Additionally, as was observed with the Ti-$C_3H_7^+$ system, higher energy intermediates in the Ti-$C_5H_{11}^+$ system were not as successful in leading to successful monomer insertion pathways as their lower energy counterparts. The higher energy intermediates, however, are not expected contribute much to the total reaction mechanism, as they have a lower relative probability of existing in-situ. Based on the idea that some structures may be more probable than others, based on their relative energies, partition function were generated to determine the probability of the system existing as any of the conformers generated using **Equation 1**, where E_{conf} is the energy of each conformer and kT is the average thermal energy.

$$P_{conf} = \frac{e^{-\frac{1}{kT}E_{conf}}}{\sum_{conf} e^{-\frac{1}{kT}E_{conf}}} \qquad (1)$$

These probabilities are shown in **Figure IV.10**, where it is clear that P_{conf} is less than 1% if $\Delta G_{Initial}$ is above 2 kcal/mol. The three lowest energy structures have relative probabilities of 43.3%, 23.5%, and 5.4%.

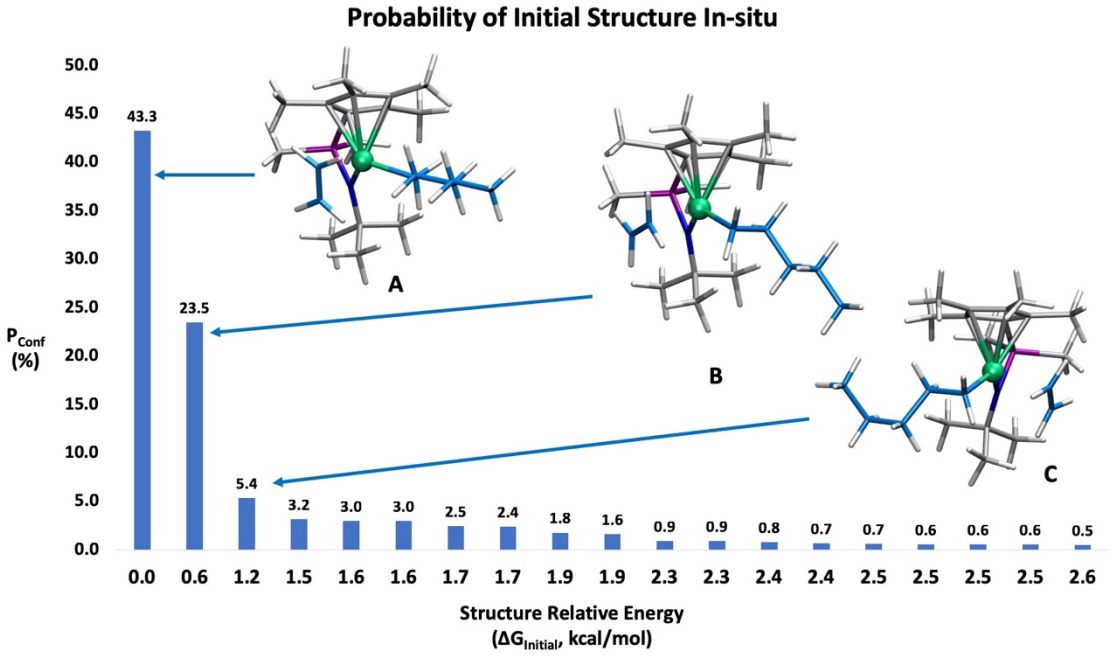

Figure IV.10: Partition function based relative probability of conformers existing in-situ based on their relative energies. Structures with probabilities below 0.5% were omitted from the chart. 3D structures for the three highest probability structures (A, B, and C) are shown.

Within the three lowest energy structures, the Ti-C_1 distance remains relatively unchanged, while the Ti-C_2 and Ti-C_3 distances don't appear to impact the stability of the conformer. In contrast, the Ti-C_4 and Ti-C_5 distances were lower for **structure A** (P_{conf} = 43.3%) and **structure B** (P_{conf} = 23.5%), while **structure C** (P_{conf} = 5.4%) had Ti-C_4 and Ti-C5 interactions similar to average of the other lower probability conformers, (**Table IV.2**). Specifically, the Ti-C_5 distance for **structures A** and **B** were 6.86 Å and 6.22 Å, respectively, which are 0.94 and 0.40 Å greater than the average Ti-C_5 distance amongst the lower probability conformers. Additionally, for **structures A** the Ti-C_4 distance is 5.47 Å, which is 0.55 Å greater than the average Ti-C_4 distance across the lower probability conformers. This suggests that maximizing the Ti distance from the terminal end of the polymer chain should be considered when trying to generate low energy initial Ti-polymer complexes. The farther distance of the terminal end of the polymer chain from the Ti center could be envisioned to allow for a less crowded open coordination site to be present for the incoming monomer to coordinate to prior to insertion occurring.

Table IV.2: Ti-polymer chain features for highest probability Ti-$C_5H_{11}^+$ initial structure conformers versus average across low probability conformers. All distances are in Å

Structure	P_{Conf} (%)	Ti-C_1	Ti-C_2	Ti-C_3	Ti-C_4	Ti-C_5
A	43.3	2.09	2.93	4.39	5.47	6.86
B	23.5	2.12	2.47	3.78	4.90	6.22
C	5.4	2.09	2.48	3.79	4.81	5.40
Avg. other conformers	< 5.0	2.09	2.94	4.01	4.92	5.82

The probability of insertion occurring through each of the 84 pathways to monomer insertion (two initial orientations of the monomer with each respective conformer) found for the Ti-$C_5H_{11}^+$ system were also calculated (**Figure IV.11**). From these pathways the three most probable TS structures leading to insertion with Ti-$C_5H_{11}^+$ occur in a 35:17:8 ratio, with ΔG_{TS} values of 4.5, 4.7 and 4.9 kcal/mol. Once ΔG_{TS} for insertion with this system rises above 6.1 kcal/mol the relative probability of insertion through that pathway drops below 1%.

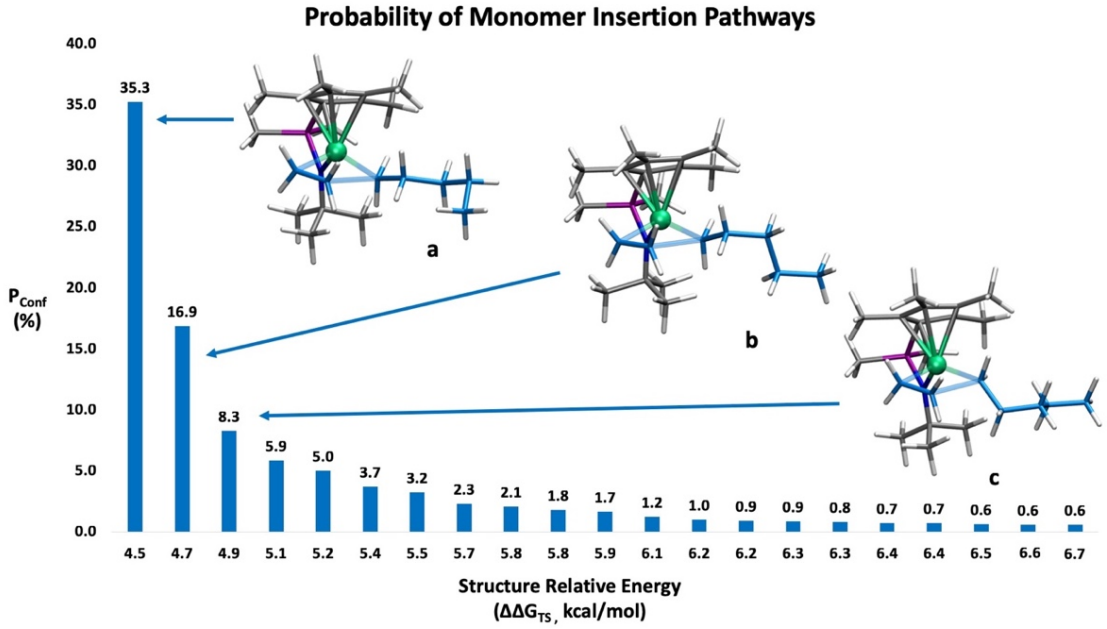

Figure IV.11: Partition function-based relative probabilities of monomer insertion occurring through the pathways found for Ti-$C_5H_{11}^+$ based on the relative energies of the TS structures. Pathways with relative probabilities below 0.5% were omitted from the chart. 3D structures for the three highest probability structures (a, b, and c) are shown.

When the three highest probability TS structures were compared to the other TS structures, it was found that certain Ti-$C_{polymer}$ distances vary significantly. Specifically, the top

three most probable TS structures (a, b, and c in **Figure IV.11)** have closer Ti-C_1 distances compared to the lower probability structures, which suggests pathways with earlier transition states are more favorable. This matches with Hammond's postulate which would suggest that the exothermic nature of insertion, shown in **Figure IV.6a** for the second insertion step, would lead to a TS structure more like the reactant than product. In addition to this structures a, b and c also have longer Ti-C_2, -C_3 and -C_5 distances compared to the average across the less probable TSs, implying that lower steric interactions between the polymer chain and Ti and catalyst leads to more favorable routes to insertion, bond distances can be found in **Table IV.3**.

Table IV.3: Ti-polymer chain features for highest probability Ti-$C_5H_{11}^+$ TS conformers versus average across low probability conformers. All distances are in Å

Structure	P_{conf} (%)	Ti-C_1	Ti-C_2	Ti-C_3	Ti-C_4	Ti-C_5
a	35.3	2.12	3.48	4.51	5.88	6.60
b	16.9	2.11	3.46	4.53	5.09	6.46
c	8.3	2.15	3.51	4.53	4.65	6.08
Avg. all other TSs	< 6%	2.24	2.86	4.06	5.07	5.99

Although the sampling of conformers clearly shows a wide range of free energies across these structures, overall this study did not lead to a minimum energy pathway with a calculated barrier close to the experimental barrier of 13.3 kcal/mol.[308] This suggests that modeling the reaction with a counterion, required experimentally, is needed to obtain more accurate energetics. In the next chapter the challenge of systematically modeling counterion interactions for this reaction is tackled.

Discussion

Modeling the ethylene insertion step for Ti-CH_3^+, Ti-C_3H7^+, and Ti-$C_5H_{11}^+$ complexes becomes more challenging as the number of potential conformers of the polymer chain increases as the chain length grows (1, 4, and 46 conformers for each respective system in this case, see **Table IV.4**). Each respective insertion step was found to occur through a 4-member TSs leading to C-C bond formation based on the Cossee Mechanism, that can be described in this work as a mid-reaction TS based on the average $C_{olefin\text{-}1}$-$C_{olefin\text{-}2}$ bond distance being 1.4-1.42 Å at the TS during each step of insertion, **Table IV.1**.

To assess how conformational changes impact the mechanism and energetics of monomer insertion, reaction pathways from all of the relevant conformers were searched for. From the resulting pathways it became evident that the atoms of the polymer chain that undergo conformational changes did not participate directly in the C-C bond forming step, therefore conformational changes had minimal impact on the mechanism of insertion. Despite this, conformational changes resulted in a wide range of ΔG_{TS} values found for both the second (ΔG_{TS} = 2.7 to 6.7 kcal/mol) and third (ΔG_{TS} = 4.5 to 18.3 kcal/mol) insertion steps, **Table IV.4**, due to variations in polymer chain-catalyst steric interactions. Although sampling here demonstrated that the mechanism was minimally affected by the choice of conformers, other reactions could be envisioned where the atoms involved in conformational changes directly impact the bond forming/breaking mechanism, making conformational sampling of TS structures even more important for generating a model that accurately depicts experimental conditions.

Table IV.4: Outcomes of modeling C_2H_4 insertion at Ti-CH_3^+, Ti-$C_3H_7^+$, and Ti-$C_5H_{11}^+$. All energies are in kcal/mol.

Chain Length	# Conformers	$\Delta G_{Initial}$ Range	Range $\Delta\Delta G_{TS}$
CH_3	1	N/A	6.6
C_3H_7	4	0.0 - 7.6	2.7 - 6.7
C_5H_{11} (all conformers)	46	0.0 - 11.0	4.5 - 18.3
Initial $C_5H_{11}^+$ (P_{conf} > 23%)	2	0.0 - 0.6	5.1 - 7.5
TS $C_5H_{11}^+$ (P_{conf} > 10%)	2	2.4 – 3.9	4.5 – 4.7

To further the understanding of how the polymer chain conformation impacted $\Delta G_{Initial}$ and ΔG_{TS} the probability of each initial structure and TS to insertion with the more complex polymer chain, Ti-$C_5H_{11}^+$ were looked at. Relative probabilities were calculated by generating a partition function for the total energy of the system and treating each conformer as a microstate. With this analysis, two initial structure conformers stuck out as being likely to exist with probabilities of 43.3% and 23.5%, while all other conformers had probabilities lower than 6%. These two structures had Ti-C_5 distances that were longer than in the lower probability complexes, and in the highest probability conformer the Ti-C_4 distance was also elongated in comparison to the other conformers. The increase in distance between Ti and the terminal end of the polymer chain leading to the lowest energy structure suggests minimizing steric

interactions between the polymer chain and catalyst should be done to generate minimum energy initial complexes by hand.

In a similar manner, the probability analysis revealed three favorable TS structures with relative probabilities of 35.3%, 16.9% and 8.3% When these structures were compared to the less probable TS structures it became evident that reducing steric interactions between Ti and the polymer chain atoms not coordinated to Ti is important to stabilize the TS structure. In contrast though, shorter Ti-C_1 distances were observed in the higher probability structures, which suggests that closer interaction between the Ti and the coordinating C_1 atom stabilizes the TS leading to monomer insertion.

Overall analysis of the most probable initial and TS structures demonstrated that the most likely routes to C-C bond formation occur through Ti-polymer conformations that reduce steric interactions between the polymer chain and catalyst by orienting the polymer chain so that the $C_{polymer}$ atoms, except for C_1, as farther removed from the Ti center.

More specifically though, it is observed that Ti-C_1, -C_2, and -C_3 distances in the initial structures generally don't change across all conformers, whereas with the TS closer Ti-C_1 distances and farther Ti-C_2, and -C_3 distances appear to lead to more stable complexes. When it comes to the C_4 and C_5 atoms though, greater distances between Ti and these atoms appears to stabilize both the TS and initial structures. This difference in what atoms lead to more stable structures implies that the most likely conformer initially is not the same as the most likely conformer that exists at the TS, signifying that conformational searches of intermediates and TS structures should be done when investigating reactions with flexible reactants.

Overall the insight gained with conformational sampling and subsequent reaction path exploration within this study led to the following insights about conformational sampling and Ti-CGC catalyzed polymerization reactions:

(I) The relative energies of starting structures ($\Delta G_{Initial}$) do not always correlate to the relative energy differences amongst each pathways respective TS structures (ΔG_{TS}).

(II) Polymer chain conformational changes do not significantly impact the qualitative TS structure for C_2H_4 insertion. Avg. Ti-C_{olefin}, $C_{olefin-1}$-$C_{olefin-2}$, C_1-$C_{olefin-1}$ and Ti-C_1 distances and geometries remain similar across all insertion steps (**Table IV.1**).

(III) As the polymer chain becomes more complex, no unique polymer chain structural feature(s) has a direct impact on a structure's energy (i.e. multiple features can act together to stabilize or destabilize a structure).

(IV) The initial structures of longer polymer chain systems are stabilized by further distances between the terminal carbon atoms (C_4 and C_5) of the polymer chain.

(V) Transition state structures to monomer insertion with a longer polymer chain are stabilized by:

i. Decreased Ti-C_1 distances

ii. Increased Ti-C_2, -C_3, -C_4, and -C_5 distances

(VI) Considering larger polymer chain lengths alone does not create a model that reflects the experimental activation barriers of 13.3 kcal/mol.[308]

Conclusions

The conformational sampling tools described in this chapter were able to explore polymerization beyond the realm of previous computational studies and look at how polymer chain conformation can impact the barrier to monomer insertion. This study was able to look at 46 conformers of the elongated $C_5H_{11}^+$ polymer chain and their pathways to insertion with two different monomer orientations with minimal user input, a feat that would not be possible without the CGen method and SE-GSM.

This study therefore was able to delve deeper into assessing how polymer chain conformation impacts the energetics and mechanism of monomer insertion. From the sampling obtained with CGen, direct correlation between the polymer chain orientation and the barrier to insertion was not found. However, it was found that as a polymer chain grows, the terminal atoms (C_4 and C_5) begin to have some impact on the stability of initial structure, and overall the distances between all of the polymer chain carbon atoms and Ti-center impacts the stability of the TS structure.

Lastly, this study demonstrated that the application of a partition function for narrowing which conformers are most probable to exist both prior to and during monomer insertion should be a sufficient way to screen structures to identify which conformers are chemically relevant. Even with increased polymer chain length and expansive conformational search, reaction barriers that were lower than the experimentally calculated barrier of 13.3 kcal/mol[308] were found for each insertion step modeled.

This discrepancy and the literature reports of counterion importance in modeling this reaction[326,328,332,333] led to expanding the search of chemical space to include the consideration of two different counterions (Me-$B(C_6F_5)_3^-$ and $B(C_6F_5)_4^-$) that are known to lead to different rates of polymerization in the next chapter.

CHAPTER V

Exploring Interactions between Counterions and Polymer Chains during Polyolefin Growth

Abstract

A wide variety of synthetic and catalytic reactions, including ethylene polymerization using Ti-constrained geometry catalysts (Ti-CGC), rely on additional reagents in the form of counterions to drive forward reactivity. Computational studies of these reactions tend to neglect modeling relevant catalyst-counterion complexes, unless it is obvious that a feasible reaction mechanism will not be found without them. With the use of the conformational search and reagent alignment method, CGen, modeling of how important borane counterions ($Me\text{-}B(C_6F_5)_3^-$ and $B(C_6F_5)_4^-$) interact with not only the Ti center, but also the flexible polymer chain was performed. Monomer insertion was modeled using the Ti-CGC catalyst $Cp^*SiMe_2NC(CH_3)_3)Ti\text{-}R^+$ ($R=CH_3$ or $C_3H_7^+$) with four different alignments of the respective counterion: (1) in front of the Ti center, (2) next to the C_2H_4 monomer coordinated to Ti, (3) next to the alkyl group coordinated to Ti and (4) above the Cp* ligand of the catalyst backbone. From this sampling it was found that the polymer chain repels the counterion from the Ti center as it grows. At the TS though, the counterion prefers to position itself as close to the Ti center as possible in the lowest barrier pathways. However, it was also found that certain counterion-catalyst alignments impede monomer insertion from occurring. Lastly, prior to monomer insertion the greater energetic cost of monomer uptake with $Me\text{-}B(C_6F_5)_3^-$ compared to $B(C_6F_5)_4^-$ raises the overall barrier to monomer insertion between the two counterions. This observation helps to explain differences in rates of polymerization observed experimentally with each counterion.

Introduction

Chemical reactions require reagents to act as co-catalysts, stabilizing agents, and as buffers to maintain consistent control over the reaction conditions. While typically thought to be the less important components of a reaction, reagents can be anything from explicit solvent molecules, to salts, acids, bases, and counterions, and they are absolutely vital for reactions to work. Strangely, the role of reagents is often ignored in computational studies, except in cases where it is plainly necessary in forming a plausible reaction mechanism. [104,105,107,108,110,328,332] With modern simulation tools, however, modeling multiple interacting chemical species using density functional theory (DFT) has become feasible, leaving less impetus to ignore reagents while studying reaction mechanisms. The role of reagents therefore can be studied in detail and should be done whenever there is experimental evidence or intuition that suggests the reagents may interact with rate-determining steps of a reaction profile.

The constrained geometry Ti catalyst for polyolefin growth explored in the previous chapter requires a borane co-catalyst to initiate polymerization.[284-288,308,309] The borane counterion is used for catalyst activation and remains present throughout the reaction[316-326], such that altering the counterion can lead to changes in the rate of reaction. [309-315] Computational studies have indicated that counterions that are strong nucleophiles have the potential to coordinate to open site on metal centers in similar Zr and Ti catalysts (with bis-Cp and CGC ligands). [318,319] These studies have also indicated that the lowering the charge on the metal center through counterion interactions or changes to the ligand structure can enhance catalyst activity.[330] A majority of these studies have focused on the Me-B$(C_6F_5)_3^-$ counterion,[330,331,335,336] but one study by Laikov and co-workers compared Me-B$(C_6F_5)_3^-$ and B$(C_6F_5)_4^-$ counterions, and found that weaker nucleophiles acted to enhance the rate of propagation.[326] However, this study was done using a bis-Cp ligated Zr complex, and only one insertion step beginning from the Zr-$C_2H_5^+$ cation was explored.[326] Ziegler and co-workers on the other hand, have examined the first two steps of monomer insertion for a Ti-CGC catalyst with the Me-B$(C_6F_5)_3^-$ counterion,[335,336] studying in particular two propyl chain conformers and two orientations of the counterion, *cis* and *trans* to the incoming monomer. The study found that rotation of the propyl chain can occur with a maximum barrier of 7 kcal/mol. Additionally, it was noted that Me-B$(C_6F_5)_3^-$ preferred to

be oriented *cis* to the incoming monomer relative to the Ti center during insertion. Although the work gave insight specifically into how Me-$B(C_6F_5)_3^-$ impacts the energetics of insertion, no other counterions were investigated nor was there an in depth investigation of how the propyl chain and counterion interact, if at all, during insertion outside of the preferred alignment of the counterion.[335,336]

To further improve the understanding of how borane counterions impact polymerization reaction, the CGen method was applied to the full catalyst system to generate ion-pairs between Ti-CGC and Me-$B(C_6F_5)_3^-$ as well as Ti-CGC and $B(C_6F_5)_4^-$. Compared to prior studies, this work systematically examines the second insertion step with a greater number of propyl chain conformers and multiple orientations of counterion coordination. By modeling both counterions more insight can be gained into the specific chemical effects of these additives, and compare how their impact on monomer uptake and insertion remains the same and/or differs. The study reveals that the difference in coordination strength between the two counterions impacts how energetically challenging monomer uptake prior to insertion is. Additionally, the comparison demonstrates that the most likely coordination mode for both counterions with respect to the Ti-center changes as the polymer chain length increases, and that the counterion can inhibit monomer insertion by blocking the polymer chain's ability to move and rotate during monomer insertion. Despite the counterion's apparent interference prior to monomer insertion, the 4-member TS structure though which insertion occurs was found to be minimally impacted by the presence of the counterion.

Computational Details

Investigation of Ti-catalyzed monomer insertion for ethylene polymerization was done using the CGen method, described above along with ZStruct[97] and SE-GSM[109]. The CGen method utilizes OpenBabel[117] to generate conformers of the initial molecular fragment. After conformer generation is completed, all initial geometries for intermediates and transition states were obtained using density functional theory (DFT) in the Q-Chem 4.3 quantum chemistry package.[289] Restricted B97-D[290-292] with a singlet spin and 6-31G* basis set[293,294] was used for optimization and frequency calculations. Energies for initial geometries, intermediates and transition states

were refined by applying the 6-31+G* basis set[295,296], and the SMD implicit solvent model, with n-decane as the chosen solvent,[297-299] using the ORCA quantum chemistry package.[300] All energies listed are Gibbs free energies with enthalpy and entropy corrections in the solvent phase, and all geometries were confirmed to have the appropriate number of imaginary frequencies.

Thermodynamic corrections to the enthalpy, H, and gas phase entropy, $S_{(g)}$, at catalytic conditions (298 K, 1 atm) were computed for all structures. To avoid inaccuracies inherent in the harmonic oscillator approximation, corrections for enthalpies and entropies were calculated by replacing low frequencies (< 50 cm^{-1}) with 50 cm^{-1}. Solvent-phase enthalpies $H_{(s)}$ were derived by adding thermal corrections for the enthalpies to the corresponding solution-phase total energies ($E_{(l)}$). Considering the significant quenching of rotational and translational degrees of freedom in the solvent phase[301-304] entropies ($S_{(l)}$) were derived by scaling the gas-phase values $S_{(g)}$ by a factor of 0.5 to reduce the overestimation of entropies in the gas phase approximation. Energies reported for Ti-catalyzed monomer insertion are therefore solvent-phase Gibbs free energies ($G_{0.5T\Delta S(l)}$) at 1 atm and 298 K.

Ethylene Polymerization with a Counterion

To model ethylene polymerization with the inclusion of a counterion monomer uptake involving: (1) Counterion coordination in the absence of C_2H_4 and (2) C_2H_4 coordination prior to monomer insertion, where C_2H_4 coordinates to Ti by displacing the counterion, were evaluated in addition to the monomer insertion step leading to chain elongation, **Figure V.1**. Specifically, thermodynamics were calculated for the intermediates involved in monomer uptake, while kinetic barriers to monomer insertion were calculated. All of the energies for the first and second polymerization steps were compared for both Me-$B(C_6F_5)_3^-$ and $B(C_6F_5)_4^-$ to investigate the cause for differences in rates of reaction between the two counterions. Additionally, various alignments (discussed below) of the counterion with respect to Ti were generated post monomer uptake and used to model monomer insertion. Similarly, multiple conformers of the Ti-$C_3H_7^+$ complex were modeled during the monomer uptake and insertion steps.

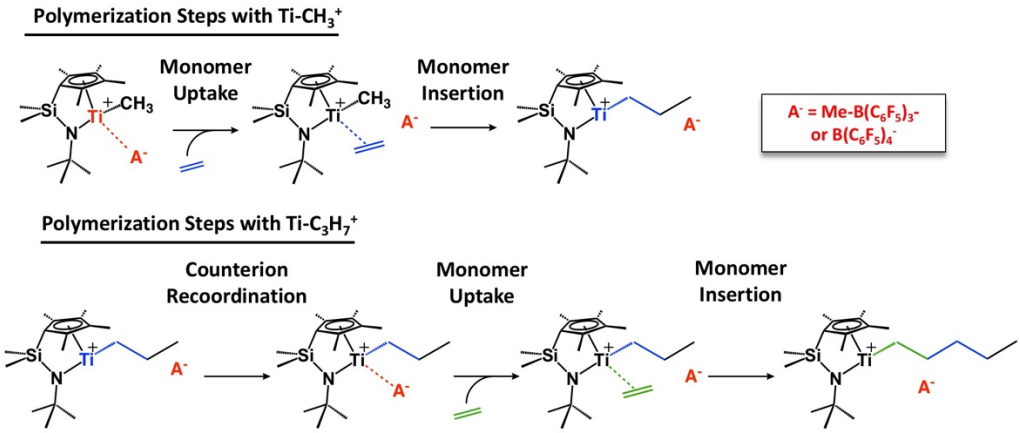

Figure V.1: Steps of polymerization considered within this work.

Monomer Uptake: Ti-CH_3^+

After methyl abstraction occurs to generate the active Ti-CH_3^+ catalyst, both counterions have the ability to coordinate to the open site on Ti, and the thermodynamics of this coordination versus C_2H_4 coordination to the open site was evaluated. In the case of the Me-$B(C_6F_5)_3^-$ counterion, the methyl group can form a bridging Ti-Me-B species with the open site on Ti when no monomer in present, whereas with $B(C_6F_5)_4^-$ no Me group is present to form a bridging species, **Figure V.2.** In these structures the Ti-B distance is 3.92 Å and 5.30 Å respectively for each counterion, indicating stronger coordination of Me-$B(C_6F_5)_3^-$ to Ti than $B(C_6F_5)_4$. In the case of Me-$B(C_6F_5)_3^-$ the methyl abstraction by the counterion and formation of the subsequent Ti-Me-B intermediate is characterized by Ti-Me and B-Me distances of 2.25 Å and 1.67 Å respectively. With both counterions, the coordinated structures are thermodynamically stable compared to the monomer coordinated intermediates, **Figure V.3**.

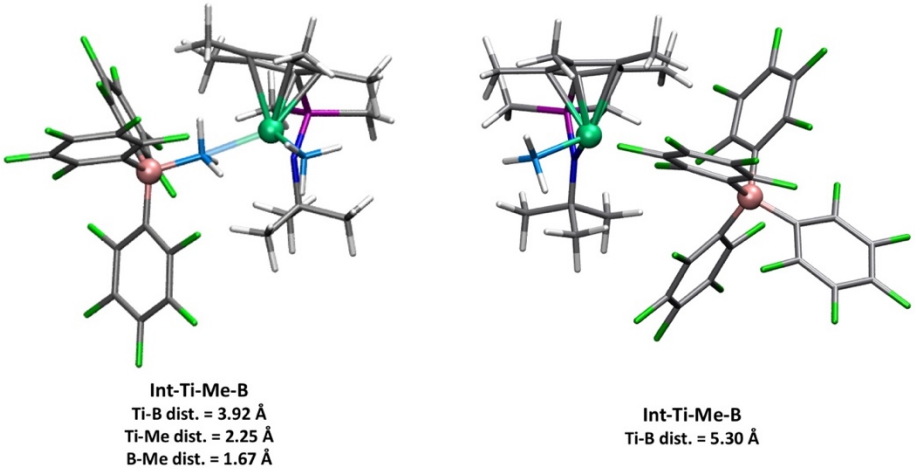

Figure V.2: 3-D renderings of Int-Ti-Me-B versus Int-Ti-B with key bond distances noted in Å.

With **Int-Ti-Me-B** monomer insertion leads uphill by 11.4 kcal/mol to reach a Ti-C_2H_4 coordinated structure with the counterion pushed away from the open site so that it is aligned in front of the Ti center, **Figure V.3**. In comparison coordination of the $B(C_6F_5)_4^-$ counterion, which a weaker nucleophile and does not coordinate as strongly to Ti, leads to monomer insertion being uphill by 3.3 kcal/mol to reach a similar Ti-C_2H_4 coordinated structure with the counterion pushed away from the open site, where it can then align itself in front of the Ti center, **Figure V.3.** After counterion displacement, the alignment of each counterion with respect to Ti was modeled in four different orientations (in front of Ti, next to the polymer chain, next to the C_2H_4 monomer and above the Cp* ligand). These alignments are discussed in more detail below, but overall lead to higher energy C_2H_4 coordinated structures indicated by the additional intermediate lines in **Figure V.3**.

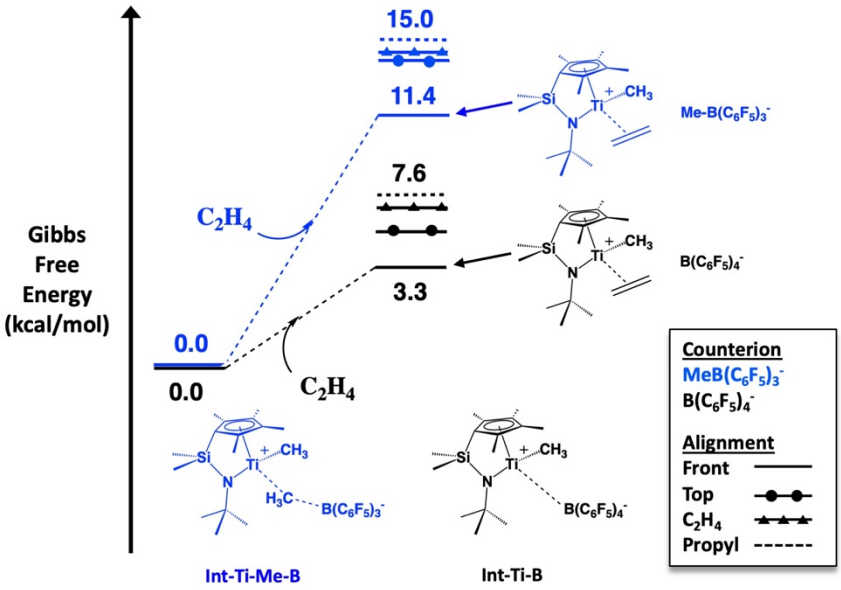

Figure V.3: Energetics of monomer uptake. (blue) Me-$B(C_6F_5)_3^-$ versus (black) $B(C_6F_5)_4^-$. The lowest energy Ti-C_2H_4 intermediates have the counterion aligned in front of the Ti center.

Monomer Uptake: Ti-$C_3H_7^+$

After the first monomer insertion step occurs and a propyl chain is formed, the open coordination site on Ti is reformed giving the counterion the ability to recoordinate to the metal center. Therefore, the thermodynamics of monomer uptake prior to the second insertion step were also calculated with respect to each of the four propyl chain conformers noted in **Chapter IV**. In the case of Me-$B(C_6F_5)_3^-$ the counterion can reform a Ti-Me-B bridging species with the catalyst prior to monomer uptake. This bridging species can form with all four propyl chain conformers, each of which mirrors the structure of **Int-Ti-Me-B**. These intermediates have relative energies of -13.2, -13.0, -10.9, and -9.4 kcal/mol for conformers 1, 2, 3, and 4 relative to **Int-Ti-Me-B**. From the lowest energy intermediate, **Int-Ti-Me-B-2,** which has the propyl chain oriented in conformer 1**,** monomer uptake is uphill by 10.3 kcal/mol, leading to a Ti-C_2H_4 coordinated structure. The lowest energy Ti-$C_3H_7^+$ complex with C_2H_4 coordinated to it has the polymer chain in conformation 2 and the counterion aligned above the Cp ligand, **Figure V.4a**. In comparison, the $B(C_6F_5)_4^-$ counterion leads to an initial Ti-$C_3H_7^+$-$B(C_6F_5)_4^-$ ion pair with each polymer chain conformer that are downhill in energy from **Int-Ti-B** by -7.4, -13.3, -9.8, and -13.1 kcal/mol for conformers 1, 2, 3, and 4 respectively. From the lowest energy intermediate, **Int-Ti-**

B-2, which has the propyl chain oriented in 3, monomer uptake is uphill by 3.9 kcal/mol, leading to a Ti-C_2H_4 coordinated intermediate. In this case the lowest energy Ti-$C_3H_7^+$ complex with C_2H_4 coordinated to it has the polymer chain in conformation 4 and the counterion aligned in front of the Ti center, **Figure V.4b**. As noted above, once the counterion is displaced by C_2H_4, the alignment of the counterion with respect to Ti was modeled with four different orientations of the counterion (in front of Ti, next to the polymer chain, next to the C_2H_4 monomer and above the Cp* ligand) with each propyl chain, which are discussed in more detail below, and were found to lead to higher energy C_2H_4 coordinated structures indicated by the additional intermediate lines in **Figure V.4a and V.4b**.

In both the first and second monomer uptake steps, the Me-$B(C_6F_5)_3^-$ counterion is able to form a stable Me-bridging species between Ti and boron. The need to disrupt the Ti-Me-B interactions ultimately raises the energy required for a monomer displace the counterion and coordinate to Ti. The lack of a Ti-Me-B interaction with $B(C_6F_5)_4^-$ leads to displacement of the counterion by C_2H_4 being a less energetically demanding step. This difference in coordination strength between the two counterions likely leads to differences in reactivity noted experimentally between the two counterions.[309]

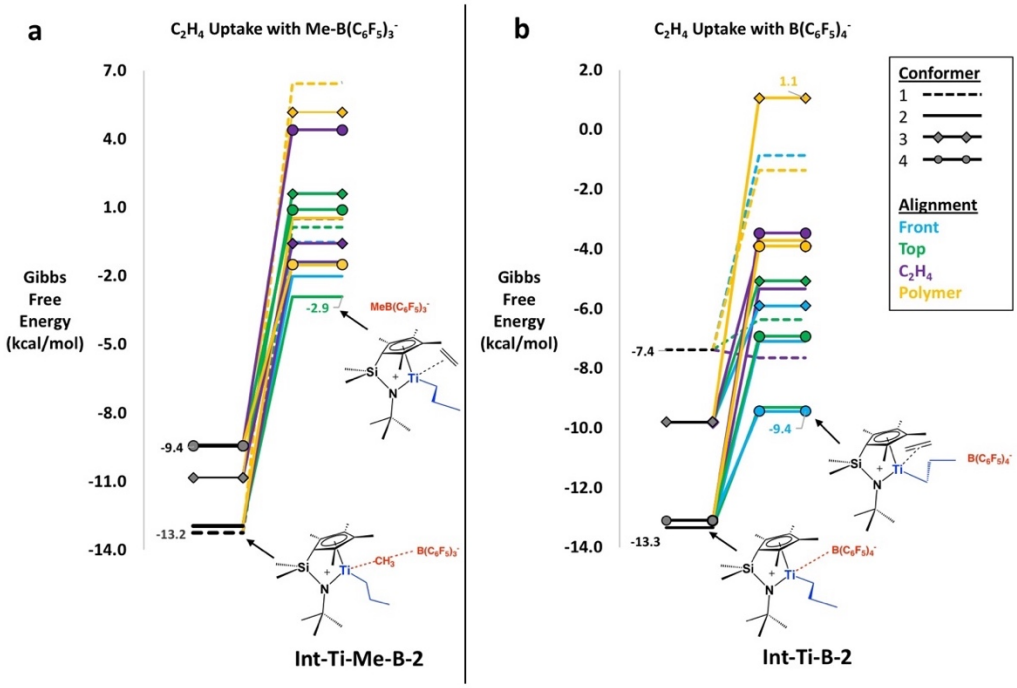

Figure V.4: Energetics of monomer uptake with Ti-$C_3H_7^+$ with (a) Me-$B(C_6F_5)_3^-$, (b) $B(C_6F_5)_4^-$

Counterion-Catalyst Alignment

As mention above, various counterion-Ti CGC alignments were generated to model monomer insertion from with both Me-$B(C_6F_5)_3^-$ and $B(C_6F_5)_4^-$. The sampling of alignments led to the following four orientations of the counterion with respect to the Ti catalyst: (1) above the Cp* ligand, (2) on the same side of Ti as the incoming C_2H_4 monomer, (3) on the same side of Ti as the alkyl chain and (4) in front of the catalyst, directly facing the position between the monomer and alkyl chain. This process was repeated for both counterions interacting with both the single conformer of Ti-CH_3 and the four conformers of Ti-$C_3H_7^+$ noted in **Chapter IV**. (An example of alignments with Ti-CH_3^+ and Me-$B(C_6F_5)_3^-$ is shown in **Figure V.5**)

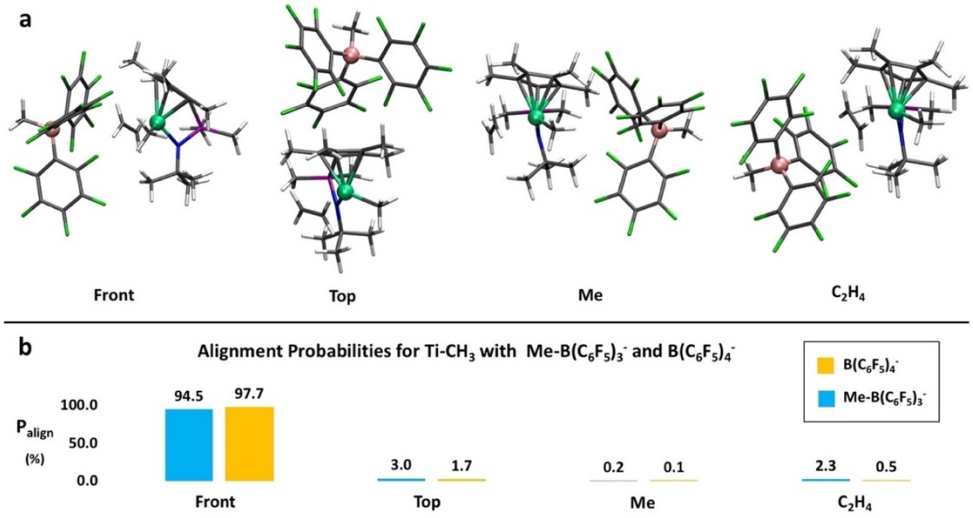

Figure V.5: (a) Alignment of Me-$B(C_6F_5)_3^-$ with the Ti-CH_3^+ catalyst and general energetic trends. (b) Partition function-based probability of each alignment with Me-$B(C_6F_5)_3^-$ (orange) and $B(C_6F_5)_4^-$ (blue).

With the Ti-CH_3 complex aligned with Me-$B(C_6F_5)_3^-$ the various alignments have energies ($\Delta G_{Initial}$) ranging from 11.4 to 15.6 kcal/mol (**Figure V.6**) when referenced to **Int-Ti-Me-B**, where the front aligned structure is lowest in energy. Similarly, when the counterion is swapped out to $B(C_6F_5)_4^-$ the same four alignments were found to have energies ($\Delta G_{Initial}$) ranging from 3.3 to 7.6 kcal/mol (**Figure V.6**), when referenced to **Int-Ti-B,** where the front aligned structure is also lowest in energy. If each alignment is treated as a microstate then the relative probability of each alignment (P_{align}) can be calculated based on the partition function of the total energy of the

system, Equation 1. This analysis shows that the front aligned structures are the most likely to exist with probabilities of 94.5% and 97.7% for Me-B(C_6F_5)$_3^-$ and B(C_6F_5)$_4^-$ respectively (**Figure V.5b**)

.

$$P_{align} = \frac{e^{-\frac{1}{kT}E_{align}}}{\sum_{conf} e^{-\frac{1}{kT}E_{align}}} \qquad (1)$$

Alignment in front of Ti allows for the Ti-B distance to be minimized at 6.08 Å and 5.85 Å for each counterion. With this alignment of Me-B(C_6F_5)$_3^-$ the counterion sits closer to C_2H_4 than CH_3 with a B-C_2H_4 distance 4.57 Å compared to the B-CH_3 distance of 5.63 Å. In contrast, B(C_6F_5)$_4^-$ sits closer to the Me group instead of C_2H_4 with B-C_2H_4 and B-Me distances of 5.39 and 4.68 Å. The farther distance from C_2H_4 observed with B(C_6F_5)$_4^-$ likely aids in allowing for insertion to occur, as opposed to Me-B(C_6F_5)$_3^-$ where the closer proximity to C_2H_4 leads to the failure to find a pathway to insertion (*vide infra*). In comparison the other alignments with Me-B(C_6F_5)$_3^-$ and B(C_6F_5)$_4^-$ have Ti-B distances ranging from 7.00 to 7.43 Å and 7.47 to 7.87 Å, respectively, which have higher ion-pairing energies. The least probable alignment was in line with the Me group on Ti (P_{align} < 0.5%) for both counterions, which is likely due to steric interactions destabilizing the complex. See **Tables V.1** and **V.2** for Ti-B distances relative to each alignment.

Table V.1: Relevant bond distances and energies for Me-B(C_6F_5)3$^-$-Ti ion pairs. All energies are in kcal/mol and all distances are in Å.

			Initial Structure			Transition State		
	$\Delta G_{Initial}$	**ΔG_{TS}**	**B-Ti dist.**	**B-C_2H_4 dist.**	**B-Me dist.**	**B-Ti dist.**	**B-C_2H_4 dist.**	**B-Me dist.**
Front	11.4	-	6.08	4.57	5.63	-	-	-
Top	13.4	21.4	7.43	8.90	8.78	7.22	8.69	8.82
CH3	15.0	18.8	7.40	9.59	7.32	6.70	8.35	6.13
C2H4	13.6	21.6	6.85	5.32	8.31	6.84	5.37	7.90

Table V.2: Relevant bond distances and energies for B(C_6F_5)$_4^-$-Ti ion pairs. All energies are in kcal/mol and all distances are in Å.

			Initial Structure			Transition State		
	$\Delta G_{Initial}$	**ΔG_{TS}**	**B-Ti dist.**	**B-C_2H_4 dist.**	**B-Me dist.**	**B-Ti dist.**	**B-C_2H_4 dist.**	**B-Me dist.**
Front	3.3	10.4	5.85	5.39	4.68	6.65	5.37	4.67

Top	5.7	10.5	7.49	7.89	8.67	7.19	8.58	8.59
CH3	7.6	12.3	7.47	9.75	7.20	7.35	9.25	7.32
C2H4	6.5	15.3	7.87	6.50	8.91	7.72	6.99	8.71

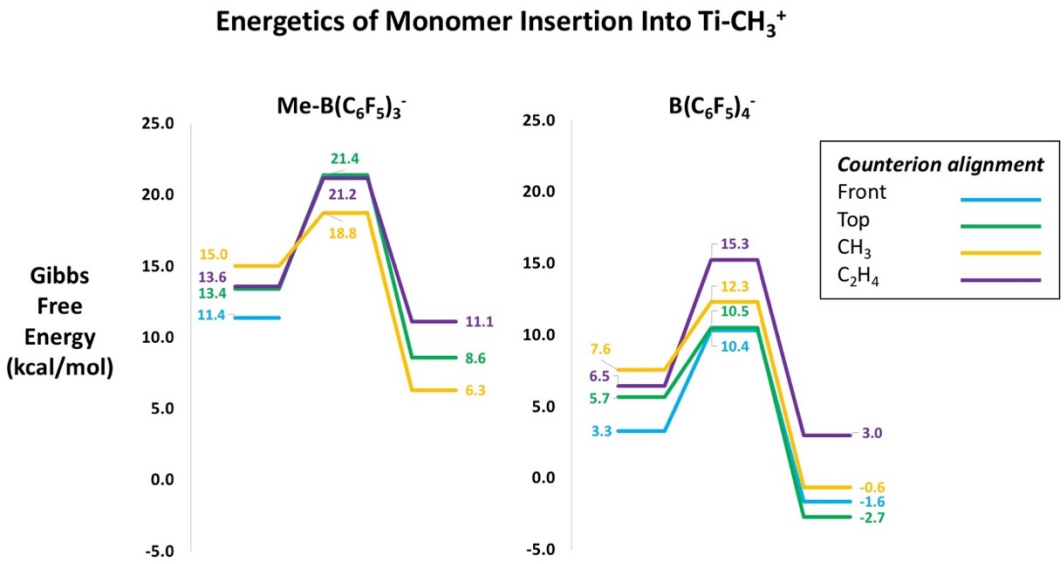

Figure V.6: Potential energy surface for monomer insertion from each counterion alignment with Ti-CH_3^+ complexes for Me-$B(C_6F_5)_3^-$ (left) versus $B(C_6F_5)_4^-$ (right). Energies are referenced to **Int-Ti-Me-B** and **Int-Ti-B**, shown in **Figure V.2**.

Since the CH_3 group on Ti led to low probability alignments, it is probable that as the polymer chain grows counterion-polymer interactions will continue to impact the probability of certain alignments existing in-situ. To look at how the growth of the polymer chain and conformers of the Ti-$C_3H_7^+$ system impacts counterion alignment and monomer insertion the same four initial alignments as shown in **Figure V.5a** were generated with both counterions using all four conformers of Ti-$C_3H_7^+$ discussed in **Chapter IV**.

Alignment with Ti-$C_3H_7^+$

For the Ti-$C_3H_7^+$ complex, the alignments of the counterion with respect to Ti center resulted in 32 initial structures (16 for each counterion). Across the alignments the orientation of the counterion with the Ti-center remains similar to the Ti-CH_3^+ system, however, differences in the propyl chain conformation (**Figure V.7**) gave rise to variation in which alignments are favorable.

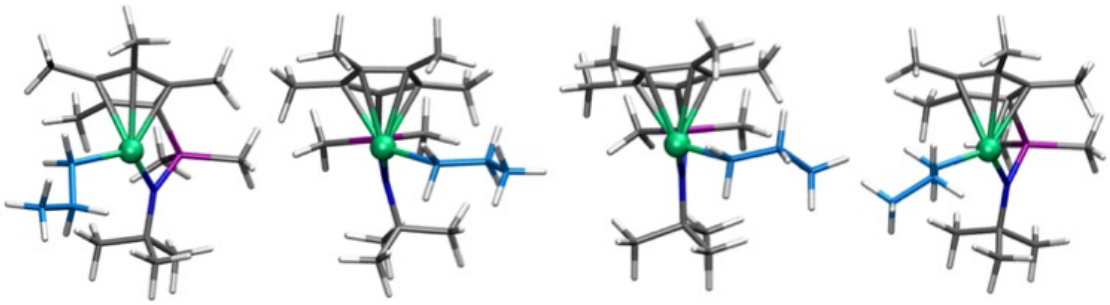

Figure V.7: Ti-$C_3H_7^+$ conformers used to model monomer insertion. The counterion and C_2H_4 have been omitted from the structures for more clarity of the conformer.

With these conformers, the inclusion of the counterion can alter the Ti-propyl chain structure slightly in comparison to their naked cation orientations. In the case of conformer **1**, which starts with the C_2 carbon of the polymer chain oriented down towards the tert-butyl ligand (**Figure V.7** structure 1) the inclusion of Me-$B(C_6F_5)_3^-$ only alters the Ti-$C_{polymer}$ distances by a maximum of 0.15 Å, and the Ti-C_1-C_2-C_3 dihedral angle change by a maximum of 13.2 degrees across all four alignments. Similarly, with the inclusion of $B(C_6F_5)_4^-$ the conformer Ti-C_1-C_2-C_3 dihedral angle changes by a maximum of 17.5 degrees, while the Ti-$C_{polymer}$ distances change by a maximum 0.09 Å from the initial naked cation. the $B(C_6F_5)_4^-$ counterion the Ti-C_3 distance did decrease more from the naked cation by 0.26 to 0.47 Å depending on the alignment.

With conformer 2, the initial naked cation has an η-2 coordination mode with a Ti-C_2 distance of 2.48 Å (**Figure V.7** structure 2). When a counterion is brought into the picture, front alignment of either counterion can break up the Ti-C_2 agostic interaction, as evident by increased Ti-C_2 distances ranging from 3.16 to 3.32 Å. This decrease in Ti-C_2 interaction likely comes from the counterion stabilizing the charge on Ti, which lessens the need or stronger polymer chain coordination to be needed for charge stabilization. With the increase in Ti-C_2 distance, the polymer chain is free to rotate to a more favorable Ti-C_1-C_2 angle. Without a counterion, this angle is 83.3 degrees, but with a counterion, the angle increases to values ranging from 109.0 to 138.0 degrees for both the front and C_2H_4 alignments of the counterion. In contrast, when the counterion is aligned with the propyl chain, the Ti-C_2 interaction remains more intact due to the counterion pushing the propyl chain towards the Ti center, as noted by the Ti-C_1-C_2 angle being

84.6 degrees with Me-B(C_6F_5)$_3^-$ and moving to 100.72 degrees with B(C_6F_5)$_4^-$, compared to 83.3 degrees with the naked counterion. The wider angle with B(C_6F_5)$_4^-$ is attributed to the counterion being less nucleophilic and sitting farther from the Ti-center, which gives the polymer chain more room to move.

For conformer 3, the initial naked cation has the polymer chain oriented to the side of the catalyst, with Ti-C_2 distance of 3.32 Å and a Ti-C_1-C_2 angle of 135.4 degrees (**Figure V.7,** structure 3). The alignments of Me-B(C_6F_5)$_3^-$ and B(C_6F_5)$_4^-$ do not alter the structure significantly. With both counterions the Ti-C_1-C_2 angle and the Ti-C_1-C_2-C_3 dihedral angle change by a maximum of 8.7 degrees, and 15.5 degrees across all structures. With respect to Ti-$C_{polymer}$ distances, the values change by a maximum of 0.13 Å across all alignment/conformer combinations compared to the naked cation structure.

Lastly for conformer 4, the initial naked cation again begins with the C_2 atom of the polymer chain close to Ti with a Ti-C_2 distance of 2.53 Å and a Ti-C_1-C_2 angle of 54.13 degrees. This conformer has the C_2 atom rotated towards the open site on Ti where C_2H_4 is aligned, as noted by the Si-Ti-C_1-C_2 dihedral angle being -178 degrees compared to 20 degrees in conformer 2 (**Figure V.7**, structure 4). With both counterions, alignment with the propyl chain and in front of the counterion pushes the propyl chain towards Ti, preventing C_2 from being able to rotate away from Ti. This is evident by the Ti-B distances for each alignment staying relatively unchanged at 2.8 and 2.7 Å for Me-B(C_6F_5)$_3^-$ and 2.5 Å for both B(C_6F_5)$_4^-$ alignments, while the Ti-C_1-C_2 angles increase slightly to 87 degrees with all of the alignments. In contrast, the C_2H_4 and top alignments allow the polymer chain to rotate away from the Ti center leading to increased Ti-C_2 distances ranging from 3.09-3.27 Å and increased Ti-C_1-C_2 angles ranging from 116-128 degrees.

Overall, the different alignments with both counterions have similar, minimal impact, on changes in how the polymer chain orients itself with respect to the Ti center. When η-2 complexes (close Ti-C_2 distances) are present in the naked cation, the charge balance between the ion pairs allows the Ti-center to rely less on coordination to the polymer chain for stabilization. This allows the Ti-C_2 interactions to be broken up when the counterion is far enough away from the propyl chain to allow for it to move away from Ti.

The Ti-$C_3H_7^+$ complexes with a counterion present have a range of energies from -2.9 to 6.4 kcal/mol for Me-$B(C_6F_5)_3^-$ (referenced to **Int-Ti-Me-B**) where the lowest energy structure has the counterion aligned above the Cp* ligand with conformer 2, shown in **Figure V.8**. In comparison alignment with $B(C_6F_5)_4^-$ led to structures with energies ranging from -9.4 to 1.1 kcal/mol (referenced to **Int-Ti-B**), where the lowest energy structure has the counterion aligned in front of the Ti center with conformer 4. shown in **Figures V.9**. Analysis via Equation 1 shows that certain initial structures are considerably more favorable than others (**Figure V.10**). The top-aligned counterion with conformer 2 of the propyl chain is favorable for both counterion types (P_{align} = 68.4% and 42.0% for Me-$B(C_6F_5)_3^-$ and $B(C_6F_5)_4^-$ respectively). This orientation of the counterion above the Cp* ligand is stabilized because steric interactions that may occur with between the counterion and polymer chain are minimized with B-$C_{polymer}$ distances of at least 7.9 Å and 8.6 Å for each respective counterion, and favorable π-interactions between the pentafluoro rings of the counterion and the Cp* ligand can exist. Additionally, with $B(C_6F_5)_4^-$ alignment of the counterion in front of the Ti-center with conformer 4 also leads to a favorable structure (P_{align} = 53.1%). This alignment allows for an η^2 complex to form between Ti and the polymer chain with Ti-C_1 and Ti-C_2 distances of 2.09 Å and 2.52 Å. Additionally the orientation of the propyl chain allows the counterion is able to stay in relatively close proximity to the Ti center with a B-Ti distance of 6.87 Å, while minimizing Ti-C_1 interactions compared to other front aligned structures. Specifically, the B-C_1 distance with conformer 4 is 7.27 Å while conformers 1, 2 and 3 have B-C_1 distances of 5.87 Å, 5.11 Å and 4.90 Å.

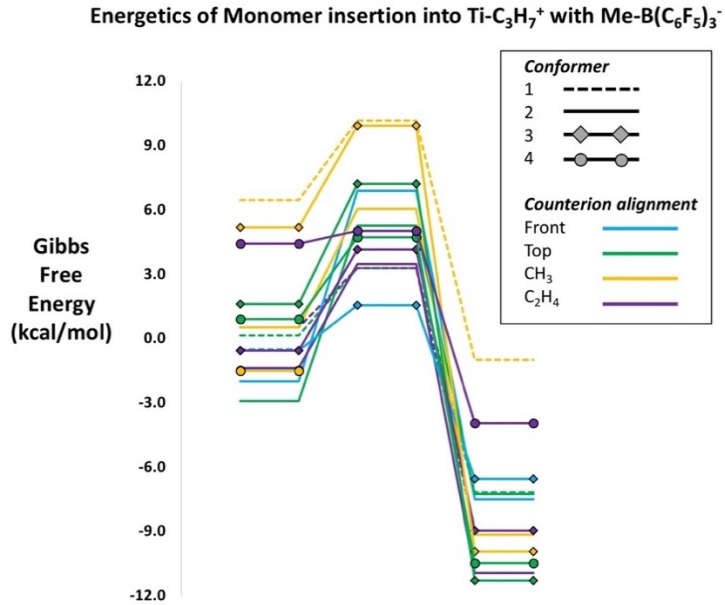

Figure V.8: Gibbs free energy diagram showing the relative difference in energy between reaction pathways to insertion for the four Ti-$C_3H_7^+$ conformers aligned with Me-$B(C_6F_5)_3^-$. Energies are referenced **Int-Ti-Me-B** in **Figure V.3**.

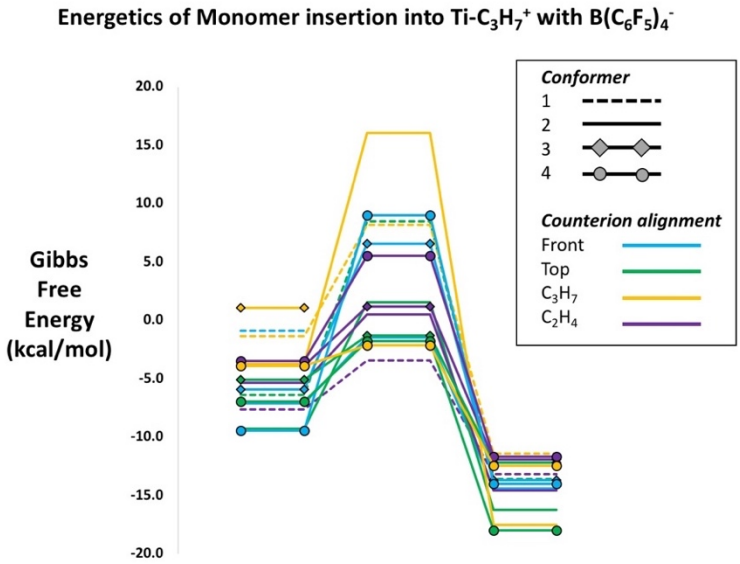

Figure V.9: Gibbs free energy diagram showing the relative difference in energy between initial and TS structures leading to insertion for the four Ti-$C_3H_7^+$ conformers aligned with $B(C_6F_5)_4^-$ Energies are referenced **Int-Ti-Me-B** in **Figure V.3**.

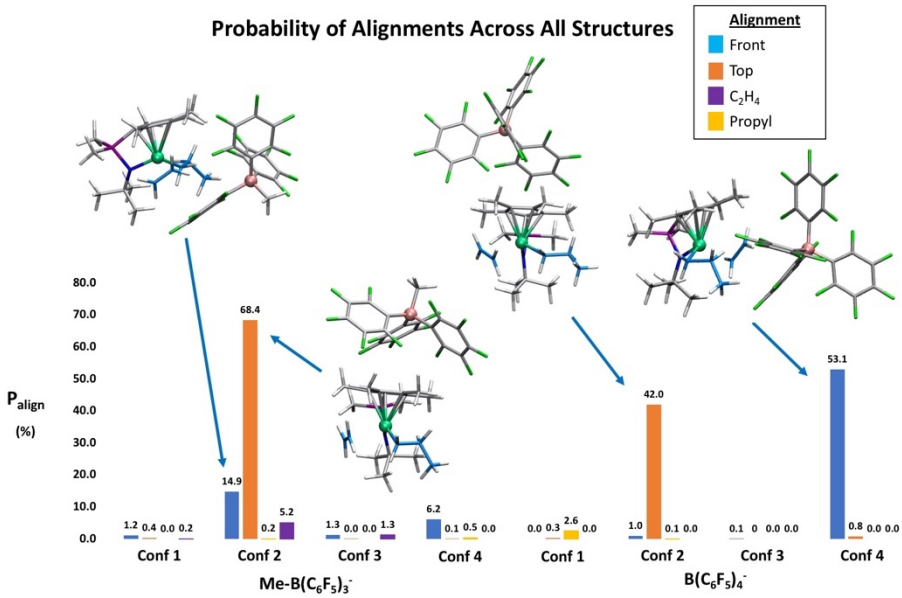

Figure V.10: Partition function-based relative probabilities of each initial structure alignment across all possible structures generated with Me-B(C_6F_5)$_3^-$ (left) and B(C_6F_5)$_4^-$ (right).

The general destabilization of other conformer/alignment combinations with lower relative probabilities tends to stem from differences in the proximity between the counterion and polymer chain and/or Ti center. In comparison to the truncated Ti-CH_3^+, interactions between the elongated polymer chain and counterion can push the counterion farther from Ti which leads to destabilizing steric interactions and less ion pair stabilization from being in close proximity to one another. For example, with Me-B(C_6F_5)$_3^-$ and Ti-CH_3^+ front, CH_3, and C_2H_4 alignments leads to B-CH_3 distances of 5.63 Å, 7.32 Å to 8.31 Å respectively. In comparison, with larger Ti-$C_3H_7^+$ system the closest B-$C_{polymer}$ distance for the front, propyl, and C_2H_4 alignments across all four conformers ranged from 5.1 to 5.7 Å, 4.3 Å to 6.8 Å, and 7.5 Å to 9.2 Å for each alignment respectively. The shorter distances found for B-$C_3H_7^+$ versus B-CH_3^+ interactions indicate more steric clashing between the counterion and propyl chain is present, which pushes the counterion farther from polymer/catalyst and creates less stable structures.

Although the front and top alignment were found to be favorable with both Ti-CH_3^+ and Ti-$C_3H_7^+$ systems respectively, monomer insertion from all of four initial alignments with each Ti-polymer system were assessed to see how the inclusion of a counterion impacts the C-C bond forming process, and to see where the counterion likes to orient itself during insertion.

C_2H_4 Insertion into Ti-CH_3^+ with Me-B(C_6F_5)$_3^-$

After monomer uptake occurs and C_2H_4 is coordinated to the Ti center, monomer insertion has the potential to occur with each of the counterion alignments noted above. From the initial Ti-catalyst-borane complexes three reaction pathways from counterion alignments of Me-B(C_6F_5)$_3^-$ for (1) above Cp*, (2) next to C_2H_4, and (3) next to CH_3 were identified (**Figure V.6**). Front alignment did not lead to a successful reaction pathway for insertion, likely due to steric interactions between Me-B(C_6F_5)$_3^-$, the incoming C_2H_4 monomer and CH_3 impeding the reaction. The B-C_2H_4 distance of 5.33 Å, and the B-CH_3 distance of 5.67 Å suggests that Me-B(C_6F_5)$_3^-$ sits too close to the reactive atoms to allow the C-C bond to form, alignment is shown in **Figure V.11**. In all other alignments the B-C_2H_4 distance ranged from 5.32 (when aligned with C_2H_4) to 9.61 Å and the B-CH_3 distances ranged from 7.32 to 8.78 Å, implying that with the other alignments the counterion was far enough removed from the site of C-C bond formation for the reaction to occur. Although the front alignment is favored pre-monomer insertion, movement of the counterion to other positions at equilibrium should allow insertion to occur. Also, it is known that the rate of monomer insertion with Me-B(C_6F_5)$_3^-$ is slower than with B(C_6F_5)$_4^-$.[309] The fact that no reaction pathway from this low energy structure was found supports the idea that Me-B(C_6F_5)$_3^-$, a strong nucleophile, may coordinate strongly to the Ti-center in ways that can impede insertion.

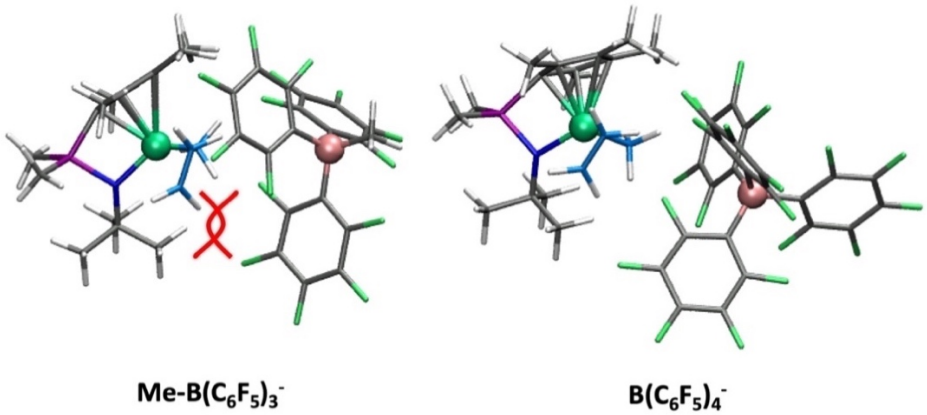

Figure V.11: Comparison of front alignment for Me-B(C_6F_5)$_3^-$ versus B(C_6F_5)$_4^-$

For the productive alignments, barriers to insertion (ΔG_{TS}) ranged from 18.8 to 21.4 kcal/mol, **Figure V.11**, when referenced to **Int-Ti-Me-B**, and the most probable TS (based on Equation 1) is found to be with the counterion oriented next to the Me group (**Figure V.12**). When the counterion occupies this alignment, insertion occurs through this 18.8 kcal/mol barrier, which is larger than the experimental value of 13.3 kcal/mol[308]. When referenced to the monomer and counterion coordinated intermediate ($\Delta G_{Initial}$ = 11.4 kcal/mol), the energy of insertion is 7.4 kcal/mol which is in agreement with the 7.3 kcal/mol barrier reported by Ziegler and co-workers for the initial monomer insertion step when the barrier is referenced to the same monomer and counterion coordinated Ti-complex. [335,336]

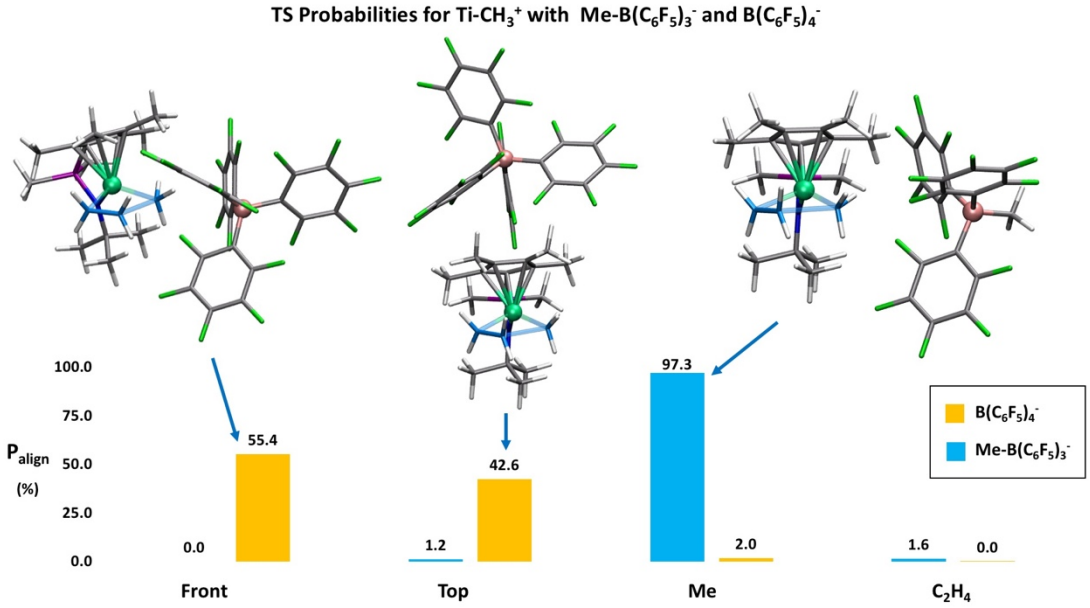

Figure V.12: Relative probability of insertion occurring through the various TSs found for (left) Me-$B(C_6F_5)_3^-$ aligned Ti-CH_3^+ complexes, and (right) $B(C_6F_5)_4^-$ aligned Ti-CH_3^+ complexes.

At the TS for the reaction pathway from each alignment, the orientation of the counterion with respect to the Ti center changes with the CH_3 aligned structure but remains similar with top and C_2H_4 alignment, **Table V.1**. Specifically, in the lowest energy, most probable, pathway the Ti-B distance decreases from 7.32 Å at the initial structure to 6.70 Å at the TS. The movement of the counterion closer to the Ti-center likely helps to stabilize the TS structure. In comparison the TS

structures with higher barriers have longer T-B distances of 6.84 Å and 7.22 Å for C_2H_4 and top alignment respectively. The increased Ti-B distance at the TS likely destabilizes these pathways.

C_2H_4 Insertion into Ti-CH_3^+ with $B(C_6F_5)_4^-$

As was done with Me-$B(C_6F_5)_3^-$ monomer insertion was modeled from the initial ion pair complexes generated with $B(C_6F_5)_4^-$, and another four reaction pathways, one from each of the alignments (1) in front of Ti, (2) above Cp*, (3) next to C_2H_4, and (4) next to CH_3, were identified. The barriers to insertion amongst the different alignments (ΔG_{TS}) ranged from 10.4 to 15.3 kcal/mol (**Figure V.6**) when referenced to **Int-Ti-B**. Based on the relative probability calculated from Equation 1, the most likely pathways for insertion with $B(C_6F_5)_4^-$ differ from Me-$B(C_6F_5)_3^-$. With this less nucleophilic counterion, the front aligned TS and the Cp* aligned TS structures are the most probable pathways (55.4% and 42.6% respectively) with ΔG_{TS} of 10.4 and 10.5 kcal/mol, which are in closer agreement to the experimental value of 13.3 kcal/mol.[308]

At the TS for each of the alignments, the orientation of the counterion with respect to the Ti center changes compared to the initial structure (**Table V.2**). Specifically, the insertion pathway from the most probable structure, front alignment, sees an increase in the Ti-B distance from 5.85 Å to 6.65 Å. The increase in Ti-B distance is likely required in order to avoid impeding C-C bond formation through front alignment of the counterion, shown in **Figure V.11**. The identification of a pathway from this alignment with $B(C_6F_5)_4^-$ compared to Me-$B(C_6F_5)_3^-$ likely stems from the weaker nucleophile having weaker coordination to the Ti center, which allows for the counterion to move away from the Ti center during insertion, thus providing room for the C-C- bond to form. The second most probable TS originates from the top aligned structure and in contrast experiences a decrease in Ti-B distance from 7.49 Å to 7.19 Å. The higher relative probability of insertion occurring through this alignment with the weaker nucleophile could be due to the counterion being less attracted to the cationic Ti-center, which allows for insertion with farther Ti-B distances to be more stable. Finally, as observed with Me-$B(C_6F_5)_3^-$, longer Ti-B distances lead to the less probable pathways, as observed with Me (P_{align} = 2.0%) and C_2H_4 (P_{align} = 0.0%) alignment which have Ti-B distances of 7.35 Å and 7.72 Å.

Based on the energetics and structures obtained for the first monomer insertion step, summarized in **Tables V.1** and **V.2**, more favorable TSs with the $B(C_6F_5)_4^-$ counterion are stabilized by shorter Ti-counterion interactions. Additionally, the weaker nucleophile does not coordinate as strongly to the Ti center (as evident in the monomer uptake step as well), which allows for favorable π-interactions between the counterion and Cp* ligand to stabilize the TS enough to make insertion with top alignment a favorable pathway, despite the longer Ti-B distance.

When the two counterions are compared, the more nucleophilic nature of $Me\text{-}B(C_6F_5)_3^-$ leads to stronger coordination with Ti, which likely makes it harder to separate the ion pair when they are in close proximity (i.e. with front alignment) to allow for insertion to occur. This in combination with the higher energetics of monomer uptake could in turn slow down the rate of polymerization with $Me\text{-}B(C_6F_5)_3^-$ compared to $B(C_6F_5)_4^-$, which is less nucleophilic and has weaker coordination to Ti.[309]

Regardless of differences in what pathways to insertion are favorable, the TS structures found for C-C bond formation for all of the pathways with each counterion remain similar to the TS structures found for the naked cation. In particular, the Ti-C_1, C_1-$C_{olefin\text{-}1}$, $C_{olefin\text{-}1}$-$C_{olefin\text{-}2}$, Ti-$C_{olefin\text{-}2}$ bond distances at the TS (found in **Table V.3**) with $Me\text{-}B(C_6F_5)_3^-$ averaged out to 2.15 Å, 2.22 Å, 1.41 Å, and 2.18 Å. These same distances with $B(C_6F_5)_4^-$ averaged out to 2.14 Å, 2.21 Å, 1.42 Å, and 2.16 Å, indicating that the choice of counterion or alignment does not significantly alter the structure of the 4-member TS leading to insertion with the truncated Ti-CH_3 system.

Table V.3: Transition state bond distances between Ti, C_2H_4 and the polymer chain. Distances for the conformers are averaged across all alignments. All bond distances are in Å and all angles are in degrees.

System	Ti-C_1 dist.	C_1-$C_{olefin\text{-}1}$ dist.	$C_{olefin\text{-}1}$-$C_{olefin\text{-}2}$ dist.	Ti-$C_{olefin\text{-}2}$ dist.
Ti-CH_3^+				
Reference[334]	2.15	3.00	1.34	2.38
No counterion	2.15	2.16	1.41	2.22
$Me\text{-}B(C_6F_5)_3^-$	2.15	2.22	1.41	2.18
$B(C_6F_5)_{4\text{-}}$	2.14	2.21	1.42	2.16
Ti-$C3H_7^+$ - no counterion				
Conformer 1	2.16	2.21	1.41	2.21
Conformer 2	2.21	2.18	1.41	2.22
Conformer 3	2.30	2.08	1.43	2.18
Conformer 4	2.12	2.37	1.39	2.30
Ti-$C3H_7^+$ - $Me\text{-}B(C_6F_5)_3^-$				
Conformer 1	2.17	2.21	1.41	2.20

Conformer 2	2.29	2.18	1.43	2.10
Conformer 3	2.29	2.19	1.42	2.11
Conformer 4	2.14	2.25	1.40	2.25
Ti-C3H$_7^+$ - B(C$_6$F$_5$)$_4^-$				
Conformer 1	2.15	2.19	1.41	2.21
Conformer 2	2.31	2.04	1.44	2.17
Conformer 3	2.31	2.02	1.44	2.14
Conformer 4	2.12	2.27	1.40	2.25

From these investigations into the initial monomer insertion step it is clear that sampling the alignment of counterion is important to understanding which initial structures and pathways are favorable to monomer insertion. Additionally, some alignments, appear to impact the ability to find successful reaction pathways for monomer insertion, as was observed with front alignment of Me-B(C$_6$F$_5$)$_3^-$. With this in mind, the second insertion step was modeled for each counterion and propyl chain conformer in order to see how the two variables together impact insertion.

C$_2$H$_4$ Insertion into Ti-C$_3$H$_7^+$ with Me-B(C$_6$F$_5$)$_3^-$

After the second monomer uptake step, leading to C$_2$H$_4$ coordinated Ti-C$_3$H$_7^+$ complexes, Me-B(C$_6$F$_5$)$_3^-$ was aligned with each propyl chain conformer in the same orientations, discussed previously and shown in **Figure V.7**. From these complexes reaction pathways tor monomer insertion from 13 of the 16 initial structures were identified. See *Appendix D* for specific reaction pathway energetics.

From the successful reaction path searches, barriers to insertion (ΔG_{TS}) ranged from 14.8 to 23.4 kcal/mol, when referenced to **Int-Ti-Me-B-2**. The most probable configuration becomes insertion with propyl chain conformer 3 and the counterion oriented in front of the Ti-center (ΔG_{TS} = 14.8 kcal/mol, P_{align} = 85.3%, see **Figure V.13**). This barrier is lower than the first insertion step however this matches reports by Ziegler and co-workers that showed the second insertion step having a lower barrier than the first. [335,336] As was the case with the first insertion step, the need to disrupt the stable Ti-Me-B bridge in **Int-Ti-Me-B-2** increases the barrier for monomer insertion to occur.

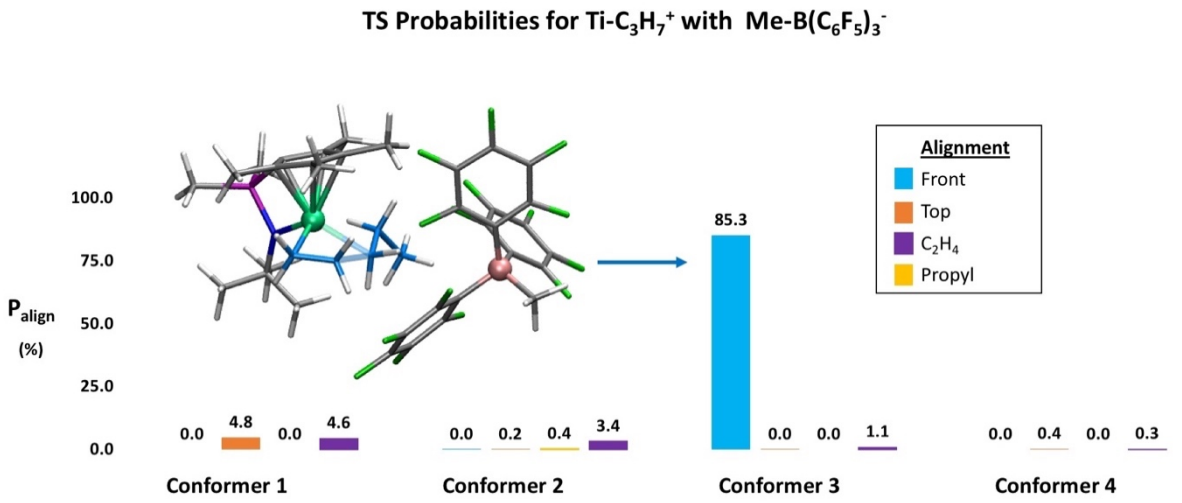

Figure V.13: Relative probability of monomer insertion occurring through each TS found for the Ti-$C_3H_7^+$ system aligned with Me-$B(C_6F_5)_3^-$

When the structure of the TSs found across all of the initial structures are looked at the general features remained somewhat unchanged and were similar to the features found for insertion without a counterion. Specifically, the average distances between Ti-C_1, C_1-$C_{olefin-1}$, $C_{olefin-1}$-$C_{olefin-2}$, and Ti-$C_{olefin-2}$ at the TS with Me-$B(C_6F_5)_3^-$ are 2.22 Å, 2.17 Å, 1.42 Å, and 2.21 Å as compared to 2.20 Å, 2.21 Å, 1.41 Å, and 2.23 Å for Ti-$C_3H_7^+$ without a counterion, **Table V.3**. The similar distances show that the general 4-member TS structure at the Ti center still remains relatively unchanged regardless of combining various conformers with counterion alignments.

If reaction pathways from specific conformers are looked at in more detail, successful reaction pathway and TS searches with all four alignments combined with conformers 2 and 3 were found. On the other hand, with conformer 1 where the polymer chain extends out in front of the Ti-center, no successful reaction path was found for insertion with the counterion aligned in front of the Ti-center. This can be attributed to Me-$B(C_6F_5)_3^-$ blocking C-C bond formation through its close proximity to the polymer chain. This blocking of C-C bond formation is evident by the B-C_2H_4, and B-Ti distances of 4.67 Å and 6.06 Å for conformer 1 as compared to the average B-C_2H_4 and B-Ti distances of 6.24 Å and 5.47 Å with the other front aligned structures, **Table V.4**. The decreased B-C_2H_4 distance in the front alignment likely makes C-C bond formation more challenging as the counterions close proximity may block the monomer from moving closer to

the polymer chain for insertion to occur. All other alignments with conformer 1 did lead to successful reaction path searches though.

Table V.4: Distances between the boron atom of Me-$B(C_6F_5)_3^-$ and the polymer chain carbon atoms (C_1, C_2, and C_3), Ti-center, and C_2H_4 monomer for initial Ti-$C_3H_7^+$. Distances are reported in Å.

	B-C_1	**B-C_2**	**B-C_3**	**B-Ti**	**B-C_2H_4**
Avg. Dist. (All Other Me-$B(C_6F_5)_3^-$ Alignments)	7.81	8.16	8.86	7.09	7.72
Avg. Dist. (Front alignment with conformers 2,3,4)	5.52	5.92	6.08	6.24	5.34
Dist. Front alignment with conformer 1	5.88	5.39	5.57	6.06	4.67

Lastly, with conformer 4, successful reaction path and TS searches for monomer insertion were only found for two alignments: when the counterion was aligned next to the C_2H_4 monomer or above the Cp* ligand. With this conformer the C_2 atom of the polymer chain is oriented towards the incoming monomer, with an Si-Ti-C_1-C_2 dihedral angle of -158 degrees, and sits closer to the Ti center as evident by the Ti-C_2 average distance of 2.41 Å compared to 3.16 Å, 2.86 Å, and 3.28 Å for conformers 1,2, and 3. This orientation of the C_2 atom causes the C_1 atom of the polymer chain to be rotated away from the incoming monomer, which can be quantified by the distance between C_1 and C_2H_4 for conformer 4 being 4.69 Å, versus C_1-C_2H_4 distances of 3.26 Å, 3.22 Å, and 3.42 Å for conformers 1, 2 and 3, **Table V.5**. With this rotation of the polymer chain in conformer 4, the C_2 atom needs to be able to move away from the incoming monomer, to allow for the C-C bond to form between C_1 and C_2H_4. Therefore, when Me-$B(C_6F_5)_3^-$ is aligned in front of Ti or next to the polymer chain rotation away is impeded, and thus blocks insertion from occurring.

Table V.5: Distances between the C_1 and C_2 atoms of the polymer chain and C_2H_4 monomer for initial Ti-$C_3H_7^+$ - Me-$B(C_6F_5)_3^-$ complexes. Distances are reported in Å.

	C_1-C_2H_4	**C_2-C_2H_4**
Avg. Dist. Conformers 1,2,3	3.53	4.65
Avg. Dist. Conformer 4	3.80	4.02

Although some pathways to insertion were inhibited by certain conformer/alignment combinations, a favorable pathway to insertion through the front alignment of Me-B$(C_6F_5)_3^-$ with conformer 3 was identified. (P_{align} = 85.3%, **Figure V.13)** Although the top alignment of the counterion with Ti-$C_3H_7^+$ is favored initially, at the TS counterion alignment close to the Ti-center is favored, as was the case with Ti-CH_3^+. The front alignment of the counterion with conformer 3 allows the counterion to be close enough to the Ti-center to stabilize the TS, while the longer polymer chain causes some steric interactions that help to push the strong nucleophile away from the Ti-center during insertion, which prevents this alignment from impeding C-C bond formation. (The Ti-B distance increases from 6.3 Å initially to 6.7 Å at the TS.) In contrast the less probable pathways involving top, propyl, and C_2H_4 alignments with other conformers have either (1) weaker Ti-counterion interactions (longer Ti-B distances) or (2) unfavorable steric interactions between the counter ion and polymer chain or monomer. For instance, insertion through front alignment with conformer 2 is less favorable (P_{align} = 3.1%) because of a longer Ti-B distance of 6.9 Å at the TS. (All Ti-B distances for the TS structures and initial structures can be found in **Table V.3**.

Based on the differences in monomer uptake and insertion noted for the initial step between the two counterions, the second insertion step was also modeled with B$(C_6F_5)_4^-$ to see how the weaker coordination combined with various conformers of Ti-$C_3H_7^+$ impacts monomer uptake and insertion in comparison to Me-B$(C_6F_5)_3^-$.

C_2H_4 Insertion into Ti-$C_3H_7^+$ with B$(C_6F_5)_4^-$

As was done with Me-B$(C_6F_5)_3^-$, monomer insertion from the C_2H_4 coordinated Ti-$C_3H_7^+$ complexes formed after the second monomer uptake step were modeled with B$(C_6F_5)_4^-$ aligned with each propyl chain conformer in the same orientations, discussed previously and shown in **Figure V.5**. From these complexes reaction pathways and TSs for monomer insertion from 14 of the 16 initial structures were identified, see *Appendix* for insertion barriers for specific reaction pathways.

From the successful reaction path searches, activation barriers for insertion (ΔG_{TS}) ranged from 9.9 to 29.3 kcal/mol when referenced to the **Int-Ti-B-2**, **Figure V.4**. Using equation 1 the

relative probability of each TS found for insertion can be calculated. This assessment identifies the most probable pathway to insertion occurring with the counterion aligned with the C_2H_4 monomer and conformer 1 of the propyl chain, **Figure V.14** (ΔG_{TS} = 9.9 kcal/mol, P_{align} = 84.5%). The 9.9 kcal/mol barrier falls in line with the initial monomer insertion barrier for $B(C_6F_5)_4$- of 10.4 kcal/mol.

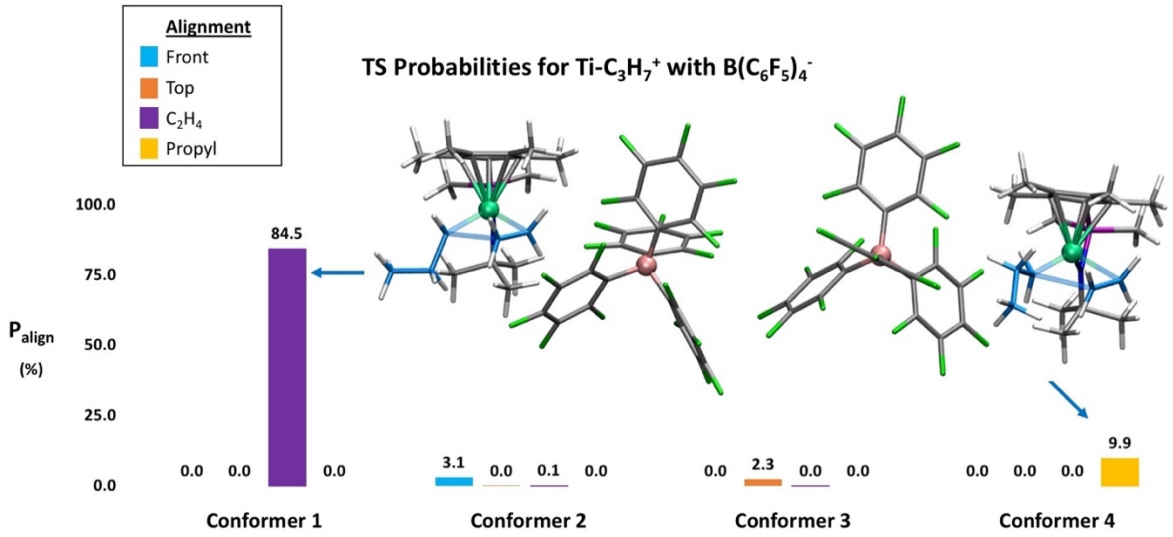

Figure V.14: Relative probability of monomer insertion occurring through each TS found for the Ti-$C_3H_7^+$ system aligned with $B(C_6F_5)_4^-$

When the structure of the TSs found across all of the initial structures are looked at the general features remained somewhat unchanged and are similar to the features found for insertion without a counterion. Specifically, the average distances between Ti-C_1, C_1-$C_{olefin-1}$, $C_{olefin-1}$-$C_{olefin-2}$, and Ti- $C_{olefin-2}$ at the TS with $B(C_6F_5)_4^-$ are 2.24 Å, 2.11 Å, 1.42 Å, and 2.19 Å as compared to 2.20 Å, 2.21 Å, 1.41 Å, and 2.23 Å for Ti-$C_3H_7^+$ without a counterion, **Table V.3**. The similar distances show that the general TS structure at the Ti center remains relatively unchanged regardless of changing the counterion from Me-$B(C_6F_5)_3^-$ to $B(C_6F_5)_4^-$.

If reaction pathways from specific conformers are looked at more specifically though, conformers 2 and 4 led to successful reaction path and TS searches all four counterion alignments. On the other hand, with conformer 1, no successful reaction path was found for insertion with the counterion aligned in front of the Ti-center, while all other alignments led to successful insertion pathways. In this case $B(C_6F_5)_4^-$ likely blocks C-C bond formation due to its

close proximity to the incoming C_2H_4 monomer compared to the other front aligned structures for conformer 2, 3 and 4. Specifically, the shorter B-C_2H_4 distance of 5.2 Å for conformer compared to distances of 5.5 Å, 5.7 Å and 5.8 Å for conformers 2, 3, and 4 likely impedes insertion, as was also found with Me-B$(C_6F_5)_3^-$

Lastly, with conformer 3, alignment with the polymer chain did not lead to a successful pathway search for insertion, whereas all other alignments did. With the propyl alignment, the polymer chain is oriented towards the counterion and pushes it away from the catalyst leading to a large Ti-B distance of 7.9 Å. This distance is larger than any other observed Ti-B distance across all other initial structures for B$(C_6F_5)_4^-$ complexes. The Ti-B distance leads to an unstable ion pair complex, which raises the energy of the system making monomer insertion from this structure unlikely.

Despite some alignments impeding insertion, a favorable pathway to insertion was found for C_2H_4 alignment of B$(C_6F_5)_4^-$ with conformer 1 (P_{align} = 84.5%, **Figure V.14**). Although the front alignment with conformer 4 and top alignment with conformer 2 is favored initially, at the TS the counterion wants to be close to the Ti-center as has been observed in the other systems discussed above. The C_2H_4 alignment with conformer 1 allows for the closest Ti-B distance amongst all of the TS structures identified, with a distance of 6.4 Å. (All other Ti-B distances at the TS structure for each respective pathway are 6.7 Å or more). The shorter Ti-B distance observed for the most probable TS with B$(C_6F_5)_4^-$ compared to Me-B$(C_6F_5)_3^-$ likely stems from no steric interactions between the polymer chain and counterion being present with C_2H_4 alignment, as the B-C_1-, -C_2, and -C_3 distances are 7.70 Å, 8.2 Å, and 9.7 Å. Additionally, alignment with the C_2H_4 monomer puts the counterion closer to where the open site on Ti would be, which likely pulls the counterion slightly closer to the Ti center in comparison to other alignments. The greater probability of monomer insertion with conformer 1 is likely due to a greater Ti-C_2 distance at the TS of conformer 1 (3.4 Å) compared to conformer 2 (2.5 Å) or 3 (2.5 Å), **Table V.6**. The lack of steric interactions with the polymer chain, combined with the close Ti-B interaction makes insertion through this TS favorable.

Just as was the case with Me-B$(C_6F_5)_3^-$ less probable pathways for insertion with B$(C_6F_5)_4^-$ have either (1) weaker Ti-counterion interactions (longer Ti-B distances) or (2) unfavorable steric

interactions between counterion and polymer chain or monomer. For instance, elongated Ti-B distances of 6.7 Å, 6.8 Å, and 6.9 Å at the TS for C_2H_4 alignment with conformer 2, 3 and 4 make these pathways less favorable. Whereas, farther C_1-, C_2-, and C_3-B distances of 7.7 Å, 8.2 Å, and 9.7 Å in the C_2H_4 alignment with conformer 1 give rise to the most probable pathway.

Overall, modeling monomer insertion from the most probable structure gave rise to a reaction pathway with a calculated barrier of 9.9 kcal/mol that is lower than the barrier found for Me-$B(C_6F_5)_3^-$ of 14.8 kcal/mol for the second insertion step. This difference in barrier matches with the observance of a faster rate of polymerization with $B(C_6F_5)_4^-$ compared to Me-$B(C_6F_5)_3^-$.[309]

Table V.6: Ti-$C_{polymer}$ distances at the TS structure during monomer insertion for conformers 1,2,3 and 4. All distances are reported in Å.

	Ti-C_1	**Ti-C_2**	**Ti-C_3**
Distance – conformer 1 (C_2H_4 alignment)	2.2	3.4	4.4
Avg. Distance – conformer 1 (Front, top, propyl alignments)	2.2	3.4	4.6
Avg. Distance – conformer 2 (Front, top, C_2H_4, and propyl alignments)	2.3	2.5	3.9
Avg. Distance – conformer 3 (Front, top, C_2H_4, and propyl alignments)	2.3	2.5	3.6
Avg. Distance – conformer 4 (Front, top, C_2H_4, and propyl alignments)	2.1	3.5	4.6

Discussion

When the overall mechanism for counterion coordination, displacement of the counterion by C_2H_4 through monomer uptake, monomer insertion and counterion recoordination, **Figure V.1**, are looked at with Me-$B(C_6F_5)_3^-$ and $B(C_6F_5)_4^-$ for the first and second insertion steps it becomes clear that differences in how the counterion coordinated to Ti leads to the different rates of reaction observed between the two counterions. In the case of Me-$B(C_6F_5)_3^-$ the coordination of the counterion to the Ti center open site, prior to monomer uptake, leads to the formation of a Ti-Me-B bridging species, **Figures V.3** and **V.4**, that are thermodynamically stable prior to both the first and second insertion steps. In order for a monomer to coordinate to Ti, and subsequent insertion to occur, the incoming monomer has to

disrupt the Ti-Me-B bridge and displace the counterion at the open site on Ti, which is an energetically unfavorable process leading uphill 11.4 and 10.3 kcal/mol for the first and second uptake steps. In contrast, with $B(C_6F_5)_4^-$, no Me group is present to form a Ti-Me-B bridge, and the weaker coordinating strength of $B(C_6F_5)_4^-$ allows for monomer uptake to be a less energetically demanding process only leading uphill in energy by 3.3 and 3.9 kcal/mol for the first and second uptake steps.

When the energetics of monomer insertion are compared between the two counterions, the increase in monomer uptake with Me-$B(C_6F_5)_3^-$ leads to higher insertion barriers of 18.8 and 14.8 kcal/mol for the first and second insertion steps compared to barriers of 10.4 and 9.9 kcal/mol for the first and second insertion steps with $B(C_6F_5)_4^-$. This difference in monomer uptake energetics and subsequently monomer insertion barriers, can explain the slower rate of polymerization with Me-$B(C_6F_5)_3^-$ compared to $B(C_6F_5)_4^-$ observed experimentally.[309]

When the alignments of the counterion and Ti-Polymer complexes are looked in more depth and compared to one another for the monomer insertion process, both counterions preferred front alignment with the truncated Ti-CH_3^+ system. With the Ti-$C_3H_7^+$ though, Me-$B(C_6F_5)_3^-$ and $B(C_6F_5)_4^-$ are found to have different counterion alignment/propyl chain combinations that lead to probable initial structures prior to monomer insertion. In both cases though, favorable alignments have the counterion oriented either in front of the catalyst or above the Cp* ligand.

At the TSs for monomer insertion both counterions also have different alignments that lead to favorable pathways, however they share a common feature of the counterion being in close proximity to the Ti center with both Ti-CH_3^+ and Ti-$C_3H_7^+$. In the case of Me-$B(C_6F_5)_3^-$ the most probable pathways had Ti-B distance at the TS of 6.7 Å for both systems. Similarly, the most probable pathways for $B(C_6F_5)_4^-$ had Ti-B distances of 6.7 Å and 6.4 Å with Ti-CH_3^+ and Ti-$C_3H_7^+$,respectively. These complexes also had minimized steric interactions with the polymer chain and site of C-C bond formation at the TS, distances can be found in **Tables V.1, V.2** for Ti-CH_3^+ and **Tables D.1** and **D.2** in *Appendix D* for Ti-$C_3H_7^+$.

Although favorable TS structures tend to have stronger ion pair interactions, too strong of interactions, or alignments that prevented polymer chain movement, were found to impede

the ability of SE-GSM to find pathways to monomer insertion. For instance, with the Ti-CH_3^+ system and Ti-$C_3H_7^+$ system alignment with Me-$B(C_6F_5)_3^+$ in front of certain Ti-polymer structures (for example conformer 1 of Ti-$C_3H_7^+$) can block monomer insertion due to the close proximity of the counterion to where C-C bond formation occurs. In contrast though, front alignments with other conformers (i.e. conformer 3) were found to give rise to the most probable pathway to monomer insertion. Specifically, in the case of conformer 3, the orientation of the polymer chain was able to push the counterion slightly farther away from Ti (initial Ti-B distances of 6.1 Å and 6.3 Å for conformer 1 and 3 respectively), leading to weaker interactions that allow the counterion to move away from Ti at the TS so that C-C bond formation can occur (as observed with a change in Ti-B distance from 6.3 to 6.7 Å with conformer 3). Other conformer/alignment combinations were also found to impede monomer insertion, particularly front and propyl alignment with conformer 4. Impediment occurred because the alignment of the counterion prevented the rotation of the C_2 atom away from Ti, which is necessary for the C_1 atom to form a bond with the incoming C_2H_4 monomer.

In comparison, with the less nucleophilic counterion $B(C_6F_5)_4^-$, the same trend was observed where the counterion wanted to be in close proximity to the Ti center. However, the weaker ion pair interactions led to the ability to find pathways to insertion from alignments that failed to lead to monomer insertion with Me-$B(C_6F_5)_3^-$. For example, with the Ti-CH_3^+ system, front alignment does not impede reactivity with $B(C_6F_5)_4^-$, and instead becomes the most probable pathway to monomer insertion. This can be attributed to the weaker nucleophile being able to move away from Ti center during insertion (Ti-B = 6.7 Å at the TS) despite the close initial Ti-B distance of 5.9 Å. When the system size is increased to Ti-$C_3H_7^+$ the consideration of conformers and the increased polymer chain length leads to the TS from conformer 1 with counterion aligned with C_2H_4 to be the most probable. With the counterion on the C_2H_4 side of the catalyst it can remain close to the Ti center during insertion (Ti-B = 6.4 Å), while also minimizing steric interactions with the propyl chain. Lastly, just as was the case with Me-$B(C_6F_5)_3^-$, there were some alignment/conformer combinations that inhibited finding pathways to monomer insertion. For instance, front alignment with conformer 1 led to the counterion

blocking the site of C-C- bond formation due to the close proximity of the counterion to C_2H_4 (B-C_2H_4 = 5.2 Å).

Overall, the sampling of alignments and conformers demonstrated that the choice of which conformer/alignment combination is used to model insertion can directly impact not only the barrier found to insertion, but also whether or not an insertion pathway will be found using computational modeling. Therefore, choosing the wrong conformer/alignment combination for a model may lead to finding high barrier reaction pathways or no reaction pathways at all, which can lead to generation of unphysical models that do not reflect experiment. If computations are to be used to help guide experimental design, then sampling of various alignments and conformers is important for working towards understanding how a reagent will interact with a catalyst or substrate of interest. For instance, looking into counterion alignments with the Cp* ligand has been neglected in past computational studies however, this sampling actually shows that these alignments can be somewhat favorable initially compared to C_2H_4, propyl, and front alignments with Ti-$C_3H_7^+$. Additionally, sampling allows for generating a variety of TS structures that can be looked at in detail. Investigations into the TS structures allowed for determining two factors that impact whether or not a pathway will be favorable:

I. Minimizing Ti-B distance
II. Minimizing steric interactions between the polymer chain and counterion

In addition to these features TS sampling allowed for the conclusion to be drawn that the inclusion of a counterion or changes in polymer chain conformation do not significantly impact the mechanism by which insertion occurs. By assessing average Ti-C_1, C_1-$C_{olefin\text{-}1}$, Ti-$C_{olefin\text{-}2}$, and $C_{olefin\text{-}1}$-$C_{olefin\text{-}2}$ distances, differences amongst TS structures for each system studied were compared, and in this case the general structure of the 4-member TS for insertion remained similar across all of the systems studied in both **Chapter IV** and **V**.

Lastly, across all of the sampling of aligned structures and reaction pathways, the increased nucleophilicity of the Me-B$(C_6F_5)_3^-$ counterion was found to create a stronger ion-pair interaction with the Ti-center. This stronger interaction can lead to the formation of stable Ti-

Me-B bridging intermediate prior to monomer uptake. This strong interaction raises the barrier to insertion, and may make it harder for the counterion to move away from the Ti center to allow for C-C bond formation to occur post monomer uptake. The strong ion pair interactions and increased energy of monomer uptake found with Me-$B(C_6F_5)_3^-$ compared to $B(C_6F_5)_4^-$ helps to explain why there is a slower observed rate for polymerization with Me-$B(C_6F_5)_3^-$ compared to $B(C_6F_5)_4^-$. [309]

Conclusions

In general, the alignment of a counterion with either Ti-CH_3^+ or Ti-$C_3H_7^+$ allowed the energetics associated with monomer uptake and insertion to be compared so that differences in reactivity between the two counterions could be assessed. The calculated insertion barriers for $B(C_6F_5)_4^-$ were found to fall roughly in line with experimental polymerization barriers found for the Ti-CGC catalyst,[308] while the barrier for Me-$B(C_6F_5)_3^-$ was found to be higher in energy when the most probable pathways were looked at. The observance of a higher barrier to monomer insertion with Me-$B(C_6F_5)_3^-$ matches the experimental observation of slower rates of polymerization when this counterion is used.[309] The sampling of alignments, and conformers with Ti-$C_3H_7^+$ allowed for the relative probability of each pathway to be calculated and comparisons between favorable and unfavorable pathways could be made. From all of the various TS structures that were sampled it becomes clear that the counterion wants to remain in close proximity to the Ti center during insertion, however the interactions between the counterion and Ti-center need to be weak enough to allow for the counterion to move away from the Ti center to allow for monomer uptake and insertion to occur. This is especially true if the initial alignment prior to monomer insertion is in front of the Ti-center. Results of this work also showed that favorable structures tended to avoid steric interactions between the polymer chain and counterion as much as possible, indicating that in solution, increased polymer chain length likely repels the counterion away from the Ti-center/polymer chain. Sampling also allowed for the identification of some unfavorable alignment/conformer combinations that impeded the ability to find successful reaction pathways to monomer insertion, demonstrating that careful consideration (or conformer/alignment sampling) is needed when modeling reactions to ensure

alignments between reagents won't impede computational methods ability to find reaction pathways.

When all of the TS generated are looked at in detail, the 4-member structure that forms between Ti, C_1, $C_{olefin-1}$ and $C_{olefin-2}$ remained similar across all of the systems studied, with small variations in Ti-C_1, C_1-$C_{olefin-1}$, $C_{olefin-1}$-$C_{olefin-2}$, and Ti-$C_{olefin-2}$ distances. This suggests that even though counterion choice impacts the energetics of monomer uptake and insertion it does not directly impact the mechanism by which polymerization occurs.

In future studies of flexible chemical systems, where additives are present, the alignment of additives and various conformers of the reactant can provide insight towards how the two variables interact to either impede or improve reactivity. This can lead to an understanding of how different additives alter the rates to reactions. If computational methods are used prior to experiment this understanding could potentially help guide the choice of what reagents to use experimentally. The limited need for chemical knowledge to generate the aligned structures and conformers demonstrated in this work, shows that the automated method of CGen can expand the scope of chemical space that can systematically be explored, and give more insight into important reactant-reagent interactions that may not be captured without conformer/alignment sampling.

CHAPTER VI

Conclusions

Reaction mechanisms are powerful conceptual tools that allow chemists to gain atomistic insight into the complexities of chemical transformations.[1-3] When mechanisms are explored by-hand, chemists tend to rely on chemical intuition[31-33], experimental data[75-82], or truncated model systems[101,108,240-242] to develop mechanisms that aim to explain experimental outcomes. These methods for generating reaction mechanisms work well[1,2,3,31-33,41,42], but the ability of computational chemistry to be used as a tool to discover new mechanisms is often left untouched. This is due to the data, approximations, and assumptions used to generate mechanisms limiting the scope of chemical space that is searched. Through the use of automated reaction discovery tools, the doors to uncovering reaction mechanisms with less reliance on user input, data, approximations, and assumptions has become more feasible.[60] Specifically the development and use of ZStruct[97] and CGen described in this work, has opened the door to exploring chemical reactivity involving not only the main reactants (i.e. catalyst and substrate), but also the inclusion of additional reagents as well.

Some of the methods available for reaction discovery are limited by the need for experimental data, or the generation of intermediate structures prior to reaction discovery taking place. [75-78] The benefit of ZStruct in contrast to these methods is that no intermediate structure generation or experimental data is needed for reaction discovery. By ZStruct[97] making use of SE-GSM[109] only knowledge of which atoms on a reactant are participating in bond forming or breaking steps is needed so that reaction pathways can be generated. ZStruct also is able to take care of aligning structures to generate initial reactant complexes even in the case where the geometry of transition metal centers requires alignments with multiple faces of the metal, thus allowing for bimolecular reactions to be modeled in a systematic way. As was demonstrated in this work, reaction discovery with ZStruct has led to a variety of chemical systems being looked

at in detail to find chemically intuitive and unintuitive pathways as well as identify key interactions between reactants and reagents. For example: 10 previously unexplored pathways for C-H activation of methane by cisplatin were identified, routes to catalyst poisoning through β-hydride elimination or the formation of Ni-THF and Ni-pyridine complexes were found for Ni(II)-catalyzed co-polymerization reactions, and the catalytic cycle and roles of ArI and Cs-acetate were uncovered for Pd-catalyzed piperidine arylation, all of which would not have been as easily identified without the use of ZStruct and SE-GSM.

The success of ZStruct in these works as well as others[99-110] lead to two realizations: (1) conformational changes of flexible molecules can impact reactivity. (2) Reagent interactions can be detrimental to creating models that reflect experimental conditions, and the alignment of reactants and additives by hand may not be sufficient for generating accurate models.

To further expand computations ability to discover reaction mechanisms and fill in the gaps associated with modeling conformational changes and reagent interactions, the method CGen was developed to generate conformers of flexible reactants and also align reagents with a chemical system of interest. When CGen is coupled with ZStruct and SE-GSM it further expands the computations ability to explore chemical space and create more accurate models.

Ultimately, combining CGen, ZStruct and SE-GSM allowed for Ti-CGC polymerization to be looked at in detail both with and without a counterion present. Without a counterion, monomer insertion the conformational changes of the polymer chain were found to not impact the TS structure through which monomer insertion occurs. However, conformational changes did impact the energetics to monomer insertion as more favorable pathways prefer to have larger Ti-Polymer distances to reduce steric interactions and leave a more open coordination site on Ti for C_2H_4 coordination.

When a counterion was included in the model it was still found that the transition state through which monomer insertion occurs is not altered. However, the coordinating ability of the counterion does impact the energetics associated with monomer uptake and insertion, as stronger coordination with Me-$B(C_6F_5)_3^-$ led to the formation of a Ti-Me-B bridging species that has to be displaced in order for polymerization to occur. Additionally, the alignment capabilities of CGen demonstrated that certain counterion alignment/polymer chain conformations are

energetically favorable, while other combinations actually impede monomer insertion, leading to unsuccessful reaction path searches.

From the use of ZStruct[97] and CGen along with SE-GSM[109], a greater scope of chemical space has been able to be explored in the transition metal catalyzed reactions discussed within this work than previous computational studies were capable of handling. The insight gained is helpful in building a better understanding of how transition metal catalyzed reactions occur, and what factors increase or inhibit reactivity. These studies ultimately led to a few general conclusions regarding the importance of modeling conformational changes and additive interactions to garner more accurate chemical models.

I. Modeling of reagent interactions can identify if they help to drive forward or impede a reaction, conclusions which can remain ambiguous without modeling.
II. Conformational changes can alter the energetics of initial and TS structures independently on one another, leading to variations in calculated activation barriers, which may not reflect experimental results.
III. The choice of reagent alignment or conformation may impact computational methods ability to find reaction pathways, which can lead to the false indication that a reaction may be improbable when sampling is neglected.

Overall, the methods described in this work provide tools that allow for computational chemists ability to create more accurate models of chemical reactions. However, there are still areas of chemical interest that remain challenging to model including: enzymatic reactions, capturing solvation effects, and modeling bimetallic reactions, to name a few. To automate reaction discovery in these areas of interest improvements in tools like ZStruct are needed.

Future of Automated Reaction Discovery

With the availability of these new methods for automating reaction discovery the scope of chemical space that can be explored now can include multiple reactants, additional reagents, and conformational changes of flexible molecules. Additionally, other methods that are also

working towards automated reaction discovery are in development by groups such as Reiher et al[55,56,95,340-347], Green et al[76,92,348] West et al[77,90,91], Aspuru-Guzik et al[78,349-352] and Habershon et al[93,94]. The one advantage of ZStruct [97] and CGen over these other methods is the added convenience of being coupled to SE-GSM[109], which is generally a reliable method for finding reaction pathways, although it is not fools proof and finding reaction pathways can still remain a challenge in some cases.

Despite the success of these methods in exploring a variety of chemical reactions[99-110], including those discussed in the work above, areas for improvement still exist both in terms of creating more accurate models as well as in data analysis. With regards to creating more accurate models, improvements that are still needed to capture experimental details include:

(I) Automated assessment of solvation models to compare potential solvents implicitly and determine if explicit solvent modeling is necessary.

(II) Integration between ZStruct and QM/MM methods to model reactions in large systems (e.g. reactions involving enzymes or MOFs).

(III) Automated sampling of metal complexes with open coordination sites filled by any reagents used experimentally.

(IV) Further ZStruct development to handle multiple catalysts (i.e. multiple transition metal centers) that could be involved in a reaction mechanism.

(V) Systematic spin multiplicity or oxidation state sampling for transition metal catalyzed reactions

With these additional developments it would allow for automated reaction discovery to give insight into how experimental conditions (e.g. solvent) impact product formation. For instance, swapping solvents experimentally is known to have the potential to completely change the outcome of a reaction.[353-356] If computational models are to capture these effects then models need to be able to assess whether implicit or explicit solvent interactions are responsible for the reactivity differences. If explicit effects are deemed important then computational models need to be able to simulate how solvent interacts with the chemical system of interest to

potentially alter the reaction mechanism. This could be done with QM through the automated generation of a solvation shell, involving only a handful of solvent molecules, to better capture experimental conditions. However, in some cases this may not be enough to capture important energetic or mechanistic details, so instead integration of ZStruct with QM/MM methods may be necessary to capture solvent interactions.

In addition to making it possible for ZStruct to work with bulk solvent, the integration of ZStruct with QM/MM methods would also allow for reactions in large systems (e.g. MOFs and enzymes) to be modeled in a systematic way opening the doors to reaction discovery in a broader array of fields including biochemical transformations and hydrogen storage processes.

Another area where these methods could use improvement is with systematic, sampling of coordination complexes when multiple reagents have the potential to coordinate to a metal center. The current methods (i.e. ZStruct and CGen) are good for looking at how a single reagent interacts with a catalyst system, as shown in **Chapter V**. However, if an experimentalist provided a list of potential reagents it would be useful to be able to run through the list, generate all potential coordination complexes, assess their relative energies, and search for thermodynamic sinks that could impede reactivity prior to any experiments being ran.

Additionally, in transition metal catalyzed reactions changes in metal-L (L = any reagent that can coordinate to the metal center) complexes can lead to oxidation state and spin state changes that need to be modeled correctly, if computations have any hope of matching experiment. The ability to automate the generation of various spin states and oxidation states of metal complexes to see which states are favored would ensure that the correct species are being studied, as the wrong choice in oxidation or spin state leads to models that are of no relevance to experiment.

Lastly, the ability to account for multiple transition metals reacting together need to be developed further as ZStruct is currently not optimized to handle bimetallic reactions, which limits the types of chemistry that can be explored, and hinders the ability to search for off-cycle pathways. For instance, the identification of pathways that lead to off cycle dimer formation would be neglected currently with ZStruct unless they were specifically searched for by hand.

The further development of automated reaction discovery tools to fill in these gaps will expand the types of reactions that can be explored with methods like ZStruct, however, the other problem of large-scale data analysis in order to draw chemically relevant conclusions would still persist.

To tackle the processing of data analysis for automated reaction discovery methods improvements in the following areas are needed:

(I) Delineation of potential intermediates within a given number of elementary steps from known structures.

(II) Low cost ranking of possible reaction pathways to determine which ones are kinetically feasible prior to refining energetics with higher level quantum chemical calculations

(III) More robust techniques for assessing relationships between structural features and energetics, especially in the case of conformational searches

(IV) Streamlined processes for setting up calculations, analyzing reaction pathways, and condensing the results into chemically relevant information that can be used to inform experiment (e.g. reaction graph networks).

(V) Streamlined process for applying the results of reaction discovery to other similar chemical systems where reaction pathways are expected to be similar.

The delineation of potential intermediates could be done through the generation of reaction graph networks, which connect intermediates to one another based on the elementary steps identified with ZStruct. Through the use of Chemdraw or other imaging tools such as VMD the generation of visible networks would allow for concise explanations of potential reaction pathways to be described in detail and shared with collaborators. If reaction network generation could be combined with the use of partition functions (as demonstrated in **Chapters IV** and **V**) to determine probable pathways, they could be highlighted on the reaction network so that it would be clear as to what intermediates, products, and pathways are predicted to be probable. The highlighting of chemically relevant pathways would allow for experimentalists to design their

reaction conditions in ways that avoid pathways to undesired products, while also allowing for the verification of computationally probable pathways through experimental attempts to isolate key intermediates noted by computation.

In addition to partition functions being used to highlight important pathways within a reaction network, they could also be used to categorize initial or TS structures into high and low probability groups. This categorization would allow for structural or chemical differences between the sets of structures to be determined that could then be used to better understand what physical or chemical factors impact reactivity.

In order to help determine the chemical or structural features of high probability structures, methods that can automatically calculate and compare features (e.g. internal coordinates, molecular orbitals, atom charges etc.) would be useful and allow for fast and easy analysis as to why certain pathways are more favorable. A tool like this could allow for the identification of specific electronic or steric factors that could be contributing to differences in rates and selectivity observed experimentally for different substrates, catalysts, or additional reagents. Ultimately, the identification of important features that lead to high probability pathways could be used as a guide to generate TS guesses or improve driving coordinates for future reaction path searches in similar chemical systems. Additionally, the insight gained the analysis of probable pathways could help to guide the experimental development of future catalysts and/or chemical reactions.

Some groups have begun to work on developing ways to handle some of these processes. For instance, Reiher and co-workers have a reaction discovery method that streamlines the process of analyzing pathways generated by printing out reaction networks of the various elementary steps found.[95] However the development of more generalized procedures that could be applied to both ZStruct and CGen simultaneously would be helpful in processing the large amount of data that can be generated by these methods, as the ability to process and share data with collaborators is ultimately what makes these methods useful.

Overall, the current state of automated reaction discovery as described in this work allows computational chemists to explore main group and transition metal catalyzed reactions to understand complex mechanisms and study the interactions between reactants, catalysts and

additional reagents. Ultimately these methods still leave areas of chemical space hidden from exploration, but with improved methods for creating models and processing data searchable chemical space will continue to expand, as computational models are more accurately depict experimental conditions. This ability will lead to a new paradigm between computation and experiment, where computational models are to not only used to understand rates and selectivity of reactions, but also are used to explore new chemical systems, discover novel reaction mechanisms, and guide experimental design through predicting chemical reactivity**.**

APPENDIX A

Computational Details for Chapter II:

Automated Tools for Reaction Discovery

A.1 Computational Details of ZStruct reaction path generation for cisplatin-catalyzed methane activation

Reaction path exploration of cisplatin-catalyzed methane activation was done using ZStruct[97] and the single-ended Growing string method[109], developed within the Zimmerman Group. All geometries for initial structures, reaction paths, transition states and intermediates were obtained using density functional theory (DFT) in the Q-Chem 4.3 quantum chemistry package.[289] Restricted B3LYP[290-292] with a singlet spin and LANL2TZ(f) basis set and corresponding effective core potentials[357-359] on Pt, and the Pople 6-311++G** basis set [293,360] on all main group elements was used for optimization and reaction path generation using the single-ended Growing string method, from which all intermediates, reaction paths and transition state structures were obtained.

A.2 Computational Details of Ni(II)-catalyzed β-H elimination versus ligand swap mechanisms

Investigation of the β-hydride elimination pathways was done using the single-ended Growing string method.[109] All initial geometries for intermediates and transition states were obtained using density functional theory (DFT) in the Q-Chem 4.3 quantum chemistry package.[289] Restricted B3LYP-D3[290-292,361] with a singlet spin and LANL2DZ basis set and corresponding effective core potentials[293,356,362] was used for optimization and frequency calculations. Energies for initial geometries, intermediates and transition states were refined by applying the ωB97X density functional,[27] the cc-pVTZ basis sets, [363-366] and the SMD implicit solvent model, with THF as the chosen solvent, [297-299] using the ORCA quantum chemistry package. [300] All energies listed

are Gibbs free energies with enthalpy and entropy corrections, and all geometries were confirmed to have the appropriate number of imaginary frequencies.

Thermodynamic corrections to the enthalpy (H) and gas- phase entropy (S(g)) under catalytic conditions (298.15 K, 1 atm) were computed for all structures. To avoid inaccuracies inherent in the harmonic oscillator approximation, corrections for enthalpies and entropies were calculated by replacing low frequencies (<50 cm^{-1}) with 50 cm^{-1}. Solvent-based enthalpies H(l) were derived by adding thermal corrections for the enthalpies to the corresponding solution-phase total energies E(l). Energies reported in this article are therefore solvent-phase Gibbs free energies $G_{T\Delta S}$(l) at 1 atm and 298 K.

All intermediates and transition states were confirmed to have the appropriate number of imaginary frequencies, unless otherwise noted. All geometry optimizations, frequency calculations, and single point calculations were performed with an SCF convergence of 10^{-6}.

APPENDIX B

Supporting Information for Chapter III:

Simulated Mechanism for Palladium-Catalyzed, Directed γ-Arylation of Piperidine

B.1 Computational details for Pd(II/IV)-catalyzed piperidine arylation

Reaction discovery tools, ZStruct,[97] described in Chapter II, were used to determine the catalytic cycle that results in γ-arylated piperidine. Most quantum chemical simulations were performed using DFT in the Q-Chem 4.3 quantum chemistry pack.[289] Restricted B3LYP[290-292] with a singlet spin and LANL2DZ basis set[357-359-362] was used for optimization, frequency and natural bonding orbital analysis calculations. Reported charges were obtained from the natural bond orbital analysis calculations.[367] Restricted ω-B97X-D[27]with singlet spin and the 6-311++G** basis set[293,356] on main group elements, LANL2TZ(f) with an ECP on Pd and uncontracted LANL2DZ with an ECP[357-359] on Cs and iodine were used to calculate energies with the SMD solvation model[297-299] on the structures obtained from gas phase reaction path searches and optimizations. The SMD computations used tert-butanol as the implicit solvent via the GAMESS quantum chemistry package.[368,369] Thermodynamic corrections to the enthalpy, H, and gas phase entropy, $S_{(g)}$, at catalytic conditions (413 K, 1 atm) were computed for all structures.

To avoid inaccuracies inherent in the harmonic oscillator approximation, corrections for enthalpies and entropies were calculated by replacing low frequencies (< 50 cm^{-1}) with 50 cm^{-1}. Solvent-based enthalpies $H_{(l)}$ were derived by adding thermal corrections for the enthalpies to the corresponding solution phase total energies ($E_{(l)}$). Considering the significant quenching of rotational and translational degrees of freedom in the solvent phase[301-304] entropies ($S_{(l)}$) were derived by scaling the gas-phase values $S_{(g)}$ by a factor of 0.5 to reduce the overestimation of entropies in the gas phase approximation. Energies reported for Pd-catalyzed piperidine arylation are therefore solvent-phase Gibbs free energies ($G_{0.5T\Delta S(l)}$) at 1 atm and 413 K.

B.2 Number of Gradients Used for GSM Optimization During Reaction Path Exploration

Table B1: Number of gradients used for GSM optimization steps during reaction path exploration for elementary steps connecting intermediates for piperidine arylation using the B3LYP functional with LANL2DZ on all elements with an ECP on Pd.

Elementary Step (Intermediates Connected)	Number of Gradients Used for GSM Optimization
2 to 3	429
3 to 4	501
4 to 5	212
5 to 7	516
4 to 6	1409
6 to 7	233
8 to 9	190
11 to 12	201
12 to 13	127
14 to 15	1842
16 to 17	1027

B.3 Alternative Reaction Pathways

B.3a. C-H Activation Including Free Acetic Acid

C-H activation beginning from **5s**, which includes free acetic acid, was explored to ensure that the free acetic acid does not participate in the C-H activation transition state. The overall pathway was identical to the C-H activation pathway starting from **5**. The same one-step process was found, involving piperidine isomerization from a chair to a boat conformation as the O of the κ^2-acetate ligand closest to C_γ-H dissociates from Pd. As the κ^2-acetate O dissociates, Pd facilitates the proton transfer from C_γ to the newly delegated O, **TS-5s-7s**, and then the newly formed OH group rotates out of the square plane of Pd to avoid steric interactions, **Figure B1**. This process results in intermediate **7s**, which is identical to **7**, in which Pd is bound to N_{DG}, N_{Pip}, C_γ and a κ^1acetic acid ligand, except that a free acetic acid molecule is present. The barrier to C-H activation is 36.0 kcal/mol, **TS-5s-7s**, and leads uphill 22.3 kcal/mol to **7s.**

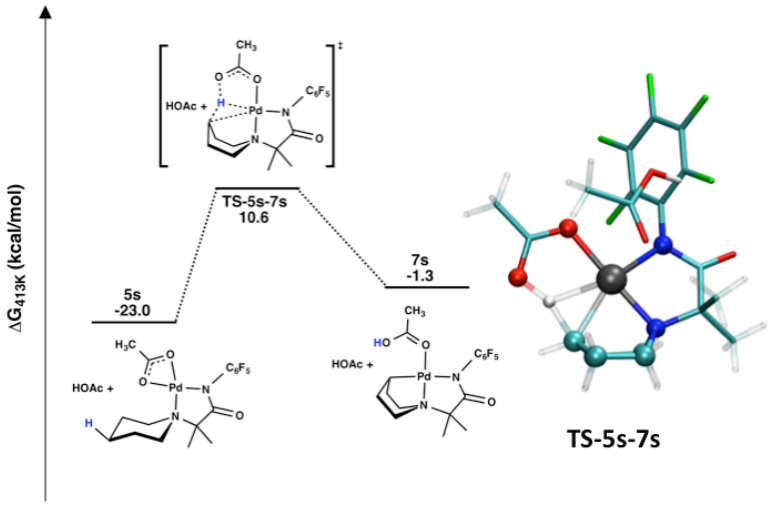

Figure B1: (Left) Alternative C-H activation pathway starting from **5s.** (Right) 3D rendering of **TS-5s-7s**. Energies are referenced to separate reactants (i.e. **1** from **Figure III.4,** main paper).

B.3b. *Two-step C-H Activation Pathway*

A two-step pathway for C-H activation involving a chair to boat isomerization followed by C-H activation from the boat intermediate was investigated, **Figure B2**. Starting from **5** the chair to boat isomerization can occur through **TS-5-5boat**, **Figure B2**, with a barrier of 11.6 kcal/mol. This leads to **5boat,** which still has Pd bound to a κ^2-acetate ligand, N_{DG}, and N_{Pip} with the piperidine ring in a twisted-boat conformation and is uphill 7.7 kcal/mol from **5**. The difference between **5** and **5boat** comes solely from the isomerization of the piperidine ring from a chair to twisted-boat conformation, which puts the γ-C-H bond in closer proximity to the Pd center. From **5boat** C-H activation is found to occur through a CMD mechanism in which a Pd-O bond closest to the γ–C-H bond breaks, allowing Pd to coordinate to the γ–carbon and hydrogen. This coordination enables Pd to facilitate the proton transfer to the newly un-ligated O. Once the proton transfer is complete the newly formed κ^1-acetic acid ligand rotates out of the square plane of the Pd to avoid steric interactions between the OH and the Pd- γ–carbon bond. The barrier to this step is 34.2 kcal/mol (**TS-5boat-7, Figure B2**) and results in **7**, which is uphill 23.8 kcal/mol from **5.**

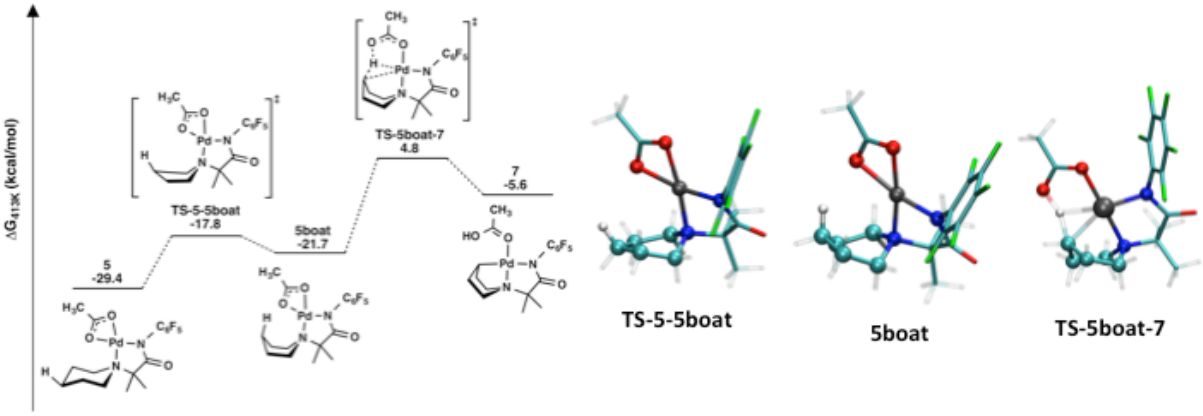

Figure B2: (Left) Alternative two-step C-H activation pathway starting from **5** leading to **7** through a boat intermediate, **5boat**. (Right) 3D renderings of **TS-5-5boat, 5boat, and TS-5boat-7** structures. Energies are referenced to separate reactants (i.e. **1** from **Figure III.4,** main paper).

B.3c. Comparison of Alpha, Beta and Gamma Carbon C-H Activation

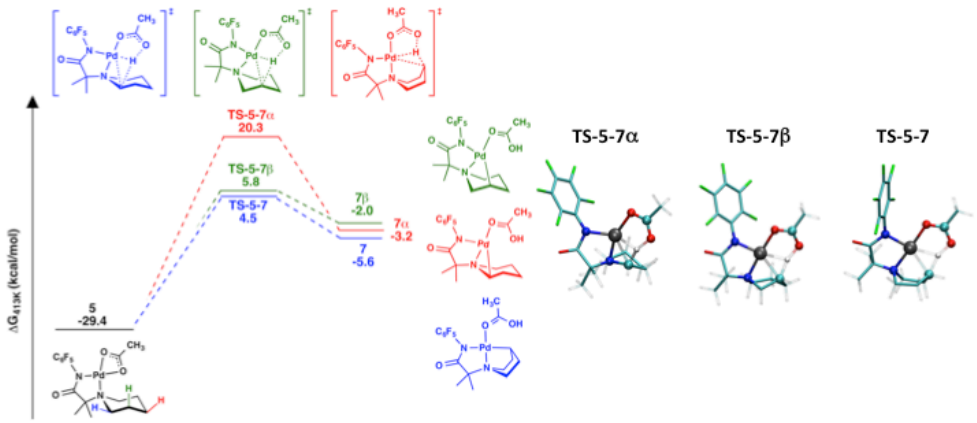

Figure B3: (Left) Pathways for α-, β-, and γ-carbon C-H activation. (Right) 3D renderings of **TS-5-7α, β, γ** structures. Energies are referenced to separate reactants (i.e. **1** from **Figure III.4,** main paper).

Mechanisms for C-H activation at the α-, β-, and γ-carbons have been compared to determine the kinetic difference in reactivity, **Figure B3**. From **5** C-H activation at each site can occur through a concerted metalation deprotonation mechanism where an O atom of the κ^2-acetate ligand on Pd dissociates and abstracts the proton from the carbon being activated. Activation of the α-carbon has the highest barrier of 49.7 kcal/mol through **TS-5-7α**. The α-activated intermediate, **7α**, is 2.4 kcal/mol higher in energy than the γ-activated intermediate, **7**.

The high activation barrier makes C-H activation at the α-carbon infeasible starting from **5**. In contrast, activation at the β-carbon has a barrier of 35.2 kcal/mol through **TS-5-7β**. This barrier is only 1.3 kcal/mol above that of γ-carbon activation, and the β-activated intermediate that forms, **7β**, is 3.6 kcal/mol higher in energy than the γ-activated intermediate, **7**. The activation barriers and difference in energy between activated intermediates supports the proposal that α- and β-carbon activation are unfavorable compared to γ-carbon activation from **5**.

B.3d. PhI Coordination: Pd-I vs Pd-π Complex Formation

From **7** PhI can coordinate to Pd through either iodine or the Ph group through the formation of a Pd-π-complex, **Figure B4**. The first pathway investigated leads to Pd-I coordination. This pathway begins with PhI addition to **7** leading downhill 2.1 kcal/mol to **8** through the addition of PhI to intermediate **7**. From **8** PhI coordination to Pd through iodine causes the displacement of acetic acid with a barrier of 8.5 kcal/mol from **7** through **TS-8-9** leading to intermediate **9,** which is 0.9 kcal/mol downhill from **7**.

Alternatively, the addition of PhI to **7** can also lead to **8a**, which is uphill 5.7 kcal/mol from **7**. From **8a** the Ph group can form a Pd-π complex, which also causes the displacement of acetic acid. This reaction has a barrier of 10.9 kcal/mol through **TS-8a-9a** leading to **9a**, which is uphill 3.7 kcal/mol from **7**. The 2.4 kcal/mol difference in activation barriers between these two pathways as well as the thermodynamic preference for Pd-I coordination over Pd-π complexation suggests that the Pd-I coordination pathway is operable rather than the Pd-π complex formation pathway. These results lead to further reaction path exploration only proceeding from **9**.

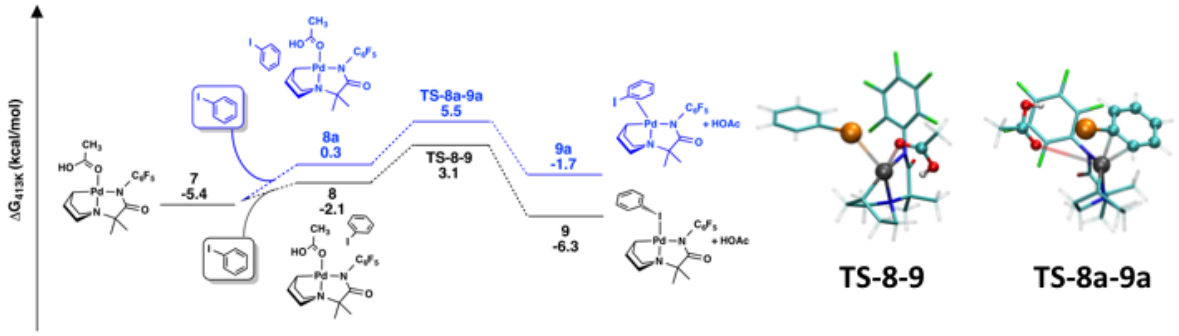

Figure B4: (Left) Reaction pathway for Pd-I coordination verses Pd-π complex formation. (Right) 3-D renderings of the transition state structures for Pd-I coordination, **TS-8-9**, and Pd-π complex formation, **TS-8a-9a**. Energies are referenced to separate reactants (i.e. **1** from **Figure III.4,** main paper).

B.3e. Oxidative Addition without CsOAc

From **9**, oxidative addition without CsOAc was examined. First, the removal of acetic acid from **9** leads to **10s,** which is downhill from **9** by 1.8 kcal/mol. From **10s** an oxidative addition pathway, shown in **Figure B5**, was found where Ph adds into the axial position on Pd *cis* to C_γ while iodine remains in the equatorial position, leading to **11s** through **TS-10s-11s**. The barrier for this pathway is 19.1 kcal/mol above **10s**, but 40.4 kcal/mol above **5** (**Figure III.4**), which is the lowest energy intermediate prior to this step. This makes oxidative addition to form the high valent Pd(IV) intermediate energetically infeasible without CsOAc. Intermediate **11s** is 3.0 kcal/mol downhill from **10s** and has square pyramidal Pd(IV) center bound to C_γ, C_{Ph}, iodine, N_{DG} and N_{Pip}. This structure is identical to intermediate **12**, from **Figure III.10**, which forms through oxidative addition after acetic acid sequestration by Cs-acetate.

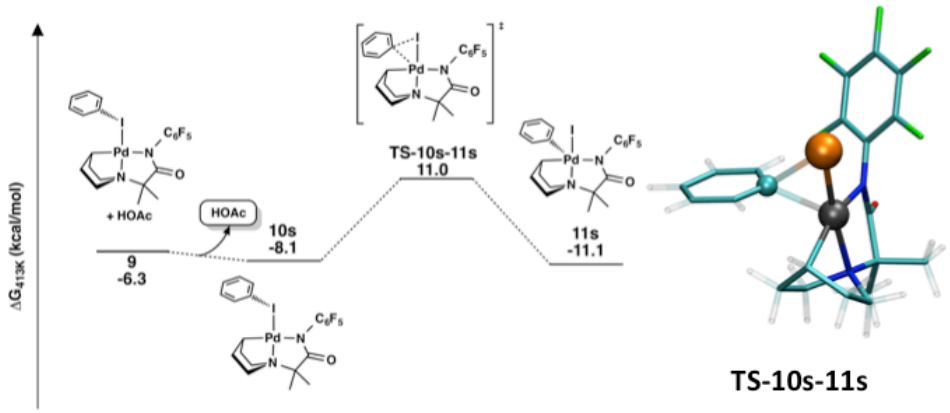

Figure B5: (Left) Oxidative addition pathway without acetic acid sequestration. (Right) 3D structure of the oxidative addition transition state **TS-10s-11s**. Energies are referenced to separate reactants (i.e. **1** from **Figure III.4,** main paper).

B.3f. Oxidative Addition and Reductive Elimination with Acetate or Acetic Acid Coordinated to Pd

Additional coordination of acetate or acetic acid to Pd prior to or following oxidative addition can result in 4 structures (**11-OAc, 11-OAcH, 12-OAc, 12-OAcH** in **Figure B6**) where the additional ligand is bound to Pd in addition to the aryl-iodide. From these four structures only **12-OAc** lead to a stable structure where the additional acetate ligand remained bound to Pd. From **12-OAc** the pathway for reductive elimination was investigated, **Figure B7**. Reductive elimination from **12-OAc** was found to have a barrier of 32.1 kcal/mol, 63.3 kcal/mol above the lowest energy intermediate, **5**, prior to this step. The barrier makes reductive elimination from **12-OAc** an energetically infeasible pathway.

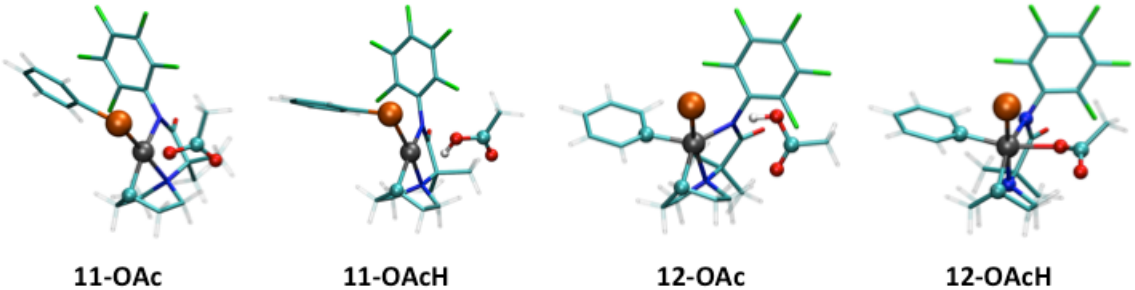

Figure B6: Optimized structures for pre and post oxidative addition intermediates with acetate or acetic acid coordinated to Pd.

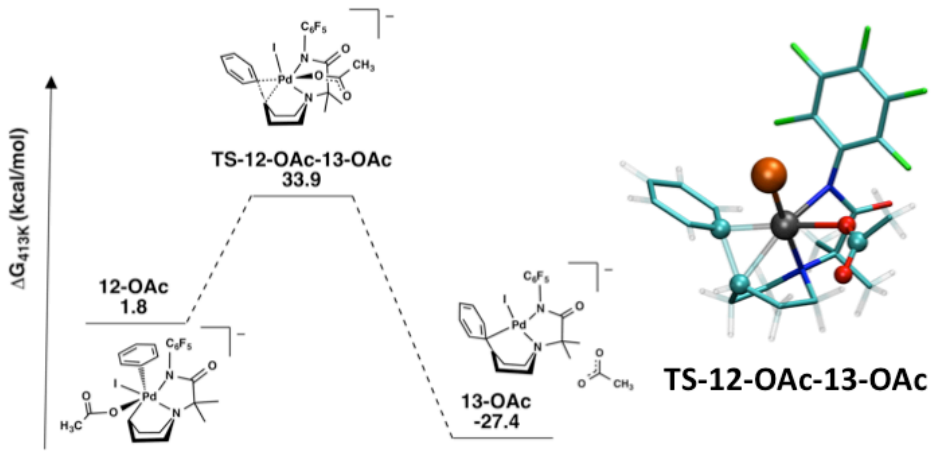

Figure B7: (Left) Reaction pathway for reductive elimination from **12-OAc**. (Right) 3D rendering of **TS-12-OAc-13-OAc.** Energies are referenced to separate reactants (i.e. **1** from **Figure III.4,** main paper).

B.3g. Acetic Acid Assisted Iodine Abstraction Without Cesium

Iodine abstraction with acetic acid assistance, but without the inclusion of a Cs cation, was investigated to assess the importance of the Cs cation in making iodine abstraction energetically feasible. Starting from **16**, acetic acid-assisted iodine abstraction can occur in the two-step process shown in **Figure B8**. First, acetic acid must replace Cs-OAcH, leading from **16** uphill 26.7 kcal/mol to **16s1**, immediately making this pathway energetically unfavorable. From **16s1** a ligand swap reaction between acetic acid and iodine can occur through **TS-16s1-17s1** with a barrier of 49.9 kcal/mol above **16** to form **17s1**, which is uphill 35.7 kcal/mol from **16**. This pathway leads to a free iodine anion and a square planar Pd center bound to κ^1-acetic acid, κ^1-acetate, N_{DG}, and $N_{Pip.}$ The high energy profile indicates the importance of having the Cs cation participate in iodine abstraction, so that it can coordinate to the iodine anion and generate CsI.

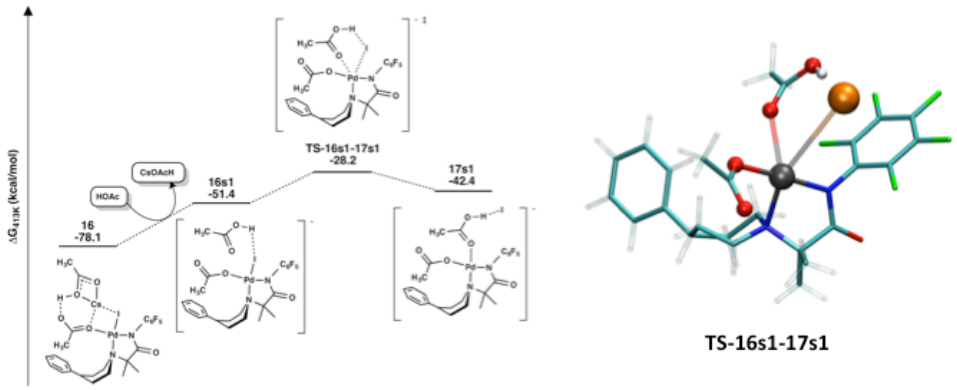

Figure B8: (Left) Iodine abstraction pathway without the Cs cation but with HOAc rebinding to Pd. (Right) 3D structure of the iodine abstraction transition state **TS-16s1-17s1**. Energies are referenced to separate reactants (i.e. **1** from **Figure III.4**).

B.3h. Iodine Abstraction without Cs-OAcH

Iodine abstraction without the assistance of Cs-OAcH was investigated to determine its effect on the barrier to iodine abstraction. Without the assistance of Cs-OAcH, iodine abstraction can occur in through a single ligand swap step (**Figure B9**) where the free O of the κ^1-acetate ligand rebinds to Pd, forcing iodine to dissociate from the metal center through **TS-16s2-17s2**. Without the presence of the Cs cation the iodine anion is left without a counter ion, which ultimately increases the energy of this step. The initial removal of Cs-OAcH from **16** leads uphill 14.5 kcal/mol to **16s2**. From **16s2** the barrier to form **17s2** is 28.6 kcal/mol above **16** through **TS-16s2-17s2**, which makes it feasible, but unlikely to occur in competition with the pathway leading from **16** to **17** through **TS-16-17** (**Figure III.16**), which has a barrier of 17.7 kcal/mol above **16** (**TS-16-17, Figure III.17**). The high energy for these steps helps establish the importance of having the Cs cation participate in iodine abstraction.

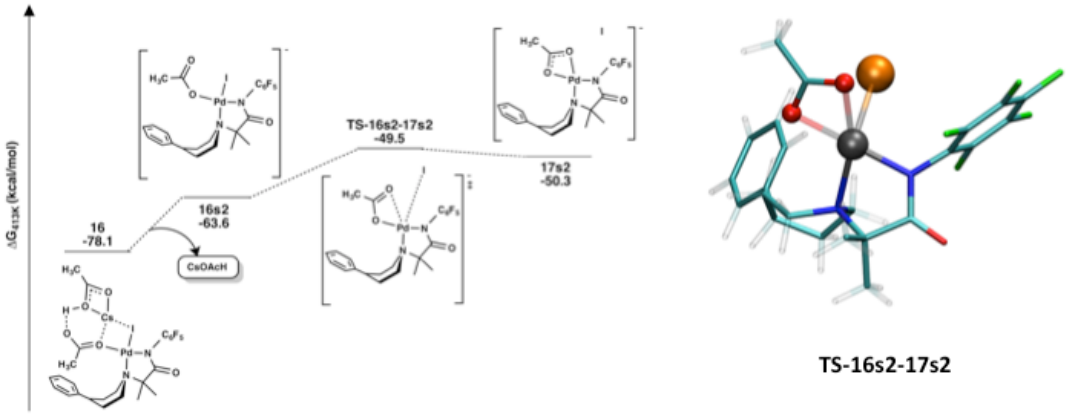

Figure B9: (Left) Iodine abstraction pathway without any additives. (Right) 3D structure of the iodine abstraction transition state **TS-16s2-17s2**. Energies are referenced to separate reactants (i.e. **1** from **Figure III.4**).

B.4 Natural Bond Orbital Data for N_{DG},N_{Pip} versus O_{DG},N_{Pip} Coordination to Pd

Table B2: Natural Bond Orbital Analysis for Pd coordinated to either N_{DG},N_{Pip} or O_{DG},N_{Pip}. All contributions are %s.

Bond	Atom	AO Contribution	s-Orbital Contribution	p-Orbital Contribution	d-Orbital Contribution
N_{DG}-Pd	N_{DG}	72.47	19.67	80.33	0.00
	Pd	27.53	9.73	0.06	90.21
O_{DG}-Pd	O_{DG}	83.17	8.92	91.08	0.00
	Pd	16.83	45.18	0.70	54.12

The thermodynamic difference of 15.7 kcal/mol favoring Pd-N_{DG},N_{Pip} coordination over Pd-O_{DG},N_{Pip} coordination can be further explained by the bonding differences between N_{DG}-Pd and O_{DG}-Pd, **Table B2**. The N_{DG}-Pd bond is composed of more even contributions from the N_{DG} and Pd orbitals (72.47% and 27.53% respectively) in comparison to the O_{DG}-Pd bond (83.17% O_{DG} and 16.83% Pd). In addition, the p-d orbital overlap differences between N_{DG} and O_{DG} coordinated to Pd could further explain the greater stability of Pd-N_{DG},N_{Pip} coordination. The N_{DG}-Pd bond is composed of 19.67% N_{DG} s-orbital and 80.33% N_{DG} p-orbital interacting with 9.73% Pd s-orbital and 90.21% Pd d-orbital interactions. In contrast, the O_{DG}-Pd bond is composed of 8.29% O_{DG} s-orbital and 91.08% O_{DG} p-orbital interactions with 45.18% Pd s-orbital, 0.70% Pd p-orbital and 54.12% Pd d-orbital interactions. The greater involvement of Pd orbitals in the N_{DG}-Pd bond and

the significant reduction in p-d orbital overlap between O_{DG} and Pd in comparison to N_{DG} and Pd can explain the greater stability of the N_{DG},N_{Pip} chelation mode.

B.5 Dispersion Correction Impact on C-H Activation Energetics and Structures

To check the reliability of the B3LYP functional for optimizations and reaction path exploration single point energies using three other functionals were examined in the C-H activation step for the model system and the real system (intermediates **5, TS-5-7**, **7, 5'**, **TS-5'-7'**, **7'**). Specifically PBE[370,371], B3LYP[290-292], ωB97X-D[27], and M06-2X[372]. were used to run gas-phase and solvent corrected single point energy calculations for the C-H activation intermediates. Similar energetics were expected from B3LYP, M06-2X and ωB97X-D functionals but an underestimated activation barrier with the GGA functional, PBE. In addition, these same C-H activation intermediates and transition states have been optimized using B3LYP and ωB97X-D to see how dispersion corrections effect optimizations.

B.5a Gas- and Solvent-Phase Energies

The energies of the C-H activation intermediates and transition state for the model system (**5**, **TS-5-7**), and the real system (**7**, **5'**, **TS-5'-7',** and **7'**) were calculated using the PBE[366,367], B3LYP[290-292], M06-2X[368] and ωB97X-D[27] density functionals with the LANL2TZ(f) basis set and ECP on Pd and 6-311++G**[293,356] basis set on all main group elements in both the gas- and solvent-phase, and the results can be found in **Tables B3, B4, B5**, and **B6**. The activation barriers for C-H activation were found to be within 1 kcal/mol of one another using B3LYP, M06-2X and ωB97X-D, with barriers between 38.1-39.1 kcal/mol for the model system and 38.2-39.4 kcal/mol for the real system, respectively, in the gas-phase. In the solvent phase, the barriers were still within 1 kcal/mol, ranging from 37.1-38.0 kcal/mol in the model system and 36.8-37.9 kcal/mol in the real system. As expected, the PBE functional underestimated the barriers for the model and real system in the gas-phase at 31.2 and 31.9 kcal/mol and the solvent-phase barriers at 30.0 and 30.2 kcal/mol. This shows that the use of a dispersion corrected functional (ωB97X-D[27]) versus a non-dispersion corrected functional (B3LYP) has little impact on calculating the activation barrier for the reaction.

In addition, the thermodynamics of the reaction were also found to have little variance with respect to the functional chosen, as the energy of reaction for the model and real system ranged from 22.7-26.1 kcal/mol and 20.3-23.7 kcal/mol, respectively, in the gas-phase. Similarly, the solvent phase thermodynamics of the reaction were 21.1-24.6 kcal/mol and 18.4-22.0 kcal/mol for the model and real system, respectively.

Table B3: Gas phase enthalpies of the structures 5, TS-5-7, and 7 using various functionals. LANL2TZ(f) basis set with LANL2TZ(f) ECP was used on Pd, while 6-311++G** was used on all main group elements.

Functional	5 (Hartrees)	TS-5-7 (Hartrees)	7 (Hartrees)	E_a (kcal/mol)	E_{rxn} (kcal/mol)
PBE	-1619.184644	-1619.13501	-1619.148423	31.2	22.7
B3LYP	-1620.839231	-1620.77833	-1620.797674	38.2	26.1
ωB97X-D	-1620.368434	1620.307773	-1620.327864	38.1	25.5
M06-2X	-1620.157362	-1620.095131	-1620.119208	39.1	24.0

Table B4: Gas phase enthalpies of the structures 5', TS-5'-7', and 7' using various functionals. LANL2TZ(f) basis set with LANL2TZ(f) ECP was used on Pd, while 6-311++G** was used on all main group elements.

Functional	5' (Hartrees)	TS-5'-7' (Hartrees)	7' (Hartrees)	E_a (kcal/mol)	E_{rxn} (kcal/mol)
PBE	-1974.641696	-1974.590826	-1974.609394	31.9	20.3
B3LYP	-1976.691449	-1976.628646	-1976.653669	39.4	23.7
ωB97X-D	-1976.125353	-1976.063768	-1976.089155	38.7	22.7
M06-2X	-1975.881549	-1975.819552	-1975.84816	38.9	21.0

Table B5: Solvated enthalpies of the structures 5, TS-5-7, and 7 using various functionals. LANL2TZ(f) basis set with LANL2TZ(f) ECP was used on Pd, while 6-311++G** was used on all main group elements.

Functional	5 (Hartrees)	TS-5-7 (Hartrees)	7 (Hartrees)	E_a (kcal/mol)	E_{rxn} (kcal/mol)
PBE	-1619.2302537	-1619.1824004	-1619.1966954	30.0	21.1
B3LYP	-1620.0578100	-1619.9986559	-1620.0186513	37.1	24.6
ωB97X-D	-1620.420491	-1620.361419	-1620.382578	37.1	23.8
M062X	-1620.200299	-1620.139672	-1620.164763	38.0	22.3

Table B6: Solvated enthalpies of the structures 5', TS-5'-7', and 7' using various functionals. LANL2TZ(f) basis set with LANL2TZ(f) ECP was used on Pd, while 6-311++G** was used on all main group elements.

Functional	5' (Hartrees)	TS-5'-7' (Hartrees)	7' (Hartrees)	E_a (kcal/mol)	E_{rxn} (kcal/mol)
PBE	-1974.692773	-1974.644594	-1974.663399	30.2	18.4
B3LYP	-1975.736102	-1975.675712	-1975.701069	37.9	22.0
ωB97X-D	-1976.180376	-1976.121733	-1976.147466	36.8	20.7
M062X	-1975.928218	-1975.868213	-1975.897928	37.7	19.0

B.5b Optimized Structures, Key Bond Lengths and Energies

The structures of C-H activation intermediates and transition state for the model system (**5**, **TS-5-7**), and the real system (**7**, **5'**, **TS-5'-7'**, and **7'**) were optimized using the B3LYP and ωB97X-D density functionals with the LANL2DZ basis set and ECP on all elements. The structures can be found in **Figure B10** and **B11** and the key bond lengths and energies can be found in **Tables B7**, **B8**, **B9**, and **B10**. The use of a dispersion versus non-dispersion corrected functional appeared to have little impact on the structure optimization for the rate-limiting C-H activation intermediates and transition states in the model and real system. In addition, changing the functional did not change the key features of the transition state structures **TS-5-7** and **TS-5'-7'**, which involve proton transfer from carbon to oxygen facilitated by Pd.

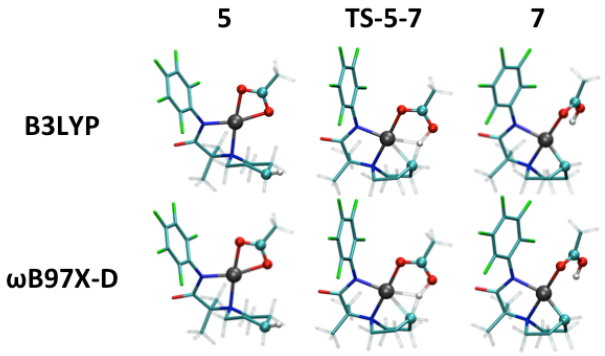

Figure B10: 3D renderings of optimized structures for **5, TS-5-7,** and **7** using B3LYP and ω97X-D.

Table B7: Key bond lengths in Å for gas phase optimized structures of **5, TS-5-7,** and **7** using B3LYP and ωB97X-D with LANL2DZ basis set on all atoms and the LANL2DZ ECP on Pd. All bond lengths are in Å.

Key Bond Length	Functional	5	TS-5-7	7
Pd-C	B3LYP	4.006	2.300	2.085
	ωB97X-D	3.958	2.257	2.067
Pd-O	B3LYP	2.198	2.961	3.142
	ωB97X-D	2.182	2.930	3.178
C-H	B3LYP	1.096	1.486	3.344
	ωB97X-D	1.094	1.477	3.109
O-H	B3LYP	4.200	1.277	0.997
	ωB97X-D	4.142	1.273	0.987

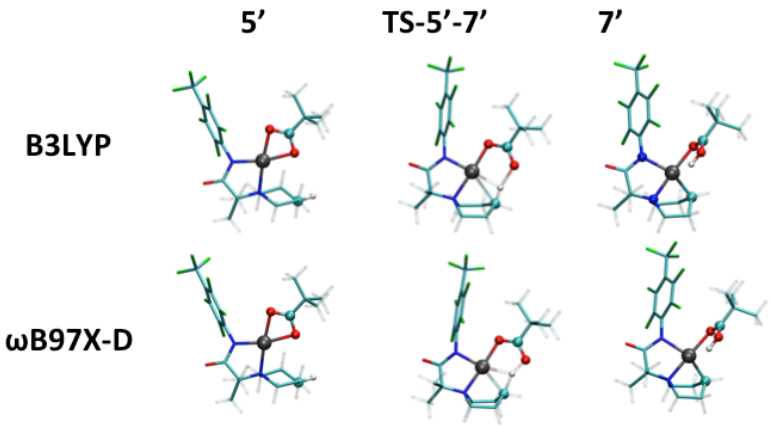

Figure B11: 3D renderings of optimized structures for **5’, TS-5’-7’, 7’** using B3LYP and ωB97X-D.

Table B8: Key bond lengths for gas phase optimized structures of **5’, TS-5’-7’,** and **7’** using B3LYP and ωB97X-D with LANL2DZ basis set on all atoms and the LANL2DZ ECP on Pd. All bond lengths are in Å.

Key Bond Length	Functional	5’	TS-5’-7’	7’
Pd-C	**B3LYP**	4.016	2.28706	2.084
	ωB97X-D	3.966	2.250	2.062
Pd-O	**B3LYP**	2.176	2.94597	3.127
	ωB97X-D	1.094	1.462	3.323
C-H	**B3LYP**	1.096	1.47219	3.418
	ωB97X-D	1.094	1.462	3.323
O-H	**B3LYP**	4.167	1.29960	0.996
	ωB97X-D	4.109	1.290	0.988

The gas phase energies of the optimized structures for C-H activation leads to the same conclusion as above: the functional has little impact on the activation barrier and energy of reaction found for the C-H activation step, even when using a smaller basis set, LANL2DZ with ECP on Pd. The activation barriers for the real and model system were found to be 38.4 and 37.4 kcal/mol using B3LYP and 37.7 and 35.6 kcal/mol using ωB97X-D. The energy of reaction for the optimized structures were found to be 28.8 and 26.0 kcal/mol using B3LYP and 27.7 and 24.4 kcal/mol using ωB97X-D respectively.

Table B9: Gas-phase enthalpies of the re-optimized structures of 5, TS-5-7, 7 using B3LYP and ωB97X-D with LANL2DZ basis set on all atoms and the LANL2DZ ECP on Pd.

Functional	5 (Hartrees)	TS-5-7 (Hartrees)	7 (Hartrees)	E_a (kcal/mol)	E_{rxn} (kcal/mol)
B3LYP	-1620.009124	-1619.948006	-1619.963306	38.4	28.8
ωB97X-D	-1619.562935	-1619.502937	-1619.518833	37.7	27.7

Table B10: Gas-phase enthalpies of the re-optimized structures of 5', TS-5'-7', 7' using B3LYP and ωB97X-D with the LANL2DZ basis set on all elements and LANL2DZ ECP for Pd.

Functional	5' (Hartrees)	TS-5'-7' (Hartrees)	7' (Hartrees)	E_a (kcal/mol)	E_{rxn} (kcal/mol)
B3LYP	-1975.674782	-1975.615109	-1975.633434	37.4	26.0
ωB97X-D	-1975.139256	-1975.0826	-1975.100383	35.6	24.4

Table B11: Bond lengths during C-H Activation. C-H and O-H bond lengths featured in **Figure III.8** and **Figure III.9** of the main text for the conversion from **5** to **7** through **TS-5-7**. All bond lengths are in Å.

Atom Dist.	5	5-7a	5-7b	5-7c	5-7d	5-7e	5-7f	TS-5-7	5-7g	5-7h	7
C-H	1.10	1.10	1.10	1.09	1.09	1.09	1.14	1.49	2.22	2.77	3.33
O-H	4.20	3.65	3.12	2.67	2.36	2.19	1.97	1.28	1.01	1.00	1.00

Table B12: Bond lengths during C-H Activation. Pd-C and Pd-O bond lengths features in **Figure III.8** and **Figure III.9** of the main text for the conversion of **5** to **7** through **TS-5-7**. All bond lengths are in Å.

Atom Dist.	5	5-7a	5-7b	5-7c	5-7d	5-7e	5-7f	TS-5-7	5-7g	5-7h	7
Pd-C	4.01	3.81	3.62	3.44	3.30	3.05	2.59	2.28	2.14	2.10	2.09
Pd-H	2.20	2.20	2.20	2.20	2.22	2.46	2.90	2.94	3.13	3.17	3.15

B.6 Energetic Differences Between High and Low Spin States for Intermediates 15 and 16

Table B13: Energies for structures **15** and **16** in the singlet (low spin) and triplet (high spin) states, and their energies referenced to the lowest energy structure. [a]Energies reported are enthalpies calculated in the gas phase enthalpies[3]. [b]Energies are Gibbs free energies calculated in solvent[4,5]

Geometry (structure)	Spin State	Energy (Hartrees)	ΔE (kcal/mol)
Square Planar (16)[a]	singlet	-2111.438676	0.0
Square Planar (16)[a]	triplet	-2111.371125	42.4
Tetrahedral (15)[a]	singlet	-2111.397954	25.6
Tetrahedral (15)[a]	triplet	-2111.365756	45.8
Square Planar (16)[b]	singlet	-2111.531667	0.0
Tetrahedral (15)[b]	singlet	-2111.496421	22.1

The barrierless isomerization of structure **15** to structure **16** can be attributed to the thermodynamic stability of the singlet square planar complex in comparison to the singlet tetrahedral complex, which lies 25.6 kcal/mol uphill in energy. This stability is extended to the difference in energy between the singlet at triplet states of the square planar and tetrahedral

complexes in which the square planar singlet complex lies 42.4 and 45.8 kcal/mol downhill in energy from the triplet square planar and tetrahedral complexes respectively, **Table S13**.

Solvent, and frequency corrections are shown to have minimal impact on changing the energetics between the singlet square planar and tetrahedral complexes in comparison to the gas phase. The smaller energetic difference between the square planar and tetrahedral complexes **15** and **16** are expected to translate to the differences in energy between the singlet and triplet states, as evident in the gas phase energies. Overall the singlet square planar state is the lowest energy state, and the thermodynamic difference in energy between the varying spin states and geometries suggests that only the square planar singlet structure should exist in-situ.

B.7 Solvated Entropy Corrections

Method for calculating reaction free energies

The gas phase entropy is given by

$$-S(g) = ((G(g)-H(g))/T) \text{ where } G(g) = E(g) + G_{corr} \text{ and } H(g) = E(g) + H_{corr}$$

For solvent phase entities entropy S(l) is derived by scaling the gas phase entropy S(g) by a factor of 0.5:

$$S(l) = 0.50 \times S(g)$$

$$G(l) = H(l) - TS(l) = E(l) + H_{corr} - 0.50 \times TS(g)$$

APPENDIX C

Supporting Information for Chapter III:

The Role of a Flexible Polymer in Olefin Chain Growth via Constrained Geometry Catalysts

C.1 Ti-$C_3H_7^+$ initial structure correlation

The energetic differences between the initial structures can be linearly correlated to the inverse of the distance (1/r) between the Ti-center and terminal carbon (C_3) of the $C_3H_7^+$ chain and the average of 1/r values between the C_2 carbon and Cp* ligand (R^2 = 0.72), **Figure C1**. This correlation leads to a linear regression with a slope of -144.98 for the Ti-C_3 interaction and +119.1 for the average C_2-Cp* interaction. The negative slope for 1/r for the Ti-C_3 distance indicates that closer Ti-alkyl interactions lead to more stable structures, this can likely be attributed to close Ti-alkyl proximity allowing for more stable η-2 coordination modes to form.

The opposing positive slope associated with the average C2-Cp* 1/r value indicates that as the polymer chain gets closer to the Cp* ligand, steric interactions raise the energy of the structure. The greater magnitude of the slope for 1/r of Ti-C_3 compared to 1/r for C_2-Cp* indicates that the electronic stabilizing effect of the alkyl chain being in close proximity to the Ti-center trumps the effect of the steric interactions on $\Delta G_{Initial}$

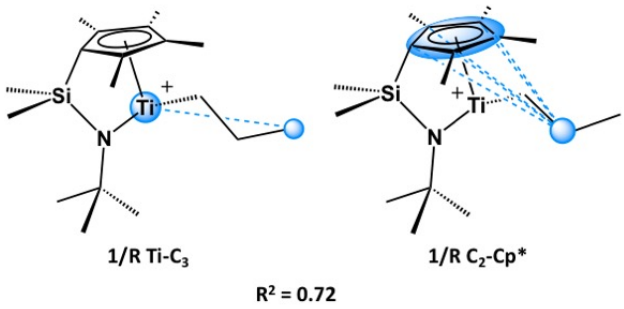

Figure C1: 2-D rendering of the 1/r values for Ti-C_3 and C_2-Cp* atom distances that correlate to $\Delta G_{Initial}$. C_2H_4 monomers have been omitted for clarity.

C.2 Ti-$C_5H_1^+$ initial structure and TS structure correlation

The differences in energy between the initial Ti-$C_5H_{11}^+$ structures could be linearly correlated to the 1/r value for the Ti-C_4 distance or Ti-C_5 distance combined with the sum of $1/r^6$ values for C_2-Cp* distances (R^2 = 0.55, 0.54 respectively), **Figure C2a and Figure C2b**. If these three features are combined then an increased correlation of R^2 = 0.59 is observed.

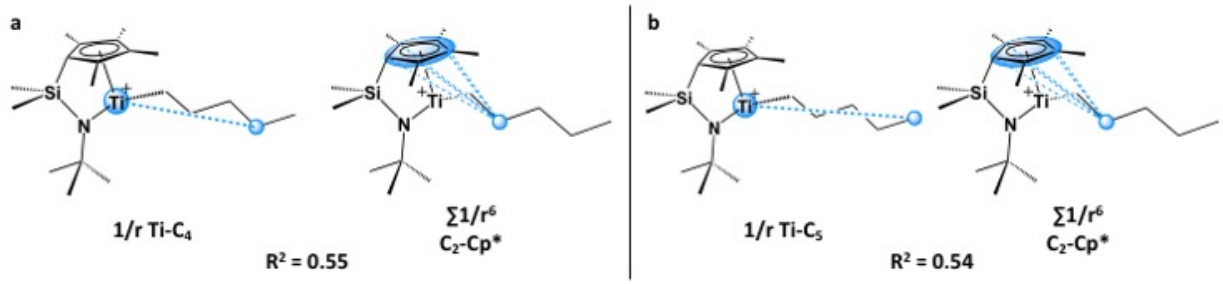

Figure C2: 2-D rendering of the structural features that correlate to $\Delta G_{Initial}$. (a) 1/r and $1/r^6$ values for the Ti-C_4 and C_2-Cp* atom distances. (b) 1/r and $1/r^6$ values for the Ti-C_5 and C_2-Cp* atom distances. C_2H_4 monomers have been omitted for clarity.

Seeing as the energy of the initial structure energy does not dictate the TS energy, investigations into what features of the various Ti-$C_5H_{11}^+$ conformers, if any, impact the activation barrier to monomer insertion were done. As was the case with the initial structures, no single structural feature describing the polymer chains interaction with the catalyst was found to correlate to ΔG_{TS} with an R^2 value greater than 0.5.

With two features moderate linear correlation (R^2 = 0.52) was found between $1/r^6$ for Ti-C_1 distances and the sum of $1/r^6$ values for Ti-Cp ring distances with ΔG_{TS}, **Figure C3a**. If the $1/r^6$ value for Ti-C_5 distance is included in the correlation then R^2 can be improved to 0.66, **Figure C3b**.

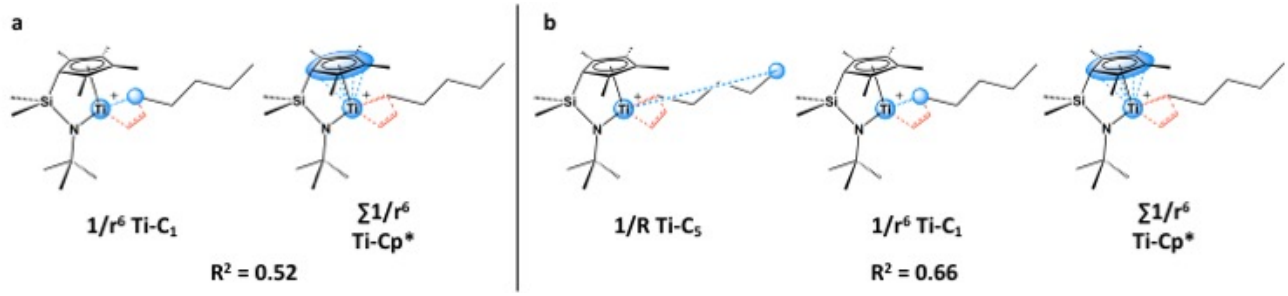

Figure C3: 2-D rendering of the structural features that correlate to ΔG_{TS}. (a) $1/r^6$ values for the Ti-C_1 and sum of $1/r^6$ values for Ti-Cp ring distances. (b) $1/r^6$ values for the Ti-C_1, Ti-C_5 and sum of $1/r^6$ values for the Ti-Cp ring distances.

The weak correlation with multiple features implies that with the larger polymer chain the TS energy, just like the initial structure, cannot be correlated to a set of structural features that have the same impact across all conformers. One thing to note though is that interactions between the terminal end of the polymer chain and Ti do appear as structural features that have weak linear correlation with the initial structure and TS energy, implying that the conformation does begin to impact energetics at least to a small degree.

APPENDIX D

Supporting Information for Chapter V:

Exploring Interactions between Counterions and Polymer Chains during Polyolefin Growth.

D.1 Energetics and Bond Distances for Monomer Insertion with Ti-$C_3H_7^+$ and Me-$B(C_6F_5)_3^-$

Table 1: Relative energies of Ti-$C_3H_7^+$ structures aligned with Me-$B(C_6F_5)_3^-$ and their respective TS structure energies for C_2H_4 insertion, along with relevant counterion-catalyst distances. All bond distances are in Å, energies are reported in kcal/mol, and charges are reported in a.u. All energies are referenced to structure **Int-Ti-Me-B-2,** in **Figure V.2,** (ΔG = -13.2 kcal/mol).

	Initial	TS	Initial Structure					TS				
Conf. 1	**ΔG**	**ΔG**	**Ti Charge**	**B-Ti dist.**	**B-C_1 dist.**	**B-C_2 dist.**	**B-C_3 dist.**	**Ti Charge**	**B-Ti dist.**	**B-C_1 dist.**	**B-C_2 dist.**	**B-C_3 dist.**
Front	-0.5	-	0.60	6.1	5.9	5.4	5.6	-	-	-	-	-
Top	0.1	3.3	0.56	7.0	8.1	9.6	10.4	0.50	6.8	8.0	9.3	9.5
$C_3H_7^+$	6.4	10.2	0.61	7.2	6.8	7.0	7.8	0.53	7.2	6.7	6.6	7.6
C_2H_4	0.5	3.3	0.60	7.2	9.2	9.8	11.3	0.52	6.9	8.6	9.5	10.9
Conf. 2												
Front	-2.0	6.9	0.61	6.2	5.4	6.1	5.9	0.51	6.9	4.9	5.4	5.4
Top	-2.9	5.3	0.51	7.0	7.9	7.8	9.2	0.48	7.2	8.4	8.2	9.6
$C_3H_7^+$	0.5	6.0	0.51	7.4	7.4	5.9	5.7	0.54	7.1	7.2	5.6	5.3
C_2H_4	-1.4	3.5	0.61	6.2	7.5	8.9	9.7	0.51	6.3	6.9	8.0	9.4
Conf. 3												
Front	-0.6	1.6	0.61	6.3	5.7	6.7	7.9	0.52	6.7	4.6	5.2	5.3
Top	1.6	7.2	0.61	7.2	8.6	9.0	9.4	0.49	7.1	9.1	8.7	10.0
$C_3H_7^+$	5.2	9.9	0.62	7.9	6.6	5.1	4.6	0.54	7.3	6.5	5.1	4.8
C_2H_4	-0.6	4.2	0.61	6.2	7.5	9.0	9.4	0.49	5.9	6.2	7.5	8.3
Conf. 4												
Front	-1.5	-	0.64	6.2	5.1	5.9	5.4	-	-	-	-	-
Top	0.9	4.7	0.60	7.4	9.2	9.9	11.3	0.52	7.4	9.2	10.2	11.0
$C_3H_7^+$	-1.5	-	0.55	6.2	4.3	5.1	5.5	-	-	-	-	-
C_2H_4	4.4	5.0	0.63	7.4	9.4	10.4	11.7	0.55	7.6	9.6	10.91	12.1

D.2 Energetics and Bond Distances for Monomer Insertion with Ti-$C_3H_7^+$ and $B(C_6F_5)_4^-$

Table 2: Relative energies of Ti-$C_3H_7^+$ structures aligned with $B(C_6F_5)_4^-$ and their respective TS structure energies for C_2H_4 insertion, along with relevant counterion-catalyst distances. All bond distances are in Å, energies are reported in kcal/mol, and charges are reported in a.u. All energies are referenced to structure **Int-Ti-B-2,** in **Figure V.3** (ΔG = -13.3 kcal/mol).

	Initial	TS	Initial Structure					TS				
Conf. 1	**ΔG**	**ΔG**	**Ti Charge**	**B-Ti dist.**	**B-C_1 dist.**	**B-C_2 dist.**	**B-C_3 dist.**	**Ti Charge**	**B-Ti dist.**	**B-C_1 dist.**	**B-C_2 dist.**	**B-C_3 dist.**
Front	-0.9	-	0.64	6.5	5.9	6.0	5.8	-	-	-	-	-
Top	-6.4	8.5	0.56	7.2	8.6	10.0	11.1	0.54	7.7	6.8	5.6	5.7
$C_3H_7^+$	-1.4	8.2	0.59	7.1	5.5	6.0	5.8	0.52	7.0	5.7	5.7	5.7
C_2H_4	-7.6	-3.4	0.59	6.6	7.9	7.9	9.1	0.49	6.4	7.7	8.2	9.7
Conf. 2												
Front	-7.1	-1.5	0.62	6.3	5.1	6.0	5.7	0.51	6.8	4.8	5.5	5.6
Top	-9.3	1.5	0.57	7.3	8.6	9.1	10.5	0.53	7.3	9.1	8.8	10.1
$C_3H_7^+$	-3.7	16.0	0.59	7.2	7.0	5.5	5.6	0.55	7.1	7.3	5.7	5.5
C_2H_4	-5.3	0.5	0.62	7.1	8.9	10.3	11.4	0.52	6.3	7.6	8.6	10.0
Conf. 3												
Front	-5.9	6.6	0.61	6.2	4.9	5.4	6.6	0.61	6.8	4.8	5.4	6.7
Top	-5.1	-1.3	0.60	7.4	8.6	9.3	10.0	0.48	7.4	8.7	8.8	10.3
$C_3H_7^+$	1.1	-	0.60	7.9	8.7	8.2	7.9	-	-	-	-	-
C_2H_4	-3.9	1.2	0.63	7.3	8.5	10.0	10.8	0.50	6.8	7.3	8.6	9.7
Conf. 4												
Front	-9.4	9.0	0.55	6.9	7.3	5.8	5.6	0.54	6.7	6.6	5.8	6.8
Top	-6.9	-1.8	0.61	7.3	8.4	8.9	10.1	0.53	7.3	8.6	9.0	9.9
$C_3H_7^+$	-3.9	-2.1	0.56	7.0	5.1	5.6	6.0	0.53	7.1	5.8	5.7	6.2
C_2H_4	-3.5	5.6	0.61	6.7	8.3	9.1	10.0	0.53	6.9	6.9	7.9	8.2

BIBLIOGRAPHY

1. A. T. Bell, M. Head-Gordon, Annu. Rev. Chem. Biomol. Eng., **2011,** 2, 453.
2. T. Sperger, Me. A. Sanhueza, I. Kalvet, F. Schoenebeck, Chem. Rev., **2015,** 115, 9532.
3. K. Jackson, S. K. Jaffar, R. S. Paton, Annu. Rev. Prog. Chem. Sect. B: Org. Chem., **2013,** 109, 235.
4. W. Kohn, A. D. Becke, R. G. Parr, J. Phys. Chem., **1996,** 100, 12974.
5. K. E. Riley, M. Pitonak, P. Jurecka, P. Hobza, Chem. Rev., **2010,** 110, 5023.
6 K. Raghavachari, G. W. Trucks, J. A. Pople, M. A. Head-Gordon, Chem. Phys. Lett. **1989**, 157, 479.
7 M. Deegan, P. Knowles, J. Chem. Phys. Lett. **1994,** 227, 321.
8 S. F. Sousa, P. A. Fernandes, M. J. Ramos, J. Phys. Chem. A **2007,** 111, 10439.
9 J.-L. Breonnet, AIMS Material Science **2017**, 4, 1372.
10 C. J. Cramer, D. G. Truhlar, Phys. Chem. Chem. Phys. **2009,** 11, 10757.
11 F. Neese, Coord. Chem. Rev. **2009**, 253, 526.
12 A. TSipis, C. Coord. Chem. Rev. **2014,** 272, 1.
13 P. H.-Y. Cheong, J. M. Um, N. Celebi-Olcum, K. N. Houk, Chem. Rev. **2011,** 111, 5042.
14 Q. N. N. Nguyen, D. Tantillo, Chem – Asian J. **2014,** 9, 674.
15 S. Niu, M. B. Hall, Chem. Rev. **2000,** 100, 353.
16 J. N. Harvey, Annu. Rep. Prog. Chem., Sect. C: Phys. Chem, **2006**, 102, 203.
17 M. Schlangen, H. Schwarz, ChemCatChem, **2010,** 2, 799.
18 X. Feng, J. Gu, Y. Xie, R. B. King, H. F. Schaefer, J. Chem. Theory Comput. **2007,** 3, 1580.
19 J. Tirado-Rives, W. L. Jorgensen, *J. Chem. Theory Comput.* **2008,** 4, 297.
20 O. Isayev, L. Gorb, J. Leszczynski, J. Comput. Chem., **2007,** 28, 1598-1609.
21 M. R. Silva-Junior, M. Schreiber, S. P. A. Saiuer, W. Thiel, *J. Chem. Phys.* **2008,** 129, 104103.
22 A. Dreuw, M. Head-Gordon, *J. Am. Chem. Soc.* **2004,** 126, 4007.
23 T. Stein, L. Kronik, R. Baer, *J. Am. Chem. Soc.* **2009,** 131, 2818.
24 T. Risthaus, S. Grimme, J. Chem. Theory Comput. **2013,** 9, 1580.
25 T. Schwabe, S. Grimme, Acc. Chem. Res. **2008,** 41, 569-579.
26 Klimes, J., Michaelides, A. *J. Chem. Phys.* **2012,** 137, 120901.
27 J.-D. Chai, M. A. Head-Gordon, J. Chem. Phys. **2008,** 128, 084106.
28 M. Bühl, H. Kabrede, J. Chem. Theory Comput. **2006,** 2, 1282−1290.
29 Y. Minenkov, A. Singstad, G. Occhipinti, V. R. Jensen, Dalton Trans. **2012,** 41, 5526−5541.
30 L. M. Pratt, S. Voit, F. N. Okeke, N. Kambe, J. Phys. Chem. A **2011,** 115, 22-81-2290.
31. L. Simon, J. M. Goodman, Org. Biomol. Chem. **2011,** 9, 689-700.
32 T. Marcelli, WiREs Comput. Mol. Sci. **2011**, 1, 142-152.
33 T. Sperger, I. A. Sanhueza, F. Schoenebeck, Acc. Chem. Res., **2016**, 49, 1311.
34 A. J. Cohen, P. Mori-Sanchez, W. Yang, Science, **2008**, 321, 792-794.
35 A. Karton, A. Tarnopolsky, J.-F. Lamere, G. C. Schatz, J. M. L. Martin, J. Phys. Chem. A **2008**, 12868-12886.
36 L. Hu, H. Chen, J. Chem. Theory Comput. **2015**, 11, 4601-4614.
37 M. M. Quintal, A. Karton, M. A. Iron, A. D. Boese, J. M. L. Martin, J. Phys. Chem. A **2006**, 110, 709-716.
38 Y. Zhao, D. G. Truhlar, J. Chem. Theory Comput. **2009**, 5, 324-333.
39 T. Weymuth, E. P. A. Couzijn, P. Chen, M. Reiher, J. Chem. Theory Comput. **2014**, 10, 3092-3103.
40 M. Seth, T. Ziegler, M. Steinmetz, S. Grimme, J. Chem Theory Comput. **2013**, 9, 2286-2299.

41 Y. Lam, M. N. Grayson, M. C. Holland, A. Simon, K. N. Houk, Acc. Chem. Res., **2016,** 49, 750.
42 Q. Peng, F. Durate, R. S. Paton, *Chem Soc Rev* **2016**, 45, 6093-6107.
43 B. H. Schlegel, J Comput Chem **2002,** 24, 1514-1527.
44 B. H. Schlegel, WIREs Comput Mol Sci **2011,** 1, 790-809.
45 M. H. Todd, Chem Soc Rev **2004,** 34, 247-266.
46 A. J. Mulholland, Drug Disc Today **2005,** 10, 1393-1402
47 Y. Zhang, H. Liu, W. Yang, J Chem Phys **2000,** 112, 3483-3492.
48 O, Acevedo, W. L. Jorgensen, Acc Chem Res **2010,** 142, 142-151.
49 S. Marti, V. Moliner, J Chem Theory and Comput **2005,** 1, 1008-1016.
50 S. F. Sousa, A. J. M. Ribeiro, R. P. P. Neves, N. F. Bras, N. M. F. S. A. Cerqueira, P. A. Fernandes, M. J. Ramos, WIREs Comput Mol Sci **2017,** 7:e1281.
51 B. Ensing, M. De Vivo, Z, Lui, P. Moore, M. L. Klein, Acc Chem Res **2006,** 39, 73-81.
52 M. Dontgen, M.-D. Przybylski-Freund, L. C. Kroger, W. A. Kopp, A. E. Ismail, K. Leonhard, J Chem Theory Comput **2015,** 11, 2517-2524.
53 M. Ianuzzi, A. Laio, M. Parrinello, Phys Rev Lett **2003,** 90, 328302-1-328302-4.
54 A. Laio, M. Parrinello, Proc Nat Acad Sci **2002,** 99, 12562-12566.
55 M. P. Haag, K. H. Marti, M. Reiher, Chem Phys Chem **2011**, 12, 3204-3213.
56 K. H. Marti, M. Reiher, J Comput Chem **2009,** 30, 2010-2020.
57 M. A. Kayala, C. A. Azencott, J. H. Chen, P. Baldi, Chem Phys Chem **2011,** 51, 2209-2222.
58 J. H. Chen, P. Baldi, J Chem Inf Model **2009,** 49, 2034-2043.
59 M. A. Kayala, P. Baldi , J Chem Inf Model **2012,** 52, 2526-2540.
60 A. L. Dewyer, A. J. Arguelles, P. M. Zimmerman, WIREs Comput Mol Sci **2018,** 8:e1354
61 E. A. Carter, G. Ciccotti, J. T. Hynes, R. Kapral, Chem Phys Lett, **1989,** 156, 472
62 S. Maeda and K. Morokuma, J. Chem. Theor. Comput., **2011,** 7, 2335.
63 S. Maeda, T. Taketsugu and K. Morokuma, J. Comput. Chem., **2014,** 35, 166.
64 H. P. Hratchain, H. B. Schlegel, In: Dykstra CE, Frenking G, Kim, K. S. Scuseria, G. E., eds. *Theory and Applications of Computational Chemistry: First Fourty Years*. New York,: Elsevier, **2005,** 195-249.
65 P. M. Zimmerman, J. Comput. Chem., **2013**, 34, 1385.
66 P. M. Zimmerman, J. Chem. Theor. Comput., **2013,** 9, 3043.
67 P. M. Zimmerman, Mol. Simul., **2015,** 41, 43.
68 K. Fukui, Acc. Chem. Res. **1981,** 14: 363-368.
69 H. B. Schlegel, Geometry optimization on potential energy surfaces. In: Yarkony DR, ed. Modern Electronic Structure Theory. Singapore: World Scientific Publishing; **1995,** 459-500.
70 H. B. Schlegel, Geometry optimization. In: Schleyer PvR, Allinger NL, Kollman PA, Clark T, Schaefer HF III, Gasteiger J, Schreiner PR. Eds. Encyclopedia of Computational Chemistry. Vol 2. Chichester: John Wiley & Sons; **1998,** 1136-1142.
71 F. Jensen, Transition structure optimization techniques. In: Schleyer PvR, Allinger NL, Kollman PA, Clark T, Schaefer HF III, Gasteiger J, Schreiner PR. Eds. Encyclopedia of Computational Chemistry. Vol 5. Chichester: John Wiley & Sons; **1998,** 3114-3109.
72 D. J. Wales, Energy Landscapes. Cambridge University Press: Cambridge, **2003**.
73 B. A. Grzybowski, K. J. M. Bishop, B. Kowalczyk, C. E. Wilmer Nat Chem **2009,** 1, 31-36.
74 N. Graulich, H. Hopf, P. R. Schreiner, Chem Soc Rev **2010,** 39, 1503-1512.
75 L. J. Broadbelt, S.M. Stark, M. T. Klein, Ind Eng Chem Res **1994,** 33, 790–799.
76 D.M. Matheu, A. M. Dean, J. M. Grenda, W. H. Green, J Phys Chem A **2003,** 107, 8552–8565.
77 C. W. Gao, J. W. Allen, W. H. Allen, R. H. West, Comput Phys Commu **2016,** 203, 212–225.
78 D. Rappoport, C. J. Galvin, D. Y. Zubarev, A. Aspuru- Guzik, J Chem Theory Comput **2014,** 10, 897–907.
79 K, Ohno, S. Maeda, Chem Phys Lett **2004,** 384,277–282.
80 S. Maeda, K. Ohno, J Phys Chem A **2005,** 109, 5742–5753
81 K. Ohno, S. Maeda, J Phys Chem A **2006,** 110, 8933–8941

82 S. Maeda, K. Ohno, K. Morokuma, Phys Chem Chem Phys **2013,** 15, 3683–3701
83 S. Maedia, K. Morokuma, *J. Chem. Phys.* **2010,** 132, 241102.
84 S. Maedia, K. Morokuma, *J. Chem. Theory Comput.* **2011,** 7, 2335-2345.
85 S. Maedia, T. Taketsugu, K. Morokuma, *J. Comput. Chem.* **2014,** 35, 166-173.
86 S. Maedia, Y. Harabuchi, T. Taketsugu, K. Morokuma, *Chem. Rec.* **2016,** 16, 2232-2248.
87 E. Martinez-Nunez, *Phys. Chem. Chem. Phys.* **2015,** 17, 14912-14921
88 E. Martinez-Nunez, *J. Comput. Chem.* **2015,** 36, 222-234
89 J. A. Varela, S. A. Vazquez, E. Martinez-Nunez, *Chem. Sci.* **2017,** 8, 3843-3851
90 P. L. Bhoorasingh, R. H. West, *Phys Chem Chem Phys* **2015,** 17, 32173-32182
91 P. L. Bhoorasingh, B. L. Slakman, F. S. Khanshan, J. Y. Cain, R. H. West, *J Phys Chem* **2017,** 121, 6896-6904.
92 Y. V. Suleimanov, W. H. Green, *J. Chem. Theory Comput.* **2015,** 11, 4248-4259
93 S. Habershon, *J. Chem. Phys.* **2015,** 143, 094106
94 S. Habershon, *J. Chem. Theory. Comput.* **2016,** 12, 1786-1798
95 M. Bergler, G. N. Simm, J. Proppe, M. Reiher, *J. Chem Theory Chem* **2015,** 11,m 5712-5722
96 L. P. Wang, A. Titov, R. McGibbon, F. Liu, V. S. Panda, T. J. Martinez, *Nature Chem* **2014,** 6, 1044-1048.
97 A. L. Dewyer, P. M. Zimmerman, *Org. Biomol. Chem.* **2017,** 15, 501-504.
98 M. Yang, J. Zou, S. Li, *J. Phys Chem. A.* **2017,** 121, 1351-1361
99 Z. Sun, G. A. Winschel, P. M. Zimmerman, P. Nagorny, *Angew Chem Int Edt* **2014,** 53, 11194-11198
100 Y. Y. Khomutnyk, A. J. Argüelles, G. A. Winschel, Z. Sun, P. M. Zimmerman, P. Nagorny, *J. Am. Chem. Soc.* **2016,** 138, 444-456.
101 J.-H. Tay, A. J. Argüelles, M. D. DeMars, P. M. Zimmerman, D. H. Sherman, P. Nagorny, *J. Am. Chem. Soc.* **2017,** 5, 3478-3493
102 S. Bhunya, P. M. Zimmerman, A. Paul, *ACS Catal* **2015,** 5, 3478-3493
103 M. Li, I. M. Pendleton, A. J. Nett, P. M. Zimmerman, *J. Chem. Phys. A.* **2016,** 120, 1135-1144
104 I. M. Pendleton, M. H. Perez-Temprano M. S. Sanford, P. M. Zimmerman, *J. Am. Chem. Soc.* **2016,** 136, 6049-6060.
105 Y. Zhao, A. J. Nett, A. J. McNeil, P. M. Zimmerman, *Macromolecules* **2016,** 49, 7632-7641
106 A. J. Nett, W. Zhao, P. M. Zimmerman, J. Montgomery, *J. Am. Chem. Soc.* **2015,** 137, 7637
107 A. L. Dewyer, P. M. Zimmerman, *ACS Catal***, 2017, 7,** 5466-5477
108 A. K. Leone, A. D. Dewyer, T. Kubo, P. M. Zimmerman, *Unpublished Work: Manuscript in Preparation***, 2019**.
109 P. M. Zimmerman, *J. Comput. Chem.* **2015,** 36, 601-611
110 A. K. Vitek, Doctoral Thesis, University of Michigan, **2019**
111 I. Chen N. Foloppe, *Curr Med Chem,* **2009,** 16, 3381-3413
112 I. Chen. N Foloppe, *Drug Development Research***, 2010,** 72, 85-94
113 J. Bostrom, *J. Comput-Aided Mol Des* **2001,** 15, 1137-1152
114 C. H. Schwab, *Drug Discovery Today Technol.* **2010,** 7, e245-e253
115 J. Ebejer, G. M. Morris, C. M. Deane, *J. Chem. Inf. Model,* **2012,** 52, 1146-1158
116 R. Taylor, *J. Chem. Inf. Model* **2011,** 51, 897-908
117 N. M. O'Boyle, M. Banck, C. A. James, C. Morley, T. Vandermeersch, G. R. Hutchinson, *J. Cheminformatics*, 3, 1-14
118 D. J. Tantillo, *Acc. Chem. Res.* **2016,** 49, 741
119 J. R. Ludwig, R. B. Watson, D. J. Nasrallah, J. B. Gianino, P. M. Zimmerman, R. Wiscons, C. S. Schindler, *Science,* **2018,** 361, 1363-1369
120 M. S. Head-Gordon, J. A. Pople, *J. Chem. Phys.* **1968,** 49, 4643
121 W. J. Hehre, L. Radom, P. V. R. Schleyer, J. A. Pople, *Ab Initio Molecular Orbital Theory,* John Wiley & Sons, New York, **1996**
122 P. M. Zimmerman, *J. Chem. Phys.* **2013,** 138, 184102
123 R. A. Periana, D. J. Taube, E. R. Evitt, D. G. Loffler, P. R. Wentrcek, G. Voss, T. Masuda, *Science,* **1993,** 259, 5093.
124 R. A. Periana D. J. Taube, S. Gamble, H. Taube, T. Satoh, H. Fujii, *Science*, **1998,** 280, 560

125 R. A. Periana, D. J. Taube, E. R. Evitt, D. G. Loffler, P. R. Wentrcek, G. Voss, T. Masuda, *Science,* **1993,** 259, 340
126 R. A. Periana, O. Mironov, D. J. Taube, G. Bhalla, C. J. Jones, *Science,* **2003,** 280, 560
127 A. Paul, C. B. Muscgrave, *Organometallics, **2007,** 26, 793*
128 J. Kua, X. Xu, R. A. Periana, W. A. Goddard III, *Organometallics,* **2002,** 21, 511
129 X. Xu, J. Kua, R. A. Periana, W. A. Goddard III, *Organometallics,* **2003,** 22, 2057
130 K. Mylvaganam, G. B. Bacskay, N. S. Hush, *J. Am. Chem. Soc.* **1999,** 121, 4633
131 K. Mylvaganam, G. B. Bacskay, N. S. Hush, *J. Am. Chem. Soc.* **2000,** 122, 2041
132 P. E. M. Siegbahn, R. H. Crabtree, *J. Am. Chem. Soc.* **1996,** 118, 4442
133 T. M. Gilber, I. Hristov, T. Ziegler, *Organometallics,* **2001,** 20, 1183
134 T. H. Hristov, T. Ziegler, *Organometallics,* **2003,** 22, 1668
135 R. Jazzar, A. R. Hitce, J. Sofack-Kreutzer, O. Baudoin, *Chem. Eur. J.* **2010,** 16, 2654-2672.
136 O. Baudoin, *Chem. Soc. Rev.* **2011,** 40, 4902-4911.
137 J. A. Labinger, J. E. Bercaw, *Nature* **2002,** 417, 507-514.
138 X. Chen, K. M. Engle, D. Want, J.-Q. Yu, *Angew. Chem., Int. Ed.* **2009,** 48, 5094-5115.
139 A. D. Ryabov, *Chem. Rev.* **1990,** 90, 403-424.
140 R. H. Crabtree, *J. Chem. Soc. Dalton Trans.* **2001,** 2437-2450.
141 L. Ackermann, *Top. Organomet. Chem.* **2007,** 24, 35-60.
142 L. Ackermann, R. Vicente, A. R. Kapdi, *Angew. Chem., Int. Ed.* **2009,** 48, 9792-9826.
143 G. Rousseau, B. Breit, *Angew. Chem., Int. Ed.* **2011,** 50, 2450-2494.
144 O. Daugulis, J. Roane, L. D. Tran, *Acc. Chem. Res.* **2015,** 48, 1053-1064.
145 Z. Chen, B. Wang, J. Zhang, W. Yu, Z. Liu, Y. Zhang, *Org. Chem. Front.* **2015,** 2, 1107-1295.
146 K. M. Engle, T. S. Mei, M. Wasa, J.-Q. Yu, *Acc. Chem. Res.* **2012,** 45, 788-802.
147 M. Schnurch, *ARKIVOC,* **2015,** 212-243.
148 T. W. Lyons, M. S. Sanford, *Chem. Rev.* **2010,** 110, 1147-1169.
149 S. R. Neufeldt, M. S. Sanford, *Acc. Chem. Res.* **2012,** 45, 936-946.
150 M. P. Drapeau, L. Gooben, J. *Chem. Eur. J.* **2016,** 22, 18654-18677.
151 H. W. L. Davies, D. Morton, *J. Org. Chem.* **2016,** 81, 343-350.
152 R. Y. Zhu, M. E. Farmer, Y. Q. Chen, J.-Q. Yu, *Angew. Chem. Int. Ed.* **2016,** 55, 10578-10599.
153 Y. Zhao, G. Chen, *Org. Lett. **2011,** 13, 4850-4853*.
154 G. Li, L. Wan, G. Zhang, D. Leow, J. Spangler, J.-Q. Yu, *J. Am. Chem. Soc.* **2015,** 137, 4391-4397.
155 G. Rouquet, N. Chatani, *Angew. Chem., Int. Ed.* **2013,** 52, 11726-11743.
156 D. S.Roman, A. B. Charette, *Org. Lett.* **2013,** 15, 4394-4397.
157 S.-Y. Zhang, G. He, W. A. Nack, Y. Zhao, Q. Li, G. Chen, *J. Am. Chem. Soc.* **2013,** 135, 2124-2127.
158 V. G. Zaitsev, D. Shabashov, O. Daugulis, *J. Am. Chem. Soc.* **2005,** 127, 13154-13155.
159 J. Schranck, A. Tlili, M. Beller, *Angew. Chem., Int. Ed.* **2014,** 53, 9426-9428.
160 C. G. Frost, A. J. Paterson, *ACS Cent. Sci.* **2015,** 1, 418-419.
161 M. Ye, D. L. Gao, J.-Q. Yu, *J. Am. Chem. Soc.* **2011,** 133, 6964-6967.
162 J. He, S. Li, Y. Deng, H. Fu, B. N. Laforteza, J. E. Spangler, A. Homs, J.-Q. Yu, *Science* **2014,** *343, 1216-1220*.
163 T. Patra, S. Bag, R. Kancherla, A. Mondal, A. Dey, S. Pimparkar, S. Agasti, A. Modak, D. Maiti, *Angew. Chem., Int. Ed.* **2016,** 55, 7751-7755.
164 D. Leow, G. Li, T.-S. Mei, J.-Q. Yu, *Nature* **2012,** 486, 518-522.
165 B.-F. Shi, N. Zhang, Y.-H. Maugel, J.-Q. Yu, *Angew. Chem., Int. Ed.* **2008,** 47, 4882-4886.
166 Q. Ding, S. Ye, G. Cheng, P. Wang, M. E. Farmer, J.-Q. Yu, *J. Am. Chem. Soc.* **2017,** 139, 417-425.
167 J. J. Topzcewski, P. J. Cabrera, N. I. Saper, M. S. Sanford, *Nature* **2016**, 531, 220-224.
168 E. A. Mitchell, A. Peschiulli, N. Lefevre, L. Meerpoel, B. U. W. Maes, *Chem. Eur. J.* **2012,** *18, 10092-10142.*
169 A. Millet, D. Dailler, P. Larini, O. Baudoin, *Angew. Chem. Int. Ed.* **2014,** 53, 2678-2682.
170 A. Millet, P. Larini, E. Clot, O. Baudoin, *Chem. Sci.* **2013,** 4, 2241-2247
171 H. Prokopcova, S. D. Bergman, K. Aelvoet, V. Smout, W. Herrebout, B. Van der Veken, L. Meerpoel, B. U. W. Maes, *Chem. Eur. J.* **2010,** 16, 13063-13067.

172 S. J. Pastine, D. V. Gribkov, D. Sames, *J. Am. Chem. Soc.* **2006,** 128, 14220-14221.
173 D. P. Affron, O. A. Davis, J. A. Bull, *Org. Lett.* **2014,** 16, 4956-4959.
174 B. Subdararaju, M. Achard, G. V. M. Sharma, C. Cruneau, *J. Am. Chem. Soc.* **2011,** 133, 10340-10343.
175 B. F. Van Stejvoort, N. Kaval, A. A. Kulago, B. U. W. Maes, *ACS Catal.* **2016,** 6, 4486-4490.
176 A. McNally, B. Haffemayer, Collins, B. S. L. Gaunt, M. J. *Nature* **2014,** 510, 129-133.
177 G. Chen, T. Shigenari, P. Jain, Z. Zhang, Z. Jin, J. He, S. Li, C. Mapelli, M. M. Miller, M. A. Poss, P. M. Scola, K. S. Yeung, J.-Q. Yu,*J. Am. Chem. Soc.* **2015,** 137, 3338-3351.
178 C.-V. T. Vo, J. W. Bode, *J. Org. Chem.* **2014,** 79, 2809-2815.
179 S. Ye, W. Yang, T. Coon, D. Fanning, T. Stamos, D. Neubert, J.-Q. Yu, *Chem. Eur. J.* **2016,** 22, 4748-4752.
180 J. E. Spangler, Y. Verma, P. Kobayashi, D.-H. Wang, J.-Q. Yu, *J. Am. Chem. Soc.* **2015,** 137, 11876-11879.
181 Y. Liu, H. Ge, *Nature Chem.* **2017,** 9, 26-32.
182 W. Cui, S. Chen, J.-Q. Wu, X. Zhao, W. Hu, H. Wang, *Org. Lett.* **2014,** 16, 4288-4291.
183 J.-W. Xu, Z.-Z. Zhang, W.-H. Rao, B.-F. Shi, *J. Am. Chem. Soc.* **2016,** 138, 10750-10753.
184 N. Romero-Revilla, J. A. Rodriguez, M. A. Fernandez-Ibanez, J. C. Carretero, *Chem. Sci.* **2013,** 4, 175-179.
185 X. Zhang, D. W. C. MacMillan, *J. Am. Chem. Soc.* **2016,** 138, 13862-1386.
186 Y. Xu, M. C. Young, C. Wang, D. M. Magness, G. Dong, *Angew. Chem, Int. Ed.* **2016,** 55, 9084-9087.
187 W. M. C. Sameera, F. Maseras, *WIREs Comput. Mol. Sci.* **2012,** 2, 375-385
188 T. Sanhueza, I. A. Sperger, I. Kalvet, F. Schoenebeck, *Chem. Rev.* **2015,** 115, 9532-9586.
189 N. Guimond, S. Gorelsy, K. Fagnou, *J. Am. Chem. Soc.* **2011,** 133, 6449.
190 Y. Boutadla, D. L. Davies, S. A. Macgregor, A. I. Poblador-Bahamonde, *Dalton Trans.* **2009,** 5820-5831.
191 F. Berini, M. Glatz, B. Stoger, M. Peruzzini, L. F. Veiros, K. Kirchner, L. Gonsalvi, *ACS Catal* **2019,** 632-639
192 N. Koga, K. Morokuma, *Chem. Rev.* **1991,** 91, 823-842.
193 K. J. T. Carr, S. A. Macgregor, C. L. McMullin, In *Transition Metal-Catalyzed Heterocycle Synthesis via C-H Activation*, 1st Ed. Wu, X.F., Eds. Wiley-VCH Verlag GmbH & Co. KGaA, **2016;** p. 1.
194 D. Balcells, E. Clot, O. Eisenstein, *Chem. Rev.* **2010,** 110, 749-823.
195 Y. Boutadla, D. L. Davies, S. A. Macgregor, A. I. Poblador-Bahamonde, *Dalton Trans.* **2009,** 5887-5893.
196 J. Guihaume, S. Halbert, O. Eisenstein, R. N. Perutz, *Organometallics* **2012,** 31, 1300-1314.
197 D. G. Johnson, J. M. Lynam, J. M. Slattery, C. E. Welby, *Dalton Trans.* **2010,** 39, 10432-10441.
198 B. Breit, U. Gellrich, T. Li, J. M. Lynam, L. M. Miler, N. E. Pridmore, J. M. Slattery, A. C. Whitwood, *Dalton Trans.* **2014,** 43, 11277-11285.
199 Y. Dang, S. Qu, J. W. Nelson, H. D. Pham, Z.-X. Wang, X. *J.* Wang, *Am. Chem. Soc.* **2015,** 137, 2006-2014.
200 Y.-F. Yang, G.-J. Cheng, P. Lio, D. Leow, T.-Y. Chen, X. Zhang, J.-Q. Yu, Y.-D. Wu, K. N. Houk, *J. Am. Chem. Soc.* **2014,** 136, 344-355.
201 D. G. Musaev, A. Kaledin, B.-F. ,Shi, J.-Q. Yu, *J. Am. Chem. Soc.* **2012,** 134, 1690-1698.
202 A. P. Smalley, M. J. Gaunt, *J. Am. Chem. Soc.* **2015,** 137, 10632-10641.
203 R. Giri, Y. Lan, K. N. Houk, J.-Q. Yu, *J. Am. Chem. Soc.* **2012,** 134, 14118-14126.
204 I. Franzoni, A. I. Poblador-Bahamonde, *Organometallics* **2016,** 35, 2955-2964.
205 M. Wang, Y. Yang, Z. Fan, Z. Cheng, W. Zhu, A. Zhang, *Chem. Commun.* **2015,** 51, 3219-3222**.**
206 Y. Zhang, Z. H. Qi, G. Y. Ruan, W. Liu, Y. Wang, *RSC Adv.* **2015,** 5, 71586-71592.
207 N. Lafrance S. I. Gorelsky, K. *J.* Fagnou, *Am. Chem. Soc.* **2007,** 129, 14570-14571.
208 S. I. Gorelsky, D. Lapointe, K. *J.* Fagnou, *Org. Chem.* **2012,** 77, 658-668.
209 D. L. Davies, S. M. A. Donald, S. A. Macgregor, *J. Am. Chem. Soc.* **2005,** 127, 13754-13755.
210 X. Zhao, C. Sun, Y. Lu, Z. Xing, N. Sun, D. Chen, *Comput. Theor. Chem.* **2015,** 1056, 41-46**.**
211 H. Tang, B. Zhou, X.-R. Huang, C. Wang, J. Yao, H. Chen, *ACS Catal.* **2014,** 4, 649-656
212 H. Tang, X. R. Huang, H. *J.* Chen, *Org. Chem.* **2015,** 80, 4672-4682.
213 Y. Dang, X. Guo, J. Deng, C. Song, W. Hu, Z.-X. Wang, *J. Am. Chem. Soc.* **2016,** 138, 2712-2723.
214 G.-J. Cheng, Y.-F. Yamg, P. Liu, P. Chen, T.-Y. Sun, G. Li, X. Zhang, K. N. Houk, J.-Q. , Yu, Y.-D. Wu, *J. Am. Chem. Soc.* **2014,** 136, 894-897.
215 L. Zhang, D.-C. Fang, *J. Org. Chem.* **2016,** 81, 7400-7410**.**

216 H. Sun, Y. Zhang, P. Chen, Y.-D. Wu, X. Zhang, *Adv. Synth. Catal.* **2016,** 358, 1946-1957.
217 S. M. Khake, R. A. Jagtap, Y. B. Dangat, R. G. Gonnade, K. Vanka, B. Punji, *Organometallics* **2016,** 35, 875-886.
218 T. M. Figg, M. Wasa, J.-Q. Yu, D. G. Musaev, *J. Am. Chem. Soc.* **2013,** 135, 14206-14214.
219 J. Jiang, J.-Q. Yu, K. Morokuma, *ACS Catal.* **2015,** 5, 3648-3661.
220 L. Zhang, D. C. Fang, *J. Org. Chem.* **2013,** 78, 2405-2412.
221 M. D. Lotz, N. M. Camasso, A. J. Canty, M. S. Sanford, *Organometallics* **2017,** 36, 165-171.
222 Y. Wei, H. Tang, X. Cong, B. Rao, C. Wu, X. Zeng, *Org. Lett.* **2014,** 16, 2248-2251.
223 K. J. Zabo, *J. Mol. Catal. A: Chem.* **2010,** 324, 56-63.
224 Y. M. Xing, L. Zhang, D. C. Fang, *Organometallics* **2015,** 34, 770-777.
225 D. Lapointe, K. Fagnou, *Chem. Lett.* **2010,** 39, 1118-1126.
226 D. L. Davies, S. M. A. Donald, S. A. Macgregor, *J. Am. Chem. Soc.* **2005,** 127, 13754-1375.
227 L. Ackermann, *Chem. Rev.* **2011,** 111, 1315-1345.
228 M. Wasa, K. M. Engle, J.-Q. Yu, *J. Am. Chem. Soc.* **2009,** 131, 9886-9887.
229 Y. Dang, X. Deng, J. Song, W. Hu, Z. X. Wang, *J. Am. Chem. Soc.* **2016,** 138, 2712-2723.
230 X. G. Zhang, H. X. Dai, M. Wasa, J.-Q. Yu, *J. Am. Chem. Soc.* **2012,** 134, 11948-11951.
231 W. S. Johnson, V. J. Bauer, J. L. Margrave, M. A. Frisch, L. H. Dreger, W. N. Hubbard, *J. Am. Chem. Soc.* **1961,** 83, 606-614.
232 I. Fabre, N. Von Wolff, G. Le Duc , E. F. Flegeau, C. Bruneau, P. H. Dixneuf, A. Jutand, *Chem. Eur. J.* **2013,** 19, 7595-7604.
233 D. L. Davies, S. M. A. Donald, O. Al-Duaij, S. A. Macgregor, M. Polleth, *J. Am. Chem. Soc.* **2006,** 128, 4210-4211.
234 E. Flegeau, C. Bruneau, P. H. Dixneuf, A. *J.* Jutand, *Am. Chem. Soc.* **2011,** 133, 10161-10170.
235 S. I. Gorelsky, D. Lapointe, K. Fagnou, *J. Am. Chem. Soc.* **2008,** 130, 10848-10849.
236 R. Weber, B. Winter, P. M. Schmidt, W. Widdra, I. V. Hertel, *J. Chem. Phys. B* **2004,** 108, 4729-4736.
237 X. Shen, W. Xu, J. Xu, G. Liang, H. Yang, M. Yao, *Solid State Ionics* **2008,** 179, 2027-2030
238 M. Fyta, I. Kalcher, J. Dzubiella, L. Vrbka, R. R. Netz, *J. Chem. Phys.* **2010,** 132, 024911-1-024911-10.
239 Bryantsev, V. S. Siallo, M. S. Goddard, W. A. *J. Phys. Chem. B* **2008,** 112, 9709-9719.
240 M. I. Childers, A. K. Vitek, L. S. Morris, P. C. B. Widger, S. M. Ahmed, P. M. Zimmerman, G. W. Coates, *J. Am. Chem. Soc.* **2017,** 139, 32, 11048.
241 Y. Zhao, G. Luo, X. Wang, X. Kang, D. Cui, Z. Hou, Y. Luo, *Organometallics,* **2018,** 37, 3210-3218.
242 L. Deng, P. Margl, T. Ziegler, *J. Am. Chem. Soc.* **1999,** 121, 6479-6497.
243 A. K. Vitek, A. K. Leone, A. J. McNeil, P. M. Zimmerman, *ACS Catal***. 2018,** 8 3655-3666
244 S. Ahmadjo, S. Damavandi, G. H. Zohuri, A. Faradipour, Z. Etemadinia, *J. Organometallic Chem.* **2017,** 835, 43-51.
245 K. D. Souther, A. K. Leone, A. K. Vitek, E. F. Palermo, A. M. LaPointe, G. W. Coates, P. M. Zimmerman, A. J. McNeil, *Journal of Polymer Science, Part A: Polymer Chemistry,* **2018,** 56, 132-137.
246 A. K. Leone, K. D. Souther, A. K. Vitek, A. M. LaPointe, G. W. Coates, P. M. Zimmerman, A. J. McNeil, *Macromolecules,* **2017,** 50, 9121-9127.
247 A. G. Roessler, P. M. Zimmerman, *J. Phys. Chem. C* **2018,** 122, 6996-7004.
248 M. L. Smith, A. K. Leone, P. M. Zimmerman, A. J. McNeil, *ACS Macro Lett.* ***2016,*** 5, 1411-1415.
249 D.-H. Kwon, B. L. Small, O. L. Sydora, S. M. Bischof, D. H. Ess, *J. Phys. Chem. C* **2019,** 109, 3737-3739.
250 S.-Y. Yang, T. Ziegler, *Organometallics,* **2006,** 25, 887-900.
251 Y. Zhao, A. J. Nett, A. J. McNeil, P. M. Zimmerman, *Macromolecules,* **2016,** 49, 7632-7641.
252 A. Perfetto, C. Costabile, P. Longo, V. Bertolasi, F. Grisi, *Chem. Eur. J.* **2013,** 19, 10492-10496.
253 I. C. Steward, D. Benitez, D. J. O'Leary, E. Tkatchouk, M. W. Day, W. A. Goddard III, R. H. Grubbs, *J. Am. Chem. Soc.* **2009,** 131, 1931-1938.
254 D. Benitez, E. Tkatchouk, W. A. Goddard III, *Organometallics,* **2009,** 28, 2643-2645.
255 A. Pazio, K. Wozniak, K. Grela, B. Trzaskowski, *Organometallics,* **2015,** 34, 563-570.
256 J. Wysoglad, J.-E. Ehlers, T. Lewe, M. Dornbusch, J. S. Gutmann, *Journal of Molecular Structure***, 2018,** 1166, 456-469.

257 S. Ahmadjo, S. Damavandi, G. H. Zohuri A. Farhadipour, Z. Etemadinia, J. Organometallic Chem **2017**, 835 43-51
258 Y. Zhao, G. Luo X. Wang X. Kang D. Cui, Z. Hou Y. Luo, *Organometallics* **2018,** 37 3210-3218
259 T. P. M. Goumans, A. W. Ehlers, K. Lammertsma, organometallics, **2005,** 24, 3200-3260
260 M. Gatti, L. Vieille-Petit, X. Luan, R. Mariz, E. Drinkel, A. Linden, R. Dorta, J. Am. Chem. Soc. **2009,** 131, 9498-9499
261 A. Perfetto C. Costabile, P. Longo, V. Bertolasi, F. Grisi, Chem Eur J **2013,** 19, 10492
262 D. Benitez, E. Tkatchouk, W. A. Goddard III, Organometallics, **2009,** 28, 2643
263 A. Pazio, K. Wozniak, K. Grela, B. Trzaskowski, Organometallics, **2015**, 34, 563
264 I. C. Stewart, D. Benitez, D. J. O'leary, E Tkatchouk, M. W. Day, W. A. Goddard III, R. H. Grubbs, J. Am. Chem. Soc. **2009,** 131, 1931
265 A. Pazio, K. Wozniak, K. Grela, B. Trzaskowski, Dalton Trans, **2015,** 44, 20021
266 P. Margl, L. Deng, T. Ziegler, *J. Am. Chem. Soc.* **1998,** 120, 5517-5525.
267 T. C. Clancy, W. L. Mattice, *Computational and Theoretical Polymer Science,* **1999,** 9, 261-270.
268 P. Choi, *Frontiers in Chemical Engineering Research*, **2006,** 84, 265-268.
269 T. Yamate, H. Suzuki, K. Kumazawa, T. Fujiwara, T. Yamaguchi, M. Akazome, *Mol. Syst. Des. Eng.,* **2017,** 2, 214-222.
270 U. Agarwal, J. d. Doelder, *Macromolecules,* **2019,** 52, 292
271 Z. Xu, K. Vanka, T. Firman, A. Michalak, E. Zurek, C. Zhu, T. Ziegler, *Organometallics,* **2002,** 21, 2444-2453.
272 G. Lanza, I. L. Fragala, T. J. Marks, *Organometallics,* **2002,** 21, 5594-5612.
273 R. D. J. Froese, D. G. Musaev, T. Matsubara, K. Morokuma, *J. Am. Chem. Soc.* **1997,** 119, 7190-7196
274 L. Deng, T. Ziegler, T. K. Woo, P. M. Margl, L. Fan, *Organometallics,* **1998,** 17, 3240-3253.
275 T. K. Woo, L. Fan, T. Ziegler, *Organometallics,* **1994,** 13, 432-433.
276 L. Y. Fan, D. Harrison, T. K. Woo, T. Ziegler, Organometallics, **1995,** 4, 2018-2026
277 T. K. Woo, L. Fan, T. Ziegler, *Organometallics,* **1994,** 13, 2252-2261
278 T. K. Woo, P. M. Margl, J. C. W. Lohrenz, P. E. Blochl, T. Ziegler, *J. Am. Chem. Soc.* **1996,** 118, 13021-13030.
279 J. J. P. Stewart, *Optimization of Parameters for Semiempirical Methods IV: Extension of MNDO, AM1, and PM3 to more Main Group Elements,* J. Mol. Model. **2004,** 10, 155-164
280 J. J. P. Stewart, J Mol Model **2007,** 13, 1173-1213
281 MOPAC2012, James J. P. Stewart, Stewart Computational Chemistry, Colorado Springs, CO, USA, HTTP://OpenMOPAC.net **(2012).**
282 MOPAC2016, James J. P. Stewart, Stewart Computational Chemistry, Colorado Springs, CO, USA, HTTP://OpenMOPAC.net **(2016)**
283 E. I. Ioannidis, T. Z. H. Gani, H. J. Kulik, *Journal of Computational Chemistry,* **2016,** 37, 2106-2117.
284 J. Okuda, Chem. Ber, **1990,** 109, 1649.
285 J. A. M. Canich, (Exon). U.S. Patent 5,026,798, **1991**.
286 J. C. Stevens, F. J. Timmers, D. R. Wilson, G. F. Schmidt, P. N. Nickias, R. K. Rosen, G. W. Knight, S.-Y. Lai, (Dow). Eur. Pat. Appl. 0 416 815 A2, **1991.**
287 Canich, J. A. M. (Exxon). Eur. Pat. Appl. 0 420 436 A1, **1991**
288 Stevens, J. C. Neithamer, D. R. (Dow). Eur. Pat. Appl. 0 418 044 A2, **1991.**
289 Shao, Y. Gan, Z. Epifanovsky, E. Gilber, A.T. B. Wormit, M. Kussmann, J; Lange, A. W. Behn, A. Deng, J. Feng, X; D. Ghosh, D. Goldey, M. Horn, P. R. Jacobson, L. D. Kaliman, I. Khaliullin, R. Z. Kuś, T. Landau, A. Liu, J. Proynov, E. I. Rhee, Y. M. Richard, R. M. Rohrdanz,M.A.Steele,R.P.Sundstrom,E.J.Woodcock,H.L. Zimmerman, P. M. Zuev, D. Albrecht, B. Alguire, E. Austin, B. Beran, G. J. O. Bernard, Y. A. Berquist, E. Brandhorst, K. Bravaya, K. B. Brown, S. T. Casanova, D. Chang, C.-M. Chen, Y. Chien, S. H. Closser, K. D. Crittenden, D. L. Diedenhofen, M. DiStasio, R. A. Do, H. Dutoi, A. D. Edgar, R. G. Fatehi, S. Fusti-Molnar, L. Ghysels, A. Golubeva-Zadorozhnaya, A. Gomes, J. H.-H. Magnus, W. D. Harbach, P. H. P. Hauser, A. W. Hohenstein, E. G. Holden, Z. C. Jagau, T.-C. Ji, H. Kaduk, B. N. Khistyaev, K. Kim, J. Kim, J. King, R. A. Klunzinger, P. Kosenkov, D. Kowalczyk, T. Krauter, C. M. Lao, K. U. Laurent, A. D. Lawler, K. V. Levchenko, S. V. Lin, C. Y. Liu, F. Livshits, E. Lochan, R. C. Luenser, A. Manohar, P. Manzer, S. F. Mao,

S.-P. Mardirossian, N. Marenich, A. V. Maurer, S. A. Mayhall, N. J. Neuscamman, E. Oana, C. M. Olivares-Amaya, R. O'Neill, D. P. Parkhill, J. A. Perrine, T. M. Peverati, R. Prociuk, A. Rehn, D. R. Rosta, E. Russ, N. J. Sharada, S. M. Sharma, S. Small, D. W. Sodt, A. Stein, T. Stück, D. Su, Y.-C. Thom, A. J. W. Tsuchimochi, T. Vanovschi, V. Vogt, L. Vydrov, O. Wang, T. Watson, M. A. Wenzel, J. White, A. Williams, C. F. Yang, J. Yeganeh, S. Yost, S. R. You, Z.-Q. Zhang, I. Y. Zhang, X. Zhao, Y. Brooks, B. R. Chan, G. K. L. Chipman, D. M. Cramer, C. J. Goddard, W. A. Gordon, M. S. Hehre, W. J. Klamt, A. Schaefer, H. F. Schmidt, M. W. Sherrill, C. D. Truhlar, D. G. Warshel, A. Xu, X. Aspuru-Guzik, A. Baer, R. Bell, A. T. Besley, N. A. Chai, J.-D. A. Dreuw, A. Dunietz, B. D. Furlani, T. R. Gwaltney, S. R. Hsu, C.-P. Jung, Y. Kong, J. Lambrecht, D. S. Liang, W. Ochsenfeld, C. Rassolov, V. A. Slipchenko, L. V. Subotnik, J. E. Van Voorhis, T. Herbert, J. M. Krylov, A. I. Gill, P. M. W. Head- Gordon, M. Mol. Phys. **2015,** 113, 184−215.
290 A. D. Becke, *Chem. Phys.* **1993,** 98, 5648-5652.
291 C. T. Lee, W. T. Yang, R. G. Parr, Phys. Rev. B: Condes. Matter Mater. Phys. **1998,** 37, 785-789.
292 P. J. Stephens, F. J. Devlin, C. F. Chabalowski, M. J. Frisch, *J. Phys. Chem.* **1994,** 98, 11623-11627.
293 R. Krishnan, S. Binkley, R. Seeger, J. A. Pople, *J. Chem. Phys.* **1980**, 72, 650-654 .
294 A. D. Mclean, G. S. Chandler, *J. Chem. Phys.* **1980,** 72, 5639-5648.
295 T. Clark, J. Chandrasekhar, P.v.R. Schleyer *J. Comp. Chem.* **1983,** 4, 294-301.
296 P. M. W. Gill, B. G. johnson, J. A. Pople, M. J. Frisch *Chem. Phys. Lett.* **1992,** 197, 499-505.
297 R. Cammi, J. Tomasi, J. Comput. Chem. **1995,** 16, 1449−1458.
298 J. Tomasi, B. Mennucci, R. Cammi, Chem. Rev. **2005**, 105, 2999−3093.
299 A. V. Marenich, C. J. Cramer, D. G. Truhlar, J. Phys. Chem. B **2009,** 113, 6378−6396.
300 F. Neese, *WIREs Comput Mol Sci* **2012,** 2, 73-78.
301 C. Spickermann, *Entropies of Condesnsed Phases and Complex Systems;* Springer Theses: Berlin, **2011**; p. 1.
302 D. H. Wertz, *J. Am. Chem. Soc.* **1980,** 102, 5316-5322.
303 H. X. Li, X. T. Wang, F. Huang, G. Lu, J. L. Jiang, Z. X. Wang, *Organometallics,* **2011,** 30, 5233-5247.
304 Y. Liang, S. Liu, Y. Z. Xia, Y. H. Li, Z. X. Yu, *Chem. Eur. J.* **2008,** 14, 4361-4373.
305 A. L. McKnight, R. M. Waymouth, Chem Rev, **1998,** 98, 2587-2598.
306 G. J. P. Britovsek, V. C. Gibson, D. F. Wass, Angew. Chem. Int. Ed. **1999,** 38, 428-447.
307 H. Braunschweig, F. M. Breitling, Coord. Chem. Rev. **2006,** 250, 2691-2720.
308 F. G. Sernetz, R. Mulhaupt, R. M. Waymouth, *Macromol. Chem. Phys.* **1996,** 197, 1071-1083
309 C. R. Landis, K. A. Rosaaen, J. Uddin, *J. Am. Chem. Soc.* **2002,** 124, 12062-12063.
310 Y.-X. Chen, C. L. Stern, T. J. Marks, *J. Am. Chem. Soc.* **1997,** 119, 2582.
311 L. Jia, X. Yang, C. L. Stern, T. J. Marks, *Organometallics,* **1997,** 16, 842.
312 Y.-X. Chen, C. L. Stern, T. J. Marks, *J. Am. Chem. Soc.* **1996,** 118, 12451.
313 M. A. Giardello, M. S. Disen, C. L. Stern, T. J. Marks, *J. Am. Chem. Soc.* **1995,** 117, 12114.
314 I. Tritto, R. Donetti, M. C. Sacchi, P. Locatelli, G. Zannoni, *Macromolecules,* **1997,** 30, 1247.
315 I. Tritto, R. Donetti, M. C. Sacchi, P. Locatelli, G. Zannoni, *Macromolecules,* **1999,** 32, 264.
316 G. Lanza, I. L. Fragala, T. J. Marks, *K. J. Am. Chem. Soc.* **2000,** 122, 12764.
317 K. Kunz, G. Erker, G. Kehr, R. Frohlich, H. Jacobsen, H. Berke, O. Blacque, *J. Am. Chem. Soc.* **2002,** 124, 336.
318 K. Vanka, M. S. W. Chan, C. Pye, T. Ziegler, *Organometallics,* **2000,** 19, 1841.
319 M. S. W. Chan, K. Vanka, C. Pye, T. Ziegler, *Organometallics,* **1999,** 18, 4624.
320 G. Lanza, I. L. Fragala, T. J. Marks, *Organometallics,* **2001,** 20, 4006.
321 G. Lanza, I. L. Fragala, T. J. Marks, *J. Am. Chem. Soc.* **1998,** 120, 8257-8258.
322 G. Lanza, I. L. Fragala, *Top Catal.* **1999,** 7, 45
323 R. Fusco, L. Longo, F. Masi, F. Garbassi, *MAcromol. Rapid Commun.***1998,** 19, 257
324 R. Fusco, L. Longo, F. Masi, F. Garbassi, *Macromolecules,* **1997,** 30, 7673.
325 F. Bernardi, A. Bottini, G. P. Miscione, *Organometallics,* **1998,** 17, 16
326 I. E. Nifant'ev, L. Y. Ustynyuk, D. N. Laikov, *Organometallics,* **2001,** 20, 5375-5393.
327 M. S. W. Chan, T. Ziegler, *Organometallics,* **2001,** 19, 5182.
328 G. Lanza, I L. Fragala, T. J. Marks, *Organometallics,* **2002,** 21, 5594.
329 Z. Xu, K. Vanka, T. Ziegler, *Organometallics,* **2002,** 21, 2444.

330 T. K. Woo, L. Fan, T. Ziegler, *Organometallics,* **1994,** 13, 2252
331 F. Schaper, A. Geyer, H. H. Brintzinger, *Organometallics,* **2002,** 21, 473-483.
332A. Klesing, S, Bettonville, *S. Phys. Chem. Chem. Phys.* **1999,** 1, 2373
333 K. Vanka, T. Ziegler, *Organometallics,* **2001,** 20, 905
334 L. Fan, D. Harrison, T. K. Woo, T. Ziegler, *Organometallics,* **1995,** 14, 2018.
335. Z. Xu, K. Vanka, T. Ziegler, *Macromol. Symp.* **2004,** 206, 457-469.
336 Z. Xu, K. Vanka, T. Ziegler, *Organometallics,* **2004,** *23, 104-116*
337 P. J. Cossee, *Catal.* **1964**, 3, 80.
338 E. J. Ariman, P. J. Cossee, *Catal,* **1964,** 3, 99.
339 P. M. Margl, T. K. Woo, P. E. Blochl, T. Ziegler, *J. Am. Chem. Soc.* **1998,** 120, 2174-2175.
340 M. Bergeler, *Doctoral Thesis, ETH-Zurich, Zurich,* **2015**
341 A. C. Vaucher, M. Reiher, *J. Chem. Theory Comput.,* **2018,** 14, 3091.
342 G. N. C. Simms, *Doctoral Thesis, ETH-Zurich, Zurich,* **2018.**
343 M. A. Heuer, A. C. Vaucher, M. P. Haag, M. Reiher, *J. Chem. Theory Comput.* **2018,** 14, 2052.
344 G. N. C. Simm, A. C. Vaucher, M. Reiher, *The Journal of Physical Chemistry A* **2019,** 109, 385-399
345 J. Proppe, M. Reiher. *J. Chem Theory Comput.* **2019,** 15, 357-370.
346 G. N. C. Simm, M. Reiher, *J. Chem. Theory Comput.* **2018,** 14, 5238-5248.
347 M. Reiher, N. Wiebe, K. M. Svore, D. Wecker, M. Troyer. *Proceedings of the National Academy of Sciences* **2017** 114, 7555-7560.
348 A. G. Dana, B. Buesser, S. S. Merchant, W. H. Green, Int. J. Chem. Kinetics, **2018,** 50, 223-258
349 D. Rapporport, A. Aspuru-Guzik, ChemRxiv, **2018**
350 F. Hase, I. F. Galvan, A. Aspuru-Guzik, R. Lindh, M. Vacher, Chem Sci, **2018,** 10, 2298-2307
351 L. M. Roch, F. Hase, C. Kreisbeck, T. Tamayo-Mendoza, L. P. E. Yuner, J. E. Hein, A. Aspuru-Guzik, *Science*, **2018,** 3, eaat5559
352 D. P. Tabor, L. M. Roch, S. K. Saikin, C. Kreisbeck, D. Sheberla, J. H. Montoya, S. Dwaraknath, M. Aykol, C. Ortiz, H. Tribukait, C. Amador-Bedolla, C. J. Brabec, B. Maruyama, K. A. Persson, A. Aspuru-Guzik, Nature Reviews, **2018,** 3, 5-20.
353 M. A. Mantell, J. W. Kampf, M. S. Sanford, *Organometallics,* **2018,** 37, 3240-3242.
354 J. . Varghese, S. H. Mushrif, *React. Chem. Eng*. **2019,** 4, 165.
355 M. C. Lehman, J. B. Gary, P. D. Boyle, M. S. Sanford, E. A. Ison. *ACS Catal.* **2013,** 3, 2304-2310.
356 J. P. Lutz, M. D. Hannigan, A. J. McNeil, *Coord. Chem. Rev.* **2018,** 376, 225-247.
357 P. J. Hay, W. R. Wadt, *J. Chem. Phys.* **1985,** 82, 299-310.
358 L. E. Roy, P. J. Hay, R. L. Martin, *J. Chem Theory Comput.* **2008,** 4, 1029-1031.
359 A. W. Ehlers, M. Bohme, S. Dapprich, A. Gobbi, A. Hollwarth, V. Jonas, K. F. Kohler, R. Stegmann, A. Veldkamp, G. Frenking, *Chem. Phys. Lett.* **1993,** 208, 111-114.
360 A. D. Mclean, G. S. Chandler, *J. Chem. Phys.* **1980,** 72, 5639-5648.
361 S. Grimme, J. Antony, S. Ehlrich, H. Krieg, *K. J. Chem. Phys.* **2010,** 132, 154104.
362 P. J. Hay, W. R. Wadt, *J. Chem. Phys.* **1985,** 82, 270-283.
363 T. H. Dunning, J. Chem. Phys. **1989,** 90, 1007−1023.
364 D. E. Woon, T. H. Dunning, J. Chem. Phys. **1995,** 103, 4572−4585.
365 N. B. Balabanov, K. A Peterson, J. Chem. Phys. 2005, 109, 064107.
366 A. K. Wilson, D. Woon, K. A. Peterson, T. H. Dunning, J. Chem. Phys. 1999, 110, 7667− 7676.
367 D. Glendening, F. Weinhold, *J. Comput. Chem.* **1998,** 19, 610-627.
368 M.S. Gordon, M. W. Schmidt, *Theory and Applications of Computational Chemistry: The First Fourty Years, 1st ed.* Dykstra, C. E., Frenking, F., Kim, K. S., Scuseria, G. E., Eds. Elsevier: Philadelphia, PA, 2005; p 1.
369 Schmidt, M. W. Baldridge, K. K. Boatz, J. A. Elbert, S. T. Gordon, M. S. Jensen, J. H. Koseki, S. Matsunaga, N. Nguyen, K. A. Su, S. Windus, T. L. Dupuis, M. Montgomery, J. A. *J. Comput. Chem.* **1993,** 14, 1347-1363
370 J. P. Perdew, K. Burke, M. Ernzerhof, *Phys. Rev. Lett.* **1996**, *77*, 3865.
371 J. P. Perdew, K. Burke, M. Ernzerhof, *Phys. Rev. Lett.* **1997**, *78*, 1396
372 Y. Zhao, D. G. Truhlar, Theor Chem Acc, **2006,** 1-, 215-241